Pore-scale Modelling of Wettability Alteration in Microporous Carbonates

Wissem Kallel

Submitted for the degree of Doctor of Philosophy

Heriot-Watt University

School of Energy, Geoscience, Infrastructure and Society

November 2016

Abstract

While carbonate reservoirs are recognized to be weakly- to moderately oil-wet at the core-scale, wettability distributions at the pore-scale remain poorly understood. In particular, the wetting state of micropores (pores <5 μm in radius) is crucial for assessing multi-phase flow processes, as microporosity can determine overall pore-space connectivity. Nonetheless, micropores are usually assumed to be water-wet and their role in multi-phase flow has often been neglected. However, oil-wet conditions in micropores are plausible, since oil has been detected within micropores in carbonate rocks. Modelling the wettability of carbonates using pore network models is challenging, because of our inability to attribute appropriate chemical characteristics to the pore surfaces in the presence of the oil phase and over-simplification of the pore shapes.

First, we carry out an investigation of the prevalent wettability alteration scenario due to heavy polar compounds (e.g. asphaltenes) adsorption from the oil phase onto the surface, which occurs strictly *after* oil invasion. We develop a physically-plausible wettability distribution that we incorporate in a quasi-static two-phase flow network model which involves a diversity of pore shapes. The model qualitatively reproduces patterns of wettability alteration recently observed in microporous carbonates via high-resolution imaging. To assess the combined importance of pore-space structure and wettability on petrophysical properties, we consider a homogeneous Berea sandstone network and a heterogeneous microporous carbonate network, whose disconnected coarse-scale pores are connected through a sub-network of fine-scale pores. Results demonstrate that wettability effects are significantly more profound in the carbonate network, as the wettability state of the micropores controls the oil recovery.

Second, we develop a novel mechanistic wettability alteration scenario that evolves *during* primary drainage, involving small polar non-hydrocarbon compounds present in the oil (e.g. alkylphenols, carbazoles, etc.). We implement a diffusion and adsorption model for these compounds that triggers a mild wettability alteration from initially water-wet to more intermediate-wet conditions. This mechanism is incorporated in the quasi-static pore-network model to which we add a notional time-dependency of the invasion percolation mechanism. The model qualitatively reproduces experimental

observations where an early rapid wettability alteration occurred *during* primary drainage. Additionally, we are able to predict clear differences in the primary drainage patterns by varying both the strength of wettability alteration and the balance between the processes of oil invasion and wetting change, which control the initial water saturation for waterflooding. In fact, under certain conditions, the model results in higher oil saturations at predefined capillary pressures compared to the conventional primary drainage. In particular, it leads to the invasion of micropores even at moderate capillary pressures in the microporous carbonate network. Additionally, the model results in significant changes in the residual oil saturations after waterflooding, especially when the wetting state is altered from intermediate-wet to more oil-wet conditions during ageing.

Acknowledgements

To my supervisors, Rink and Ken, for your continuous support.

To my friends, for the memorable times spent together.

To my parents and brother, for your unconditional love and caring.

To my darling, Yasmine, for your unlimited love and for being the rock upon which I stand.

Table of Contents

List of Tables

List of Figures

List of Publications

Journal papers:

Kallel W., Van Dijke, M. I. J., Sorbie, K. S., Wood, R., Jiang, Z., & Harland, S. (2015). Modelling the effect of wettability distributions on oil recovery from microporous carbonate reservoirs. Advances in Water Resources, 1-12. 10.1016/j.advwatres.2015.05.025.

Harland, S. R., Wood, R. A., Curtis, A., Van Dijke, M. I. J., Stratford, K., Jiang, Z., **Kallel W.**, & Sorbie, K. S. (2015). Quantifying flow in variably wet microporous carbonates using object-based geological modelling and both lattice-Boltzmann and pore network fluid flow simulations. AAPG Bulletin, 99(10), 1827–1860. 10.1306/04231514122.

Kallel W., Van Dijke, M. I. J., Sorbie & K. S., Wood, R (2016). Pore-scale Modelling of Wettability Alteration during Primary Drainage (submitted to Water Resources Research).

Conference presentations:

Modelling Wettability in Microporous Carbonates, International Conference on Computational Methods in Water Resources (CMWR), Stuttgart, June 2014.

Pore-scale Modelling of Wettability Alteration during Primary Drainage, International Conference on Porous Media (InterPore), Padua, Italy, May 2015.

Pore-scale Wettability Evolution Model during Primary Drainage, International Conference on Porous Media (InterPore), Cincinnati, OHIO, USA, May 2016.

Nomenclature

COBR	Crude oil/brine/rock system;
CTS	Circle-Triangle-Square cross-sectional shape characterisation of pores;
$\boldsymbol{c}$	The curvature of the cross-sectional shape of a pore;
$\boldsymbol{C_o(\mathrm{t})}$, $\boldsymbol{C_{\mathrm{w}}(\mathrm{t})}$ **and** $\boldsymbol{C_0}$	The mobile concentrations of polar compounds in a given pore at time t in the oil and water phases, respectively ($C_o(\mathrm{t})$ and $C_{\mathrm{w}}(\mathrm{t})$) and the inlet concentration of polar compounds (C_0);
D	Fick's diffusion coefficient;
(FE)SEM	(Field-Emission) Scanning Electron Microscopy;
FWB, SWB	Fast-wetting boundary (FWB) and slow-wetting boundary (SWB), which are limiting cases for the PD/WE model;
$\boldsymbol{f_{ow}}$	The volumetric fraction of oil-wet pores among all the pores in the network ($f_{ow} \in [0,1]$);
$\boldsymbol{h}$	Height in the oil column, linked to a fixed capillary pressure;
IP	Invasion percolation mechanism;
$\boldsymbol{I_{AH}}$, $\boldsymbol{I_{USBM}}$	The Amott-Harvey index (I_{AH}) and the United States Bureau of Mines index (I_{USBM});
K	The Langmuir's adsorption constant;
$\boldsymbol{K_{ro}}$, $\boldsymbol{K_{rw}}$	The oil and water relative permeabilities, respectively;
micro-CT	micro X-ray computed tomography;
MWL, MWS, FW and AW	Inter-pore wettability distributions: the common Mixed-Wet Large (MWL), Mixed-Wet Small (MWS) and Fractionally-Wet (FW); and the developed physically-based Altered-Wet (AW, Chapter 4);
OWC	The oil-water contact i.e. the highest level in the oil column at which the oil saturation is zero;
P	The partitioning coefficient;
$\boldsymbol{P_c}$, $\boldsymbol{P_c^{max}}$, $\boldsymbol{P_c^{min}}$, $\boldsymbol{P_c^*}$	The capillary pressure (P_c), the predefined final (maximum) capillary pressure reached after primary drainage (P_c^{max}), the predefined final (minimum) capillary pressure reached after

	waterflooding (P_c^{min}), and the threshold capillary pressure at which the thin film collapses (P_c^*);
PD	Primary Drainage i.e. first oil charge in a water-filled and water-wet system;
PD/WE	The developed Primary Drainage/Wettability Evolution model, where the wettability alteration evolves during Primary Drainage (Chapter 5);
PL, SO	Piston-like (PL) and snap-off (SO) pore-scale displacements;
PNM	Pore network modelling;
PSD	The distribution of pore-sizes within a network;
PV	Pore volume of the porous medium (core/network);
$\boldsymbol{Q}$	The oil flow rate;
$\boldsymbol{R_{ins}}$	The inscribed radius of the cross-sectional shape of a pore;
$\boldsymbol{S_w}, \boldsymbol{S_o}$	The water and oil saturations, respectively, in a network ($S_o = 1 - S_w$);
$\boldsymbol{S_{wi}}, \boldsymbol{S_{oi}}$	The initial water and oil saturations, respectively, at which waterflood starts following PD ($S_{oi} = 1 - S_{wi}$);
$\boldsymbol{S_{or}}$	The saturation of the residual oil following waterflood;
$\boldsymbol{t_f}$	The final time of the PD/WE simulation;
$\boldsymbol{\beta}$	The limiting contact angle for which $\Gamma = \Gamma_{max}$ ($\beta \in [0,1]$);
$\boldsymbol{\gamma}$	The half-angle of the cross-sectional shape of a pore;
$\boldsymbol{\Gamma(t)}, \boldsymbol{\Gamma_{max}}$	The adsorption level of polar compounds per unit area in a given pore at time t ($\Gamma(t)$) and the Langmuir's maximum adsorption level (Γ_{max});
Δ_t^{TR}	The transport model's time-step;
$\boldsymbol{\theta}, \boldsymbol{\theta_{pd}}, \boldsymbol{\theta_{max}}, \boldsymbol{\theta_{a,ww}}$ and $\boldsymbol{\theta_{a,ow}}$	The oil-water contact angle (θ), the primary drainage (fixed) contact angle (θ_{pd}, Chapter 4), the maximum contact angle reached following PD/WE (θ_{max}, Chapter 5) and the water-wet and oil-wet advancing contact angles, respectively ($\theta_{a,ww}$ and $\theta_{a,ow}$);
Π, Π_{crit}	Disjoining pressure (Π) and critical disjoining pressure at which thin films collapse (Π_{crit});

$\boldsymbol{\sigma_{ow}}$	Oil-water interfacial tension;
$\boldsymbol{\chi_{ph}, \widehat{\chi_{ph}}}$	Euler number (χ_{ph}) and normalised Euler number ($\widehat{\chi_{ph}}$) of a given phase ph (oil/water) in a saturated network.

Chapter 1 : Introduction

Understanding the wettability state of a porous medium is essential for accurate modelling of multi-phase flow processes in hydrocarbon reservoirs, as well as in aquifers following contamination by non-aqueous phase liquids or injection of carbon-dioxide. Specifically, in simulations of hydrocarbon reservoir behaviour, assumptions on the wettability distribution strongly influence many petrophysical functions. This includes the capillary pressure and relative permeability data, as well as the oil recovery efficiency after waterflooding. The stakes become notably high when dealing with carbonate rocks, as such formations host a significant amount of the remaining oil reserves (Roehl and Choquette, 2012).

The pore-scale wettability of microporous carbonates has been unresolved. Indeed, the micropores, which may be defined as pores <5 µm in radius (Cantrell and Hagerty, 1999), have usually been excluded from contributing to the flow process as they were often supposed to be water-filled and water-wet. Nonetheless, the rise of imaging technology in recent years helped visualise the pore-scale fluids distribution and wettability at the micro and nanometre scale. In fact, many authors have detected oil in micropores using high-resolution imaging (Al-Yousef et al., 1995, Clerke, 2009, Knackstedt et al., 2011, Fung et al., 2011, Clerke et al., 2014, Dodd et al., 2014). This was an important step forward to acknowledge the role that micropores might play in oil recovery processes, as well as to recognise a possible oil-wet state in micropores. This was confirmed by Marathe et al. (2012) who detected oil-wet micrite facets, and identified a face-selective pattern of wettability alteration where curved surfaces are oil-wet, in contrast with smooth water-wet surfaces. Nonetheless, questions arise about how oil migrates into such tiny micropores without reaching huge capillary pressures. This might be linked to a scenario of wettability alteration that has occurred over geological time.

In this work, we aim to model the pore-scale wettability alteration in complex multiscale carbonate rocks. To achieve this, we use a quasi-static two-phase flow pore network model that involves a wide range of pore shapes and includes a realistic thermodynamic criterion for the formation and collapse of oil layers. Our main objectives consist of:

a) Reproducing the wettability alteration trends shown by high-resolution imaging of microporous carbonates (Marathe et al., 2012).
b) Assessing the importance of the micropores' wettability on oil recovery.
c) Understanding the oil migration process into tiny micropores with excessively high entry pressures.

In Chapter 2, we carry out in a first section an extensive review of the concept of wettability in the literature. We first examine the different pore-scale mechanisms responsible for the wettability alteration. Then, we describe the main factors that are thought to affect wettability. Subsequently, we study how wettability is assessed from pore to pore and how its pore-space distribution is characterized. Then, we examine the significant effect of wettability on residual oil saturations. In the second section of this chapter, we focus on the particular case of microporous carbonates, for which we begin presenting their main structural features. It is followed by an analysis of the carbonates' wettability characteristics and their oil recovery efficiency. Finally, we provide an overview of the pore-scale modelling of multiscale carbonate rocks.

In Chapter 3, we briefly introduce the pore network modelling approach in general. Then we present the quasi-static two-phase flow network modelling tool we use in this work and describe its main features. Indeed, we present the variety of pore shapes modelled, and the corresponding wide range of fluid configurations and multiple fluids displacements. We then describe the commonly used workflow of primary drainage, ageing and waterflooding, detailing the different pore-level displacement mechanisms involved. We also introduce the Euler number as a measure of the connectivity of the network and the fluid phases. Finally, we present the two topologically different pore network models that are inputs to our simulations: a homogeneous Berea sandstone network and a complex multiscale carbonate network.

In Chapter 4, we aim at meeting objectives a) and b). For this, based on the model developed by Kovscek et al. (1993), we suggest a physically plausible wettability distribution model *following* primary drainage, subsequent to ageing, that takes into account both the pore size and shape. The resulting wettability distribution, referred to as Altered-Wet, is compared to the standard wettability distributions that are either exclusively correlated to pore size (Mixed-Wet Large and Mixed-Wet Small) or distributed regardless of size (Fractionally-Wet). Then, we investigate the effect of the

wettability distribution on the petrophysical properties, especially on the residual oil saturation, for both the Berea and carbonate networks.

In Chapter 5, we aim at meeting the final objective c). To achieve this, we suggest a novel model of wettability alteration that occurs *during* primary drainage, based on the work by Bennett et al. (2004). We thoroughly describe the model, consisting of a time-dependent oil invasion coupled with a transport model for polar compounds, whose adsorption triggers a wettability change. Then, for each of our input networks, we show the results of primary drainage at the pore level, which we link to the reservoir scale. Finally, we present the subsequent waterflood calculations and the resulting residual oil saturation patterns, depending on whether an additional wettability alteration from water-wet/intermediate-wet to oil-wet conditions during ageing was performed.

Finally, Chapter 6 consists of a summary of our main results and key findings. We further recommend possible suggestions as future work.

Chapter 2 : Literature review

2.1 Wettability alteration

The wettability of a solid surface describes its degree of molecular affinity towards one fluid (water/oil) rather than the other (Abdallah et al., 2007). Wettability is a surface phenomenon, typically quantified using the equilibrium contact angle, θ, measured between the fluids at the interface, usually through the denser (water) phase, as shown in Figure 2.1. Physically, the contact angle is a surface property describing the balance between the surface and interfacial forces, unique for a given combination of a solid and two pure fluids. It is computed through Young's equation:

$$\sigma_{so} = \sigma_{sw} + \sigma_{ow} cos\theta \qquad (2.1)$$

where σ_{so}, σ_{sw} and σ_{ow} are the surface-oil, surface-water and oil-water interfacial tensions, respectively. However, for a real crude oil/brine/rock (COBR) system, the wettability cannot be characterised by a single contact angle but rather by numerous contact angles at the different three-phase contact points zones (Hirasaki, 1991). For instance, two different contact angles can be depicted, the advancing and receding contact angles, depending on whether the water is the displacing or the displaced phase, respectively. This phenomenon, the so-called contact angle hysteresis, is mainly a result of surface chemical heterogeneity and roughness. The advancing contact angle is usually higher than the receding contact angle, and the gap between the two values grows with increased roughness (Morrow, 1975).

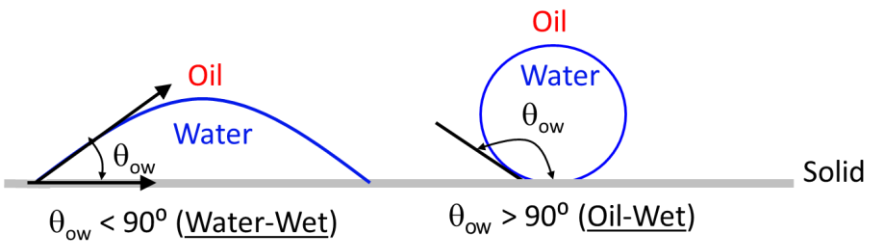

Figure 2.1: Wettability illustrated using a pure water drop at equilibrium on a smooth solid surface, surrounded by pure oil. If $\theta < 90°$, the surface is water-wet and the oil drop spreads on the surface. Otherwise, if $\theta > 90°$, the surface is oil-wet and the oil drop forms a bead, minimizing the contact with the solid.

2.1.1 Pore-scale wettability alteration mechanisms

Reservoir rocks are thought to have been initially filled by formation water for a long geological time thus having an initial strong water-wet state before oil migration (Marzouk, 1999, Hamon, 2000, Abdallah et al., 2007). The pore-scale wettability alteration of reservoir rocks has often been associated with asphaltenes, which have been cited as being major wetting alteration agents. These are high molecular weight polar aggregates occurring in many crude oils, coated by lower molecular weight molecules called resins. Asphaltenes are characterised by a high surface activity. However, their large average size of $\sim 0.6\ \mu m$ is thought to prevent them from accessing pores smaller than their own size (Al-Yousef et al., 1995). In addition, asphaltenes have the characteristic of being highly insoluble in water, i.e. hydrophobic. This prevents them from penetrating thin protective water films that occur on water-wet surfaces (Hirasaki, 1991) and directly contacting the pore walls.

Using "adhesion tests" on smooth silicate surfaces, Buckley and Liu (1998) identified four mechanisms that are jointly responsible for the adsorption of such polar components from the crude oil onto the surface: polar interactions, surface precipitation, acid/base interactions and ion-binding:

- Polar interactions occur between polar compounds in the oil and polar sites on the surface. They only contribute when the oil is directly in contact with the surface i.e. in the absence of a protective water film, thus are unlikely to take part in initially aqueous systems. This mechanism leads to moderate wettability alteration to intermediate-wet conditions.
- The surface precipitation of asphaltenes may take place in the case where the crude oil's solvency for its asphaltenes is low. This leads to a relatively high wettability alteration to oil-wet conditions.
- In the presence of a water film, Coulombic acid/base interactions occur between ionized acidic and basic components at electrically charged oil/water and solid/water interfaces. These interactions control the surface charge at the interfaces, which in turn affects both the water-film stability and surface adsorption. The resulting contact angles depend on both the water composition (pH and ionic properties) and oil properties (acid and base numbers).

- Ion binding interactions may prevail over the acid/base interactions in the presence of divalent and/or multivalent ions in the brine (e.g. Ca^{2+}). These ions bind at the oil/water and solid/water interfaces and influence the contact angle. As for the acid/base interactions, the extent of the wettability alteration depends mainly on the oil and brine compositions.

Kovscek et al. (1993) established a pore-level scenario to describe the wettability alteration of initially water-wet rocks following ageing in crude oil. It is based on the existence of the thin films that coat the pore wall and preserve the rock's initial wettability state. At equilibrium, the water film in a given pore is stabilised by thin film forces; the related pressure is the so called disjoining pressure, Π. Three major factors contribute to the disjoining pressure: Electrostatic interactions, Van der Waals interactions and Hydration forces (Hirasaki, 1991). As shown in the illustrative disjoining pressure isotherm (Figure 2.2), Π depends on the thickness of the water film. As the capillary pressure $P_c = P_o - P_w$ i.e. the difference in pressure at the oil/water interface, rises during oil invasion, the film gets thinner. The film first gains in stability since Π rises, until P_c reaches a threshold capillary pressure, P_c^*:

$$P_c^* = \Pi_{crit} + \sigma_{ow} c \qquad (2.2)$$

The threshold capillary pressure is an intrinsic property of the pore related to the oil-water interfacial tension, σ_{ow}, the curvature of the pore wall, c, and the critical disjoining pressure at which the film collapses, Π_{crit}. The latter depends on the fluid system and mineralogy of the rock surface. In fact, when $P_c > P_c^*$, $i.e. \Pi < \Pi_{crit}$, the film becomes unstable and breaks down to a molecularly thin one. Subsequently, polar compounds from the oil, mainly asphaltenes, may then irreversibly adsorb onto the surface, hence rendering it oil-wet.

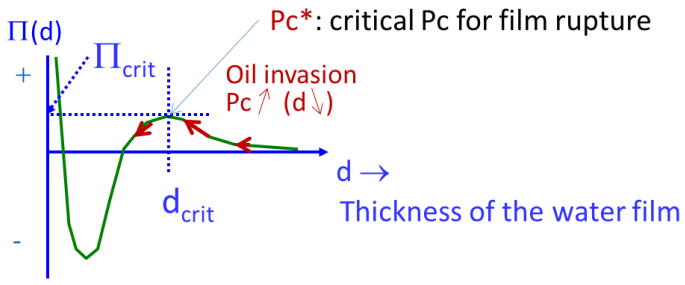

Figure 2.2: Evolution of thin film stability during oil invasion, illustrated on an example of disjoining pressure isotherm $\Pi(d)$, after Hirasaki (1991).

Kovscek et al. (1993) incorporated their wettability alteration mechanism in a capillary bundle model with star-shaped pore cross sections. The resulting capillary pressure curves and residual oil showed reasonable qualitative agreement with experimental results. Frette et al. (2009) also included this scenario in a bundle-of-tubes theoretical model with 2D realistic pore cross sections derived from high resolution SEM (Scanning Electron Microscopy) images, for which they examined the relationship between collapsed films fraction and capillary pressure. It has also been implemented in 3D network models (Blunt, 1997, Blunt, 1998, Oren et al., 1998, Jackson et al., 2003). To allow wettability changes to occur, these models employed angular pore cross sections, and a simple parametric model for the water film collapse.

A complementary theory suggests that the thin water films may initially be destabilised by the adsorption of polar components with smaller molecular weight that are present in the crude oil (van Duin and Larter, 2001, Bennett et al., 2004, Bennett et al., 2007). Indeed, crude oils are usually rich in smaller polar non-hydrocarbon compounds, for instance the aromatic oxygen compounds such as alkylphenols (e.g. phenol $C_0 - C_3$) (Taylor et al., 1997, Lucach et al., 2002). Alkylphenols are characterized by their high solubility in water (hydrophilic, unlike asphaltenes) and high surface activity. Indeed, Huang et al. (1996) induced wetting changes in a laminated rock using a "synthetic crude oil" containing a number of candidate smaller polar molecules such as cresols, phenols, carbazoles, etc. van Duin and Larter (2001) used molecular dynamics simulations to suggest a wettability alteration process involving these small water-soluble polar non-hydrocarbon compounds. First, they penetrate the water films that initially coat water-wet mineral surfaces. They then rapidly adsorb onto the surface and render it more hydrophobic. As a result, the water film is disrupted and the disjoining pressure is reduced thus making the film prone to collapse at the existing local oil/water capillary pressure. This water film collapse then allows direct contact with the surface by heavier compounds, such as asphaltenes. As a result, the surface is rendered oil-wet with contact angles reaching up to $180°$.

Bennett et al. (2004) confirmed this wettability alteration process using a core-flood experiment on a sandstone, where they observed an early rapid wettability alteration that occurred during primary drainage involving alkylphenols. Indeed, these small polar species were absent from the eluted oils at the end of the experiment ("p-cresol" in

Figure 2.3(a)). The non-appearance of polar compounds is mainly due to their high interaction with the surface, which decreased across the length of the core (Figure 2.3(b)). This resulted in a significant wettability alteration, preferentially near the inlet, as confirmed by an ESEM (Environmental SEM) examination of the core after wetting alteration. In fact, while water spread as continuous sheets near the outlet, supporting a water-wet behaviour (Figure 2.3(c)), it appeared as discrete droplets on surfaces near the inlet, supporting rather oil-wet conditions (Figure 2.3(d)). Additionally, the authors pointed out the relative speed of the process, which may happen in a reservoir over a time-scale from days to months. Thus, the timescale of wetting alteration in such a mechanism would depend on the slowest step in the process from diffusion of the polar organics into the water films, the adsorption of these smaller polar molecules to the rock surface, the lowering of the disjoining pressure of the water film and its subsequent collapse and finally the adhesion of larger polar compounds such as asphaltenes onto the rock surface, which is unknown.

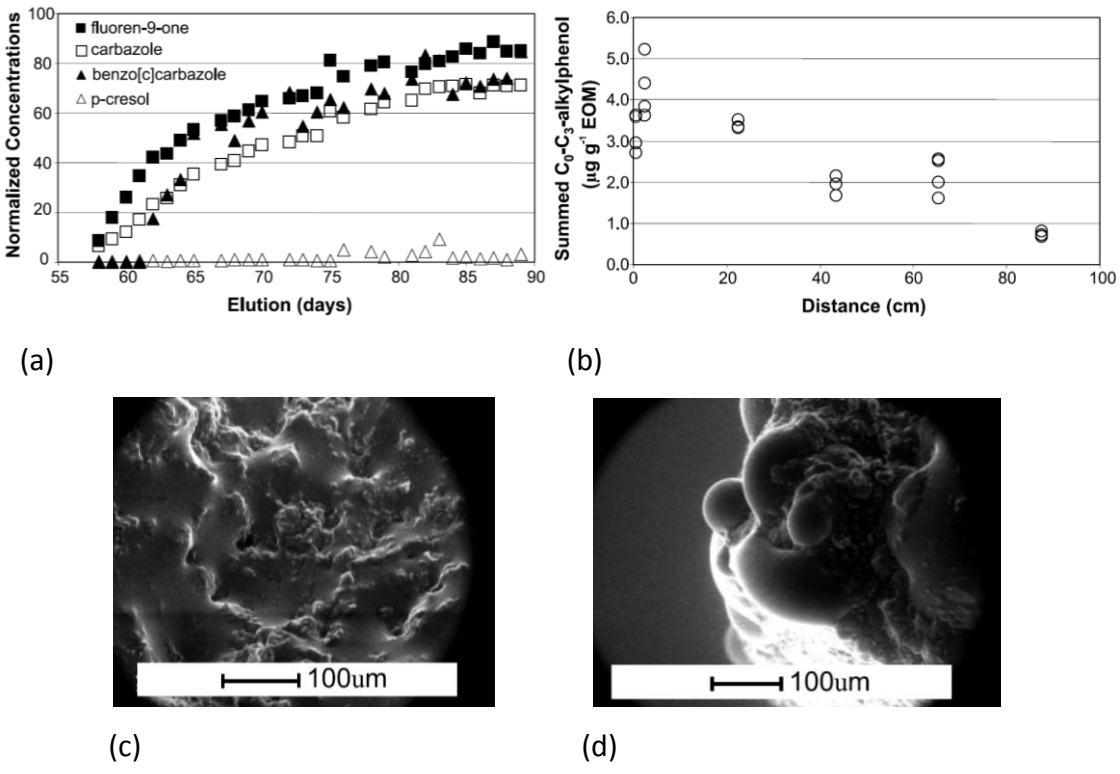

Figure 2.3: (a) Plot of the normalized concentrations of polar compounds in the produced oil (mobile) function of the elution time; (b) Plot of the concentration of "p-cresol" in the core extract oil (immobile) relative to the distance along the core; ESEM images showing water spreading trends from (c) the outlet and (d) inlet of the core (Bennett et al., 2004).

The scenario suggested by Bennett et al. (2004) is compatible with the findings by Graue et al. (2002) who performed core-flood experiments on chalk (carbonate) rocks. They observed that the wettability alteration process was more efficient by continuous injection of crude oil during ageing, as opposed to stopping the oil invasion. Additionally, the authors pointed out the important increase in wettability alteration efficiency with the core length, as the continuously flushed oil was resupplying its surface-active polar compounds, thus speeding up the ageing process.

2.1.2 Factors affecting wettability

A multitude of factors are thought to affect wettability, which is a property of the whole COBR system. These widely include the rock's intrinsic properties, the brine and crude oil properties as well as the ageing history. Nonetheless, the importance of each of the factors cited above is not agreed upon in the literature as it depends on the specific system studied.

The rock's intrinsic properties

Some intrinsic properties of the rock, such as the geometry of the pores (size, roughness, etc.) and surface mineralogy, are thought to affect wettability. Indeed, Fassi-Fihri et al. (1995) observed that wettability in carbonates was mostly affected by pore geometry, while mineralogy was found to be the major factor controlling wettability in sandstones. On the other hand, Hamon (2000) examined a large dataset of samples from a sandstone hydrocarbon reservoir and found no evidence that pore mineralogy has any direct impact on wettability. He rather observed that horizontal wettability variations across the reservoir (at constant capillary pressures) are dependent on the pore geometry through the sample's permeability, with more oil-wet conditions for higher permeabilities.

The brine characteristics

The brine characteristics, mainly identified as its ionic composition and pH, may play a role in wettability alteration. Indeed, Mahani et al. (2015) demonstrated that for sandstones, wettability in the presence of clay is mostly dependent on the brine's ionic composition.

The crude oil composition

Buckley and Liu (1998) focused on the effect of the crude oil composition on the wettability by comparing crude oils with strikingly different compositions. They identified three chemical characteristics that determine the potential of a crude oil to alter the surface wettability: its acid number, its base number and its API gravity (or density), which measures its solvency for its polar components (e.g. asphaltenes). Interestingly, they showed that the solvent environment to which the asphaltenes belong is more important to their potential wetting performance than their actual amount. In fact, the poorer the solvent quality of a crude oil to its asphaltenes, the stronger would be the resulting oil-wet conditions.

Besides, Idowu et al. (2015) examined using high-resolution imaging techniques two (cleaned) mini-plugs of an outcrop and a reservoir sandstone following ageing in crude oil. They showed that the samples ended up in uniformly water-wet and oil-wet conditions, respectively, even though they were characterized by quasi-identical mineralogies (dominated by quartz and plagioclase). They suggested that the observed deviations in wetting behaviour were mainly due to the difference in the crude oils they utilized for each sample.

The saturation and ageing history

The wettability of reservoir rocks depends strongly on their original structural position (Marzouk, 1999, Hamon, 2000, Abdallah et al., 2007, Okasha et al., 2007)**.** In fact, wettability generally varies vertically in the reservoir with height above the oil-water contact (OWC) i.e. the highest level in the oil column at which the oil saturation is zero. Indeed, the higher the sample in the oil column, the more oil-wet it is likely to be. This results in the establishment of a mixed wettability state in the transition zone (as illustrated in Figure 2.4). This wetting behaviour can be attributed to three major factors:

- The capillary pressure being higher at the top, which results in thin films coating the pore walls becoming less stable (Hamon, 2000) (see Section 2.1.1).
- Oil accumulated from top to bottom, hence oil contacted the upper surfaces for a longer time (Marzouk, 1999).
- A higher number of pores are invaded at the top, thus the overall sample's affinity to oil is more likely to increase (Jackson et al., 2003).

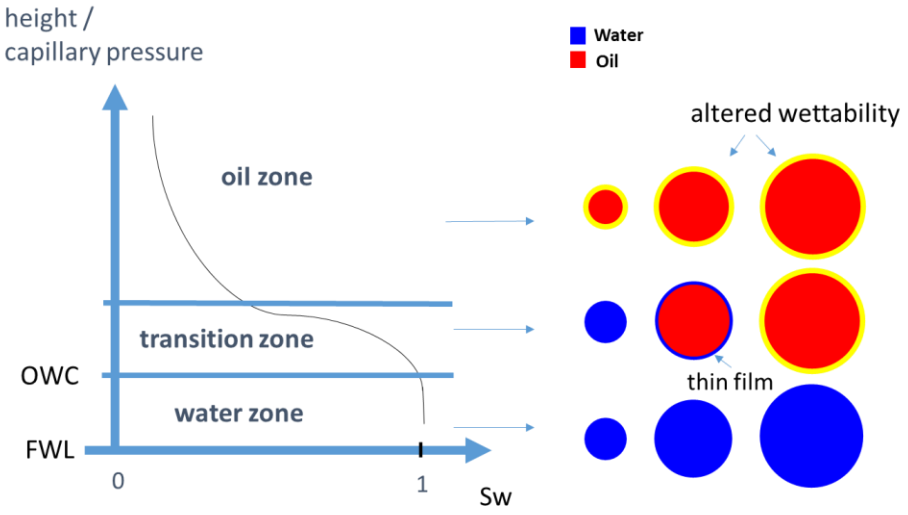

Figure 2.4: Structural position effect on fluid saturations and wettability within a typical reservoir. In the water and oil zones, all pores are water-filled & water-wet and oil-filled & oil-wet, respectively. In the transition zone, the smallest and largest pores are water-filled & water-wet and oil-filled & oil-wet, respectively. However, some intermediate-sized pores may be oil-filled & water-wet, as the thin water film may resist the moderate capillary pressure exerted.

The ageing time and temperature are also thought to affect wettability. As for the ageing time, if any correlation exists, it tends to be positive with respect to the oil-wetness (Buckley and Liu, 1998, Kowalewski et al., 2003)**.** Rock samples are typically brought from an initial water-wet to an oil-wet state by aging in crude oil in labs for a duration ranging from several days to a few weeks. Kowalewski et al. (2003) observed that ageing sandstone samples in crude oil at 75 °C beyond 10 days did not induce any further changes to their wettability. However, the relationship between the ageing temperature and extent of wettability change is still debated in the literature. While Buckley and Liu (1998) observed an increase in the measured contact angles with temperature on a glass surface; the opposite effect was reported by Lichaa et al. (1993) on calcite surfaces from three different carbonate samples.

2.1.3 Assessing wettability

No universal method is currently available to accurately evaluate the wettability of a real COBR system, which cannot be described by a unique contact angle. Instead, both quantitative and qualitative methods were designed to provide a description of wettability as close as possible to the real one.

a) Quantitative methods

On the one hand, direct quantification of wettability can be done through contact angle measurements, traditionally from pure mineral surfaces, or more recently using high-resolution imaging techniques. On the other hand, indirect methods use capillary pressure curves to infer an average wettability state of the core.

Contact angle measurements

Contact angles can be directly evaluated from mineral surfaces. For this, several methods have been developed, thoroughly reviewed by Yuan and Lee (2013). These include the commonly used sessile drop, the captive bubble and the Wilhelmy balance methods. The main shortcoming of these techniques is that they require a rigid, smooth, homogeneous surface interacting with a pure fluid. Hence, they fail to capture the full heterogeneity of a real system.

Important progress in imaging led to the development of advanced techniques such as the Drop Shape Analysis (DSA) method and its improvement the Axisymmetric Drop Shape Analysis (ADSA) method (Yuan and Lee, 2013). These techniques evaluate the contact angle by analysing the shape of a drop and fitting it into a theoretical profile. They are undergoing continuous improvement, leading to ever more accurate wettability measurements and a much enhanced reproducibility.

Andrew et al. (2014) suggested a new method to directly measure the contact angles from micro-CT (micro X-ray computed Tomography) images. It is based on manual tracings of vectors tangential to the non-wetting/wetting interface and the solid surface, as shown in Figure 2.5. They applied this technique on a CO_2-brine-carbonate system and obtained a distribution of contact angles centred around $45°$ i.e. the system was weakly water-wet. However, the method requires hundreds of manual tracings. Moreover, at the microscale, thin water films (nanometre-scale) are not resolvable, hence the three-phase contact line -if existent- may not be accurately identified.

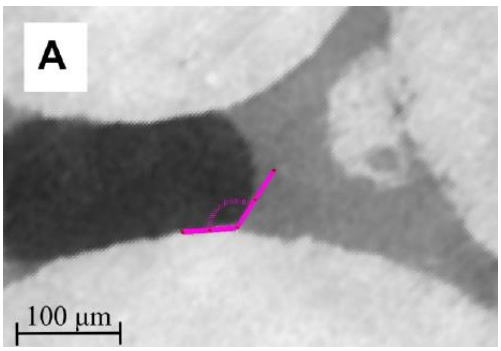

Figure 2.5: An example of a measured contact angle $(53°)$*; it is the complement of the traced angle (pink arc,* $127°$*) measured through the* CO_2 *(black, less dense phase) (Andrew et al., 2014).*

Amott / USBM

To evaluate the average wettability of reservoir core samples, indirect methods requiring capillary pressure data are used, based on displacement analysis, namely the Amott-Harvey index (I_{AH}) (Amott, 1959) and United States Bureau of Mines index (I_{USBM}) (Donaldson et al., 1969). Figure 2.6 gives a brief overview on how these are calculated. Practically, both indices range between -1 for strongly oil-wet to 1 for strongly water-wet conditions. They can be calculated from a single combined experiment (Sharma and Wunderlich, 1987). Note that neither of the tests is based on a well-established theory, they are rather empirical. Moreover, even though they have been of interchangeable usage in the literature, the link between them from a theoretical and practical point of view remains ambiguous. Indeed, while the Amott index is controlled by spontaneous displacement, the USBM index mainly depends on the energy associated with forced displacement. Dixit et al. (2000) used both analytical computations and the pore network modelling approach to examine the relationship between the two indices. They demonstrated that indeed a broad correlation exists between them, further explained in Section 2.1.4, which can provide further interpretation of some experimental results. Moreover, they showed that both indices depend on the network characteristics (e.g. pore size distribution, network connectivity). This was consistent with experimental results conducted later by Hamon (2000) who clearly states that these measures are not a pure reflection of the intrinsic wettability of the rock.

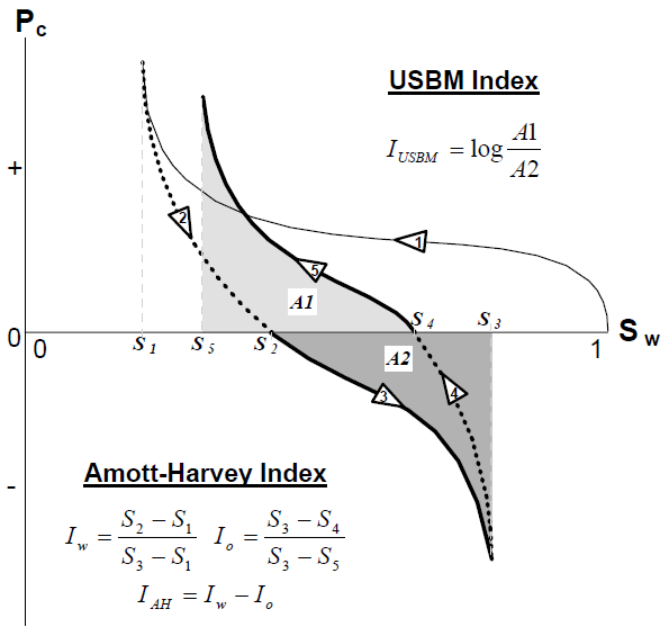

Figure 2.6: Calculation of the Amott indices to water, I_w, and oil, I_o, and their combination through the Amott-Harvey index I_{AH}, as well as the USBM index, I_{USBM}. These depend on the water saturations, S_j, at the end of the flood j ($j = 1$ – primary drainage, 2 - spontaneous imbibition, 3 – forced imbibition, 4 – spontaneous drainage, 5 - forced drainage) (Dixit et al., 2000).

b) Qualitative methods

Qualitatively, imaging techniques are able to reveal wettability distributions in rocks at the level of individual pores. For instance, Cryo-SEM (cryogenic SEM) was used to infer the local wettability from the visualised fluid distributions at the microscale (Fassi-Fihri et al., 1995, Al-Yousef et al., 1995, Kowalewski et al., 2003). In fact, Fassi-Fihri et al. (1995) confirmed the heterogeneity of wettability at the pore scale. They were also able to observe wetting films, but only those thicker than the imaging resolution of $0.1\mu m$.

The Atomic Force Microscopy (AFM) technique (Lord and Buckley, 2002, Morrow and Buckley, 2006) can be used to visualise nano to micron-scale topographic variations of mineral surfaces following contact with crude oil. Lord and Buckley (2002) used AFM to describe the properties of the adsorbed film on smooth mica surfaces exposed to crude oil. They were able to resolve the micron-scale asphaltene aggregates deposited on the surface, cemented to it through an adsorbed film. The latter consists of other polar compounds from the crude oil, and is of about 15 nm thickness. Morrow and Buckley (2006) observed similar trends when ageing calcite surfaces (Figure 2.7).

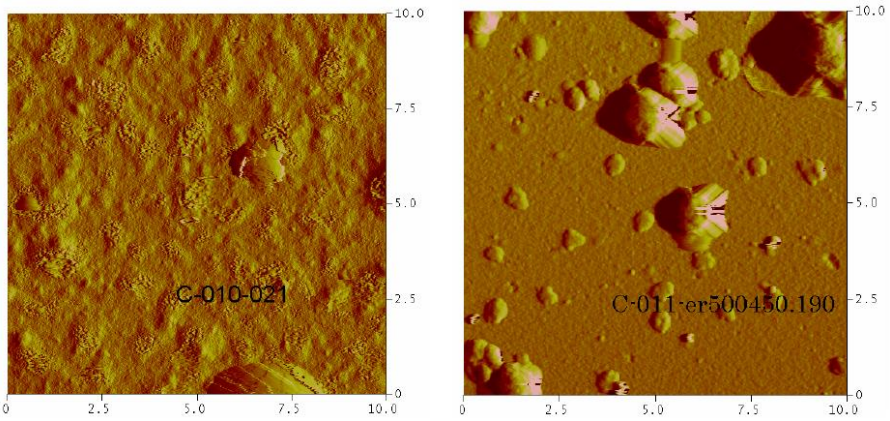

(a) (b)

Figure 2.7: 10µm x10µm AFM image (scanned under water) of a calcite surface aged in crude oil for (a) 2 days and (b) 21 days. Note the presence of a continuous adsorbate layer covering the surface in (a), which gets thicker and more stable by increasing the ageing time in (b) with the presence of large particles with irregular morphologies (asphaltenes aggregates) (Morrow and Buckley, 2006).

In the last couple of years, significant advances in imaging technologies helped visualize details of the local wettability alteration at higher resolution. Recently, FESEM (Field-Emission SEM) was used to image the asphaltenes deposition i.e. the wettability "footprint", on microparticle faces in dry conditions, which are revealed after the removal of the fluids (oil and brine) with mild solvents (Knackstedt et al., 2011, Marathe et al., 2012, Dodd et al., 2014, Idowu et al., 2015).

Schmatz et al. (2015) used a combination of the cryo-BIB (broad ion-beam), SEM, and EDX (energy-dispersive X-ray) analysis techniques to image details of the pore-scale fluid-fluid-solid contacts at the nanoscale in a mixed-wet sandstone. All the observed oil-water-rock contacts correspond to one (or are a combination) of three distinct configurations (Figure 2.8). Moreover, they were able to directly measure contact angles using serial sectioning technique when the three-phase contact line was distinguishable (category (a) in Figure 2.8). However, this was far from being straightforward due to the complex local geometries at the nanoscale.

Figure 2.8: The observed oil-water-rock contacts which fall in three different categories: (a) a conventional three-phase contact line; (b) a thin water film keeping the solid surface from direct contact with oil; and (c) a local oil-rock pinning at geometrical and chemical heterogeneities (asperities) (Schmatz et al., 2015).

Idowu et al. (2015) proposed to integrate the information from the local surface mineralogy visualised by high-resolution QEMSCAN (Quantitative Evaluation of Minerals by SEM) with the local wettability alteration displayed by FESEM. Their method suggests that this gathered "mineral-dependent" wettability information would then be incorporated into a pore network model. However, the mineralogy information they collected did not help in understanding the wettability distributions, since the two samples they chose possessed quite similar mineralogies and showed uniformly water-wet and oil-wet conditions, respectively. Moreover, it is unclear how the wettability information would be included on a pore by pore basis in a pore network model. The main challenges to address are the difficulty to capture the full heterogeneity of a mixed-wet system, as well as the absence of information on the contact angles.

2.1.4 Wettability distributions

Oil recovery in a porous medium is not only influenced by its degree of wetting change but also by the distribution of wettability among the pores. McDougall and Sorbie (1995) proposed a classification system from pore-to-pore that consists of uniform and non-uniform wettability distributions:

- Uniform wettability: homogeneous wetting behaviour throughout the rock where all the pores are either uniformly water-wet, intermediate-wet (i.e. neutral-wet) or oil-wet. Many cut-off contact angles are available in the literature to classify the intermediate-wet state, for instance between 75 and 105° (Anderson, 1986).
- Non-uniform wettability: wettability distributed non-uniformly from pore-to-pore, with coexisting fractions of water-wet and oil-wet pores in the rock. This

category is classified into sub-categories, depending on the correlation between pore wettability and size:

- Mixed-Wet Large (MWL): large pores are oil-wet, small pores are water-wet;
- Mixed-Wet Small (MWS): small pores are oil-wet, large pores are water-wet;
- Fractionally-Wet (FW): wettability randomly distributed, uncorrelated to pore size.

McDougall and Sorbie (1995) evoked as well the possible existence of non-uniform wettability within the same pore, with the presence of oil-wet and water-wet pore walls. However, they did not examine this further. The described classification system is summarised in Figure 2.9 and will be employed throughout the thesis.

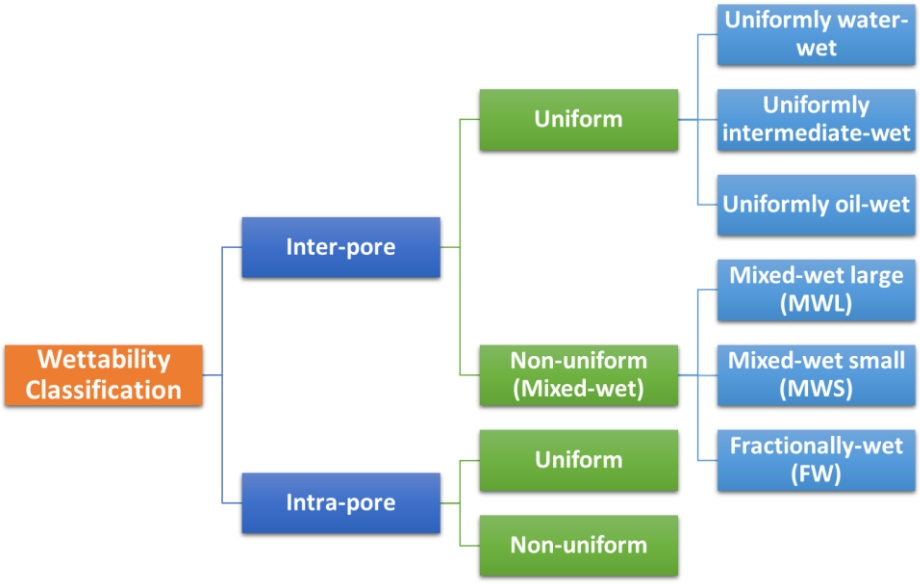

Figure 2.9: Wettability classification system, after Ryazanov (2012).

The consequences of the MWL, MWS and FW wettability distributions on the observed wettability indices (both I_{AH} and I_{USBM}) and their relationship were predicted by Dixit et al. (2000) using analytical calculations and pore network modelling. Under some simplifying assumptions, this method predicts that the FW distribution of a slightly water-wet nature coincides with the $I_{AH} = I_{USBM}$ line. On the other hand, the MWL and MWS are predicted to reside above and below the $I_{AH} = I_{USBM}$ line, respectively, as shown in Figure 2.10, with the majority of the data points lying in the MWL region.

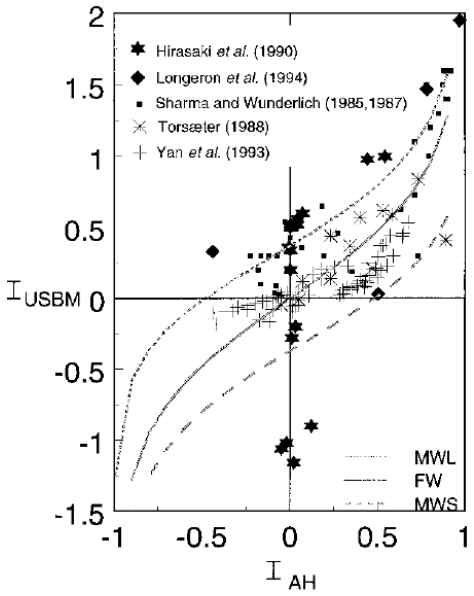

Figure 2.10: Relationship between I_{AH} and I_{USBM} indices that were measured from the same core sample by different authors. The MWL, FW and MWS lines are derived analytically (Dixit et al., 2000).

Actually, the MWL distribution, firstly introduced by Salathiel (1973), is thought to be the most widely occurring wettability distribution. The simple reason behind that is that the oil, naturally present in the larger pores, would preferentially alter their wettability. Hamon (2000) observed trends from sandstone reservoirs compatible with the MWL distribution. Indeed, wettability increased horizontally (at fixed height in the oil column) with permeability, which can be translated into larger pore spaces.

Nonetheless, there is obvious evidence from the literature of the existence of all wettability distributions in real reservoir rocks. Rueslåtten et al. (1994) classified using the I_{AH} /I_{USBM} correlation two reservoir plugs as being MWS. A thorough examination of these samples showed the presence of oil in the smallest pores, which makes the least conventional MWS condition plausible. Additionally, Skauge et al. (2007) proved that MWL, MWS and FW distributions are all theoretically compatible with the scenario suggested by Kovscek et al. (1993) involving the disjoining pressure concept (see section 2.1.1). The former demonstrate that the type of wettability distribution may be fully determined by the stability of the thin films, which in turn is controlled by the curvatures of the pore-shapes. In fact, MWL, MWS and FW distributions are related to mono-mineral rock materials consisting of concave (positive curvature), convex (negative curvature) and flat (zero curvature) pore-shapes, respectively. Additionally, they

examined a large dataset of wettability indices from intermediate-wet sandstone reservoirs, each of them falling into one of the MWL, MWS and FW categories according to Dixit et al. (2000)'s correlation. The predicted wettability distributions were further confirmed by examining the related SEM/ESEM images.

Although helpful to study homogeneous cases, these theoretical wettability distributions may be insufficient to describe complex wettability distributions that may arise in heterogeneous pore spaces, especially in microporous carbonates (refer to Section 2.2.2).

2.1.5 Effect of wettability on the residual oil saturation

Residual oil saturations after waterflooding in oil-bearing reservoirs may range from less than 1% to more than 40% (Morrow, 1990, Skauge and Ottesen, 2002). An essential feature to understanding this large scatter in oil recovery efficiencies is thought to be the wettability. Actually, the role of wettability on oil recovery is crucial as it is a property that controls the fluids displacement and trapping mechanisms, hence eventually influences the final oil distribution and residual saturation.

a) Experimental work

Salathiel (1973), for the first time, related an unexpectedly high oil recovery to a mixed-wet (large) system in a sandstone reservoir. He explained this behaviour by the persistence of oil-wetting films in the surfaces of altered wettability during waterflooding. These films would maintain the oil phase connectivity and form a continuous pathway for oil to flow to remarkably low saturations (lower than 10%).

Jadhunandan and Morrow (1995) conducted waterflooding experiments on Berea sandstone samples by injecting up to 20 pore volumes (PV) of water. They found that the residual oil saturations decreased by inducing wettability changes from strongly water-wet to a minimum at very weakly water-wet to neutral-wet conditions (Figure 2.11). Additionally, the recovery efficiency was steadily improving as more water was injected, as shown in Figure 2.11.

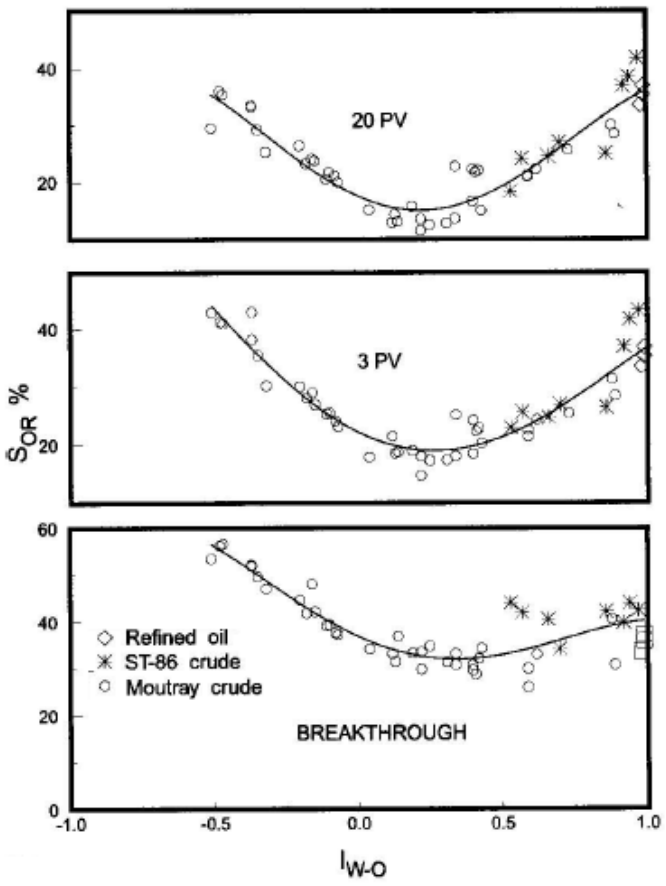

Figure 2.11: Residual oil saturation as a function of the Amott-Harvey index for three different crude oils and different PV of water injected (Jadhunandan and Morrow, 1995).

Skauge and Ottesen (2002) published oil recovery results from a wide dataset of around 30 sandstone reservoirs shown in Figure 2.12. Although they were overall consistent with Jadhunandan and Morrow (1995)'s findings, they observed a large scatter in the residual saturation data, especially at neutral-wet conditions. This reflects the inability of the used wettability indices to cover the full extent of wettability alteration, and/or is due to the difference in the experimental materials (COBR systems) and procedures.

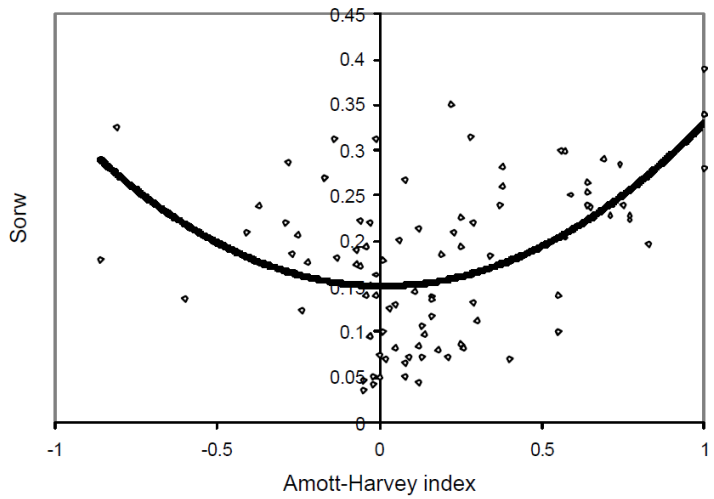

Figure 2.12: Residual oil saturation as a function of the Amott-Harvey index from 30 sandstone reservoirs (Skauge and Ottesen, 2002).

Skauge et al. (2007) extended the previous work using a wider dataset and further studied the effect of the different wettability distributions (MWL, MWS and FW) on the oil recovery from sandstone reservoirs. They observed a trend where the MWL, FW and MWS systems generally exhibited increasing residual oil saturations, in order.

b) Pore-scale simulations

Many authors have studied the effect of wettability on oil recovery using capillary-dominated pore network modelling (PNM) (McDougall and Sorbie, 1995, Blunt, 1997, Blunt, 1998, Dixit et al., 1999, Zhao et al., 2010, Ryazanov et al., 2014). In these pore-scale simulations, pore-level displacement mechanisms (piston-like, snap-off, oil layer formation, etc.), which occur depending on the governing wettability state, control the fluids distributions and trapping behaviour. These will be detailed in Chapter 3.

First, there is a need to define the residual oil saturation, S_{or}, from a simulation point of view. Ryazanov et al. (2014) distinguished between four possible definitions of S_{or}:

- The waterflood is stopped at a predefined S_{or}. This value is not a prediction of the residual oil, but should be rather referred to as the "remaining" oil saturation.
- The waterflood is stopped when a predefined final (minimum) capillary pressure, P_c^{min} is reached. This should be referred to as S_{or} at P_c^{min}.
- The waterflood is carried out until no more pore-level invasions are possible under the capillary-dominated regime. Since the capillary pressure is lowered to

infinite levels (more specifically to the lowest available entry pressure), this should be referred to as the "ultimate recovery", or S_{or} at $P_c^{min} \to -\infty$. This is considered to be a theoretical limit, probably impractical in core-flood experiments.

- The waterflood is stopped when a predefined number n of pore volumes (PV) of water is injected. This threshold is obtained from the network simulation by integrating the resulting relative permeabilities into a one-dimensional continuum scale Buckley-Leverett model (Dake, 1983). This definition of the residual oil, referred to as S_{or} at nPV, has been used extensively in the literature in order to compare with experimental data (McDougall and Sorbie, 1995, Dixit et al., 1999, Valvatne and Blunt, 2004, Zhao et al., 2010, Ryazanov et al., 2014).

McDougall and Sorbie (1995) examined the effect of both wettability distribution (FW and MWL only) and oil-wet fraction on oil recovery by simply using a regular 3D cubic network constituted of pores with circular cross-section. They concluded that for both FW and MWL, the lowest residual oil saturation following up to 20PV of water injected was reached when approximately half of the pores are oil-wet. McDougall et al. (1997) and Dixit et al. (1999) extended the latter work by introducing a regime-based framework for classifying and interpreting oil-recovery experiments depending on the underlying wettability properties (contact angles and oil-wet fraction).

Blunt (1998) used a regular cubic network with square cross-sectional pores and a parametric model to model the pore-scale wettability scenario suggested by Kovscek et al. (1993)**.** He demonstrated the complexity and non-monotonicity of the relationship between the oil recovery and wettability, characterized by the oil-wet fraction and contact angle. In fact, as shown in Figure 2.13(a), he identified four governing regimes depending on the range of contact angles:

i. Strongly water-wet: The competition between snap-off and piston-like dictates the amount of residual oil. Note that snap-off is considered as being the major trapping mechanism.
ii. Weakly water-wet: Snap-off is inhibited, and water invades throats in favour of nodes, hence this regime leads to a low trapping and a high recovery.

iii. Weakly oil-wet: Water preferably invades large throats and pores, hence it tends to surround the wetting oil phase. As a result, this regime is characterized by a high trapping, leading to a poor recovery.

iv. Strongly oil-wet: Oil layers are formed in oil-wet pores and enhance the recovery. The ultimate residual oil saturations reach very low values, but only following high PV of water injected.

Additionally, as shown in Figure 2.13(b), Blunt (1998) observed that only at an oil-wet fraction of around 0.55, when a connected pathway of oil-wet pores is formed throughout the network, that the oil recovery starts improving. The recovery then gets better by means of slow displacements through connecting oil layers.

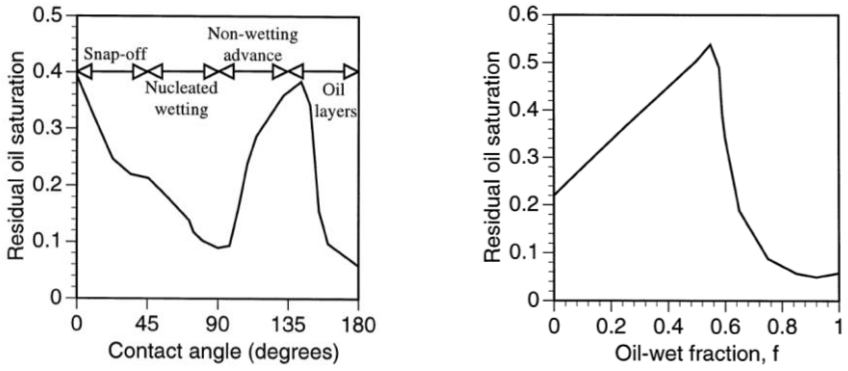

(a) (b)

Figure 2.13: Ultimate residual oil saturation as a function of contact angle (left) and oil-wet fraction (right) (Blunt, 1998). Note that "Snap-off", "Nucleated wetting", "Non-wetting advance" and "Oil layers" correspond to the regimes i., ii., iii. and iv. as described in the text, respectively.

Oren et al. (1998) reconstructed a geologically realistic sandstone network based on thin-section data analysis. Their model has been extensively used in attempts to reproduce experimental trends. Jackson et al. (2003), Valvatne and Blunt (2004) and Zhao et al. (2010) aimed at reproducing the experiment conducted by Jadhunandan and Morrow (1995) by calculating S_{or} at 3PV. Although the simulations are in fairly good agreement with the experiment (see Figure 2.14), the maximum oil recovery is slightly moved to the more oil-wet regime (lower Amott-Harvey index). Note that the wettability was used as a tuning parameter to match the experiment: the oil-wet fraction and the distribution of oil-wet contact angles were varied to reproduce the Amott water and oil

indices, respectively. Furthermore, Zhao et al. (2010) examined the impact of the distribution of contact angles and the oil-wet fraction on the residual oil saturation after 3PV of water injected using several networks with different pore systems derived from micro-CT images of real rocks. They concluded that for a uniformly-wet state, the residual oil saturations decrease with higher contact angles until it reaches a plateau for slightly oil-wet conditions at around $100°$ where the best oil recovery is obtained. However, for a mixed-wet state, the fraction of oil-wet pores has a more significant impact on oil recovery than the contact angle. In fact, a large fraction of oil-wet pores leads to the lowest residual oil saturation. Additionally, they observed that the effect of the pore structure on the relationship between wettability and oil recovery is weak.

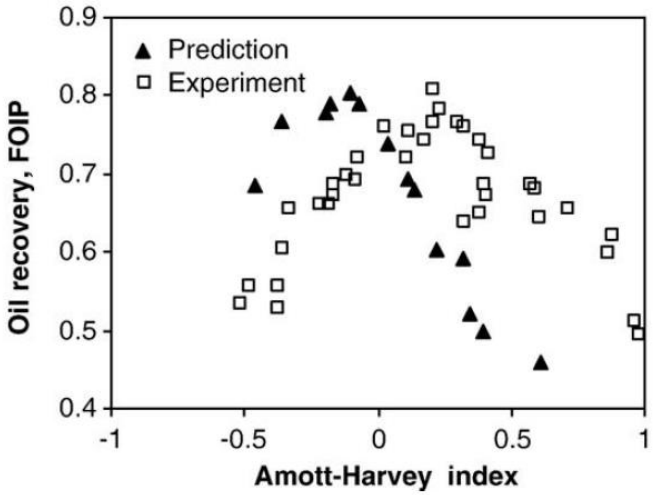

Figure 2.14: Comparison between PNM simulation and experimental data from Jadhunandan and Morrow (1995) of the oil recovery (the Fraction of Oil In Place) as a function of wettability (Amott-Harvey index) following a 3PV injection of water (Zhao et al., 2010).

Ryazanov et al. (2014) used the pore-network modelling tool described in Chapter 3 to obtain a better match of the Jadhunandan and Morrow (1995) experiment compared to previous studies, including at different PV throughput (Figure 2.15). They also visualised the 3D structure of the residual oil in mixed-wet systems as a function of wettability. They were able to observe clear variations in the nature of the residual oil, depending on the system's wettability condition. On the one hand, for moderately water-wet conditions, the residual oil is detected in the bulk space of pores. Additionally, its saturation is high at relatively small numbers of PV of water injected. On the other hand, for moderately oil-wet conditions, the ultimate residual oil resides in a large number of

oil layers with relatively low volume, and in few bulk spaces. Moreover, S_{or} slowly increases with higher PV injected since the flow is mainly controlled by the connecting oil layers.

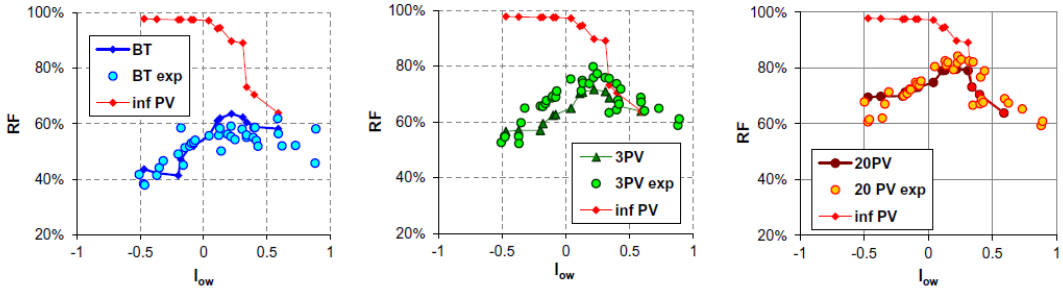

Figure 2.15: Comparison between PNM simulation and experimental data from Jadhunandan and Morrow (1995) of the recovery factor (RF) as a function of wettability (Amott-Harvey index) at breakthrough (BT), and following 3PV and 20PV injection of water. The infinite (inf) PV case was also included on each figure (Ryazanov et al., 2014).

2.2 Carbonates and microporosity

Around half of the world's remaining hydrocarbon reserves lie in carbonate reservoirs (Roehl and Choquette, 2012). The carbonates' complexity resides in their heterogeneous pore space, with pore sizes spanning multiple length-scales. Micropores are particularly interesting to examine as they may dominate the connected pore system in many carbonate reservoirs, accounting for up to 100% of the total porosity (Cantrell and Hagerty, 1999). Among many definitions of micropores available in the literature, we use the definition suggested by Cantrell and Hagerty (1999) as pores <5 µm in radius. Nonetheless, microporosity has been poorly understood and its contribution to flow has often been neglected, since micropores are usually assumed to contain irreducible water due to their small size and the resulting high capillary pressures required for the oil to enter them, hence they are naturally assumed to be water-wet. However, the presence of hydrocarbons in micropores was identified (Al-Yousef et al., 1995, Clerke, 2009, Knackstedt et al., 2011, Fung et al., 2011, Clerke et al., 2014, Dodd et al., 2014), which may result in a potential oil-wet state. This has driven research to analyse the wettability of micropores, thought to be the key to maximise oil recovery from microporous carbonates, which is the main topic of this thesis.

2.2.1 Composition and structure

Despite a significant variability in pore structure, carbonates possess a simple mineralogy compared to sandstones, being mainly dominated by calcite, and to a lesser extent by dolomite. These minerals typically have a slightly basic nature and exhibit a positive surface charge (Lichaa et al., 1993, Morrow and Buckley, 2006)**.** Morrow and Buckley (2006) state that this is generally true when the pH of the brine in contact with the surface is around neutral.

Microporosity in carbonates often occurs within micrite (microcrystalline calcite) crystals of rhombic shape (Figure 2.16(a)). It is thought to have formed due to diagenesis i.e. carbonate dissolution, transport and precipitation (cementation) mechanisms. Diagenetic processes require an aqueous medium, thus are not favoured in presence of the oil and predominant oil-wet conditions (Cox et al., 2010, Heasley et al., 2000). Cantrell and Hagerty (1999) suggested that several diagenetic mechanisms account for the formation of microporosity. Moreover, they observed that micropores may exist in many types, namely as (a) microporous grains, (b) microporous matrix, (c) microporous fibrous to bladed cements, and (d) microporous equant cements; as illustrated in Figure 2.17. Whatever the type, a magnified view shows an identical sponge-like microporous structure, not only well inter-connected but also connecting up the meso/macro-porosity (Figure 2.16(b)). Individually, the micropores usually exhibit a distinctive morphology consisting of flat and platy shape. The micrite crystals sizes, shapes and packing pattern influence the micropores morphology (Harland et al., 2015). Additionally, Cantrell and Hagerty (1999) state that the wide variations in the microporosity types and abundance (ranging between 0 and 100% of the total porosity), are mainly due to the depositional texture (in particular the presence or absence of mud).

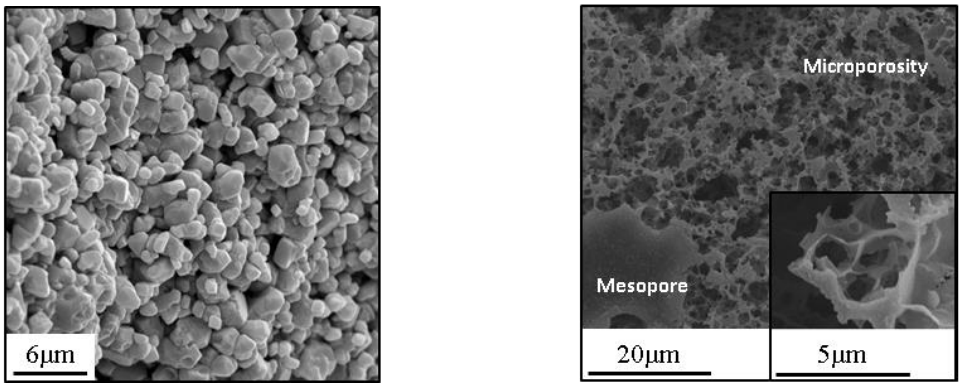

(a) (b)

Figure 2.16: SEM images from microporous carbonates (a) displaying the rhomboidal micrite crystals and (b) showing the structure of the microporous network and its connection to the larger mesopore (using epoxy resin cast) (Harland et al., 2015).

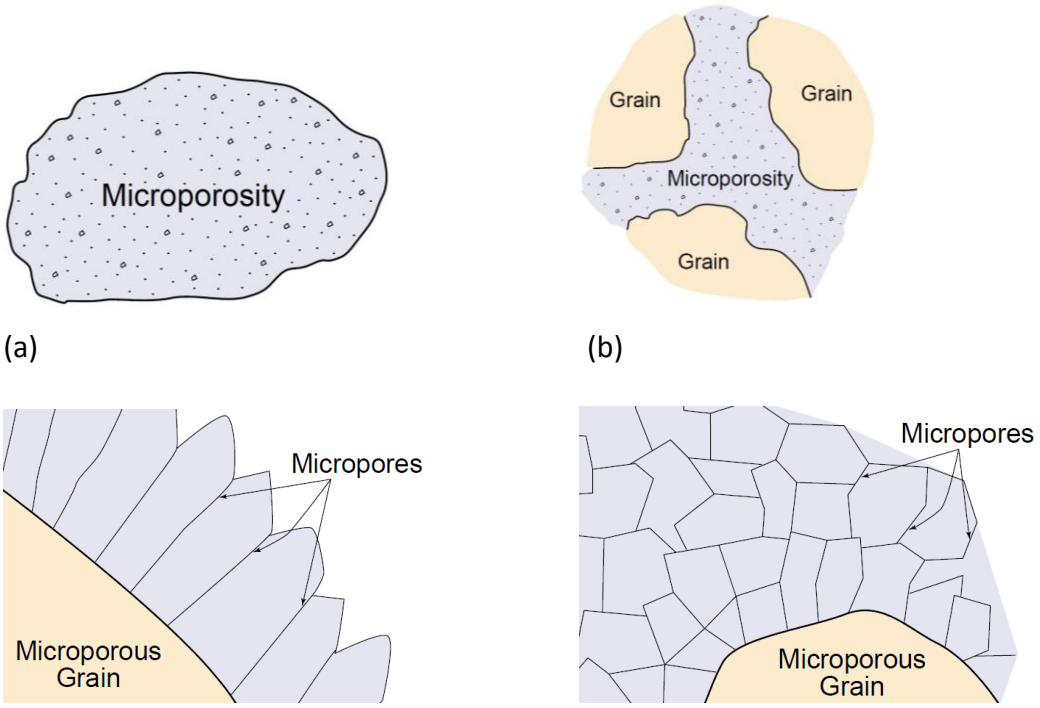

(a) (b)

(c) (d)

Figure 2.17: Illustration of the four different microporosity types observed by Cantrell and Hagerty (1999): (a) microporous grains, where the fully micritised grains seem like sponges; (b) microporous matrix, consisting of a network of connected micropores; (c) microporous fibrous to bladed cements, where micropores are found between cement blades; and (d) microporous equant cements, with the appearance of micropores between cement crystals.

The complex heterogeneity of carbonate pores has led many authors to arrange them into pore classes according to their structure, porosity and permeability. Naturally, the more heterogeneous carbonates would contain more pore classes. Several classification systems exist in the literature, constituted by tens of pore types that can be visually identified from rock images (Choquette and Pray, 1970, Lucia, 1983, Lønøy, 2006). It is well established that flow properties vary significantly with pore classes (Skauge et al., 2006). Additionally, this categorisation enhances our understanding of the relationship between some of the petrophysical properties for each class (e.g. porosity, permeability, etc.) and the resulting residual oil saturations after waterflooding (Pourmohammadi et al., 2008).

2.2.2 Wettability

Earlier in section 2.1, we described more generally the wettability for various surfaces and the link with surface properties. In this section, we focus on the particular case of the wettability of carbonates.

a) Average core-scale wettability

Many studies using the USBM and Amott tests confirm that carbonate reservoir rocks show intermediate to weakly oil-wet behaviour at the core scale (Cuiec and Yahya, 1991, Lichaa et al., 1993, Al-Yousef et al., 1995, Skauge et al., 2007, Okasha et al., 2007). Nonetheless, Okasha et al. (2007) observed an intermediate to slightly water-wet state for rocks below the OWC. This is consistent with the general trend of higher water-wetness with decreasing height in the oil column. Typically, while carbonate reservoir rocks could not be changed further than weakly water-wet state after cleaning, no matter how strong the cleaning procedure was, their "preserved" wettability state could be readily restored after ageing in crude oil (Cuiec and Yahya, 1991, Lichaa et al., 1993). Morrow and Buckley (2006) succeeded for the first time to identify a set of carbonate rocks that exhibited a very strongly water-wet (VSWW) condition after thorough cleaning. This result is important as it provides a clear base case to analyse the effect of wettability change on oil recovery.

b) Factors affecting wettability

In fact, the weak affinity of carbonate surfaces to oil is thought to be primarily a result of acid/base interactions between the slightly acidic components of the crude oil

(negatively charged) and the slightly basic carbonate surface (positively charged) (Lichaa et al., 1993, Al-Yousef et al., 1995).

Morrow and Buckley (2006) thoroughly studied the wettability state of carbonates by directly measuring contact angles on smooth calcite surfaces using different surface preparation techniques, crude oils and brines. Overall, they observed that the major parameter affecting wettability of calcite minerals is the nature of the crude oil. This is in contrast with an earlier study (Cuiec and Yahya, 1991) which came to the conclusion that neither the crude oil nor the ageing temperature and pressure affected the carbonates' wettability, but that it was mainly controlled by the surface properties. Morrow and Buckley (2006) additionally observed that the amount of asphaltenes exhibited a negative correlation to the measured contact angles, which seems counterintuitive. They explain this trend by the fact that the kinetics of adsorption are slow for compounds as heavy as the asphaltenes. In contrast, the effect of the brine properties was found to be unimportant as no clear trend emerged. In a second series of experiments, the same authors tested the effect of crude oil composition, initial water saturation and ageing time on the wettability of two carbonate samples using spontaneous imbibition curves. They concluded that the acid number of a crude oil is the most telling property about its wetting alteration potential on carbonate surfaces. They also confirmed that the ageing time and initial water saturation are major influential parameters for carbonates, and they exhibit positive and negative correlations with the wettability alteration, respectively, as expected.

c) Pore-to-pore wettability

Besides, the inter-pore wettability distribution in carbonates is widely recognised as being non-uniform, where all wettability states (oil-wet, intermediate-wet and water-wet) may coexist (Cuiec and Yahya, 1991, Lichaa et al., 1993, Al-Yousef et al., 1995). For instance, Cuiec and Yahya (1991) calculated a fraction of oil-wet surfaces equal to 0.78 and 0.62 for the preserved and restored states, respectively, of a middle-eastern carbonate rock. However, the wettability distribution within the heterogeneous and multi-scale pore space of carbonates is largely unknown. There are common claims that micropores always maintain their strong affinity to water, since they have never been in contact with oil, and that carbonates exhibit a typical MWL wettability distribution (Lichaa et al., 1993, Fassi-Fihri et al., 1995). Indeed, Fassi-Fihri et al. (1995) examined a

Middle Eastern carbonate reservoir and observed that micropores were water-wet, in contrast to oil-wet mesopores. Yet oil has been detected within micropores in carbonate rocks, making oil-wet conditions plausible (Al-Yousef et al., 1995, Clerke, 2009, Knackstedt et al., 2011, Fung et al., 2011, Clerke et al., 2014, Dodd et al., 2014). Al-Yousef et al. (1995) performed a centrifugation in crude oil of a cleaned and initially water-filled microporous carbonate core and observed that most of the microporosity (diameter ranging between 1 and 10 microns) remained filled with water. Nonetheless, following a two-weeks ageing and a further centrifugation in crude oil, the latter was detected in micropores using cryo-SEM imaging.

Skauge et al. (2006) examined the wettability of relatively homogeneous carbonate samples, each consisting of a unique and different pore class but are mostly microporous. They found that following core-flooding and a 4-weeks aging procedure, nearly all the samples exhibited MWS behaviour according to the combined Amott/USBM test. This means that the smallest pores were oil-wet, which is contrary to the common assumptions. As an exception, one unique sample was identified as FW with a weak inclination to MWS.

Marathe et al. (2012) used Field-Emission SEM (FESEM) imaging to identify the existence of a pattern of wettability alteration within micropores in reservoir carbonates. They suggested that the wettability alteration on rhombic micrite is face-selective, where the anhedral ("curved, rough and poorly formed") faces are preferentially oil-wet, as opposed to the euhedral ("flat, smooth, well-formed") which remained water-wet (see Figure 2.18).

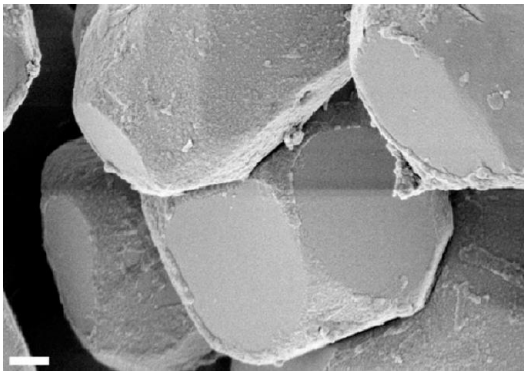

Figure 2.18: FESEM imaging (250 nm scale bars) of the oil deposits (i.e. the footprint of the wettability alteration) on calcite micro-particles in carbonate rocks (Marathe et al., 2012).

Juri et al. (2016) developed a new approach that characterises the wettability of carbonate rocks using stochastic inversion of multi-scale PNM to predict relative permeabilities. They found that not only micropores could be oil-wet but also the advancing contact angles in micropores could be higher than in larger pores. More generally, the authors found that the wettability distribution in carbonates was uncorrelated to pore size.

2.2.3 Effect of wettability on oil recovery

The relationship between wettability and oil recovery for carbonates is poorly understood. This is mainly due to the heterogeneity of the pore space at multiple scales, as well as the inability to experimentally restore the reservoir's initial water saturation and wettability state. Few studies in the literature attempted to address this issue, in contrast with a more extensive research on sandstones.

Masalmeh (2002) analysed a broad data from carbonate fields. As expected, they witnessed the decrease of the residual oil saturation following ageing of water-wet samples from 20-30% to around 5-10%. Nonetheless, they did not find any clear correlation of residual oil to initial oil saturations (S_{or}/S_{oi}) for mixed-wet carbonate samples, as opposed to a linear increase for water-wet sandstones.

Skauge et al. (2006) examined experimentally the oil recovery after waterflooding from a broad carbonate (mostly microporous) dataset. Interestingly, they observed that carbonates with low-permeability (and low porosity), which could be related to a high microporosity content, may exhibit a good oil recovery efficiency (e.g. 45% of the oil was recovered from a rock with a permeability as low as 0.7mD). This was explained by a good connectivity of the porous space. Moreover, as expected, the residual oil saturation was lower at aged conditions (intermediate to slightly oil-wet) than at the initial cleaned state, for almost all the samples. The change was surprisingly significant for most of the aged microporous samples, all of these falling into the MWS distribution (Section 2.1.4), with the recovery factor increasing as much as almost three times the initial value.

Tie and Morrow (2005) studied the response to wettability change of three initially very strongly water-wet carbonate samples, two classified as "grainstones" (mud-free and grain supported) with different heterogeneities and one as "boundstone" (bound by its

components during deposition). They aged the rocks in crude oil. Then, depending on the nature of the oil displaced by water during imbibition, called "probe" oil, they obtained three different wettability states:

- MXW: typical mixed-wettability state where the crude oil is the "probe" oil.
- MXW-F: the crude oil is removed first by a solvent, leaving a film of adsorbed polar components (F); then the solvent is in turn replaced by a mineral oil (characterised by its low solvency for its asphaltenes) used as "probe".
- MXW-DF: the crude oil is directly flooded (DF) by the mineral "probe" oil. Omitting the use of solvent enhances destabilisation and surface precipitation of asphaltenes by direct contact between crude and mineral oils.

As shown from Figure 2.19, MXW, MXW-F and MXW-DF tend to increase the rock's oil-wetness, in sequence, up to neutral-wet conditions. Additionally, they observed that the two "grainstones" exhibited trends similar to those reported for sandstones by Jadhunandan and Morrow (1995). In fact, as shown in Figure 2.19, the maximal oil recovery was reached when wettability was slightly water-wet to intermediate-wet. Note that following wettability alteration, the oil saturation reached up to half the initial VSWW value. However, the "boundstone" did not exhibit any clear correlation between wettability and oil recovery. Although this is ascribed to the difference in pore structure, the variations in the preparation methods should also be taken into account.

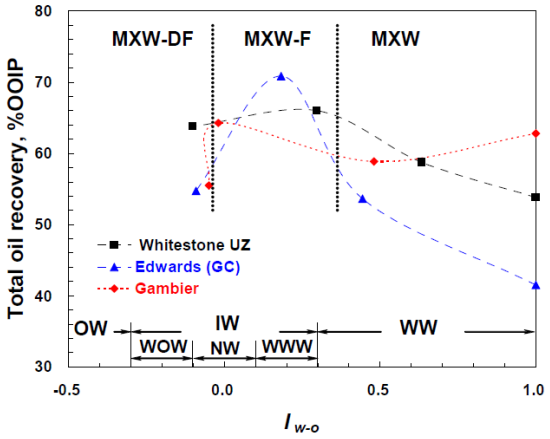

Figure 2.19: Oil recovery for three different carbonate rocks (two "grainstones" in black and blue, and a "boundstone" in red) as a function of the Amott-Harvey index. Three wettability states (MXW, MXW-F and MXW-DF, refer to text) are compared to the VSWW base case. WW: water-wet; IW: intermediate-wet (WWW: weakly water-wet; NW: neutral-wet; WOW: weakly oil-wet); OW: oil-wet (Tie and Morrow, 2005).

2.2.4 Multi-scale modelling

The pore-space of carbonate rocks is particularly difficult to numerically reproduce due to the multiple orders of change in the pore-size distribution. Indeed, common imaging technologies fail to capture the heterogeneous nature of such multi-scale pore systems. The challenge resides in combining data from distinct scales of porosity obtained separately using imaging at different resolutions. This issue has been tackled by many authors in the recent years (Roth et al., 2011, Jiang et al., 2013, Bultreys et al., 2015, Prodanović et al., 2015, Harland et al., 2015).

Jiang et al. (2013) suggested a multi-scale pore-network extraction methodology for reconstruction of multi-scale carbonate rocks. The workflow can be summarised in four successive steps:

- Two 3D pore networks are extracted from micro-CT images at two distinct resolutions: (i) a fine-scale network extracted at one length-scale and (ii) a coarse-scale network extracted at a higher length-scale. Note that the two networks may have some overlap in pore sizes.
- A sub-network is extracted from the original coarse-scale network, its domain corresponding to the nesting domain for the target multi-scale network.
- A stochastic fine-scale network is statistically generated within the same nesting domain, without overlapping with the elements of the coarse-scale network. It is equivalent to the original network in terms of geometry, topology and correlations.
- The fine-scale and coarse-scale networks are integrated into a single two-scale network. Indeed, after superimposing the two networks, the fine-scale bonds intersecting with the coarse-scale bonds are suppressed. Then, the cross-scale connections are ensured by adding connecting fine-scale bonds between coarse-scale nodes and neighbouring fine-scale nodes.

Bultreys et al. (2015) developed a new pore network modelling technique that couples the microporosity and the macroporosity. It consists in incorporating into a standard macroporous network some notional connecting micropores or “micro-links”. The latter are dealt with as a continuous porous medium with pre-assigned petrophysical

properties, and may join-up initially disconnected macroporous networks to allow drainage to occur.

Harland et al. (2015) developed an original object-based rock reconstruction methodology which reproduces the micro-scale structure of microporous carbonates. The workflow consists in the analysis of 2D SEM image data of carbonate samples to capture the basic structural features of micropores. This information is then used to populate 3D digital images with micrite crystals of varying shapes, sizes and packing patterns. Afterwards, single-phase and multi-phase simulations are run on the obtained 3D image (using Lattice-Boltzmann) and a network extracted from it (using PNM), respectively. They showed that the percentage of microporosity among the total porosity strongly influenced the single-phase permeability. For multi-phase imbibition calculations, they considered either a uniformly water-wet distribution or fractionally-wet (FW), with half of the pores oil-wet and the other half water-wet. The authors showed that both the wettability distribution and the network's homogeneity i.e. proportion of microporosity, affected the oil recovery. Indeed, increasing the network's homogeneity in water-wet conditions resulted in a better recovery due to a higher sweep efficiency, which is in accordance with earlier observations (Clerke, 2009, Clerke et al., 2014).

Note that micropores may supply the connectivity and fluid pathway between otherwise disconnected larger pores within some multi-scale pore network models (Roth et al., 2011, Jiang et al., 2013, Bultreys et al., 2015).

2.3 Discussion

Having reviewed the literature on wettability and microporous carbonates, we identify some needs that few studies have attempted to address, which coincide with our objectives stated in Chapter 1:

a) Model the wettability distribution patterns identified by Marathe et al. (2012) in microporous carbonates, where the wettability is dependent on the pore shape.
b) Assess the impact of the wettability of micropores on oil recovery in multi-scale carbonate networks, especially when micropores control the network's connectivity.

c) Suggest a pore-scale mechanism that may be responsible for oil migration into initially strongly-water-wet micropores. Actually, an oil-wet state in micropores may have developed over geological time either (i) by means of calcite cementation as some pores get smaller, or (ii) in the upper regions of exceptionally large oil columns where high enough capillary pressures are reached, or (iii) if the micropores undergo progressive wettability changes during oil migration, which reduces their capillary entry level and makes them more prone to oil invasion. Scenario (i) is the least likely to have happened, since as previously stated in Section 2.2.1, the cementation process is slowed down in the presence of the oleic phase. We will focus in Chapter 5 on scenario (iii), which we think is perfectly plausible.

Chapter 3 : Pore network model

3.1 Introduction

Pore Network Modelling (PNM) is a physically-based multi-phase flow modelling tool that offers a computationally-cheap simulation workflow to derive petrophysical properties e.g. relative permeabilities, capillary pressures, residual oil saturations, etc. Their input networks are approximations of the pore space, either generated numerically or extracted from 3D images of real core samples (see Figure 3.1). The utility of Pore Network Models resides in the ability to incorporate in their simplified geometries appropriate pore-level physics of displacement mechanisms, e.g. fluid films and layers, etc. This leads to a better understanding of complex flow and transport mechanisms by allowing to "*examine the expected consequences of various pore scale phenomena at the macroscopic scale"* (Dixit et al., 1999)**.** Indeed, PNM assists reservoir engineers in gaining insight into laboratory experiments, reservoir behaviour and recovery mechanisms, by deriving and explaining macroscopic properties. Additionally, compared to Direct Numerical Simulations, it is computationally cheaper, meaning that it can support bigger models (larger volume and range of pore sizes), thus providing a better "representativity" of the core sample.

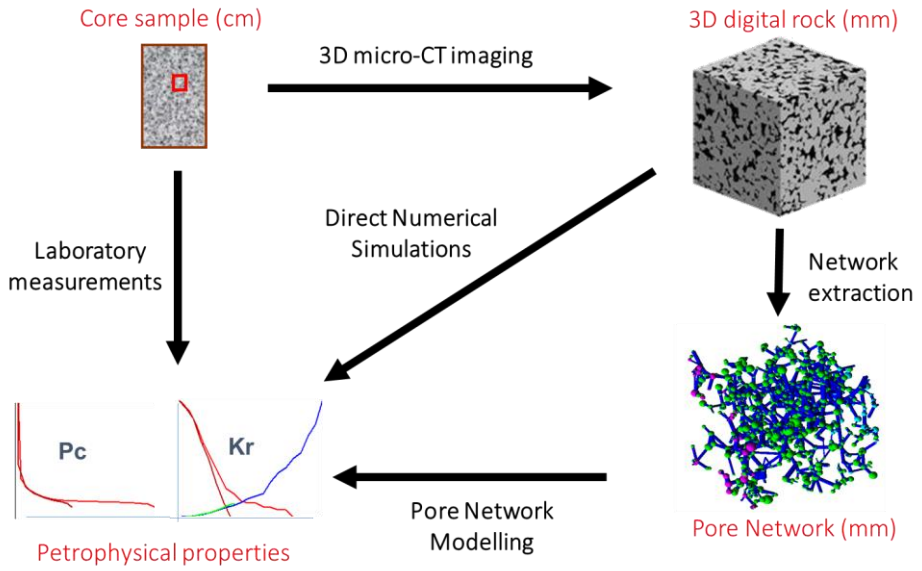

Figure 3.1: Different workflows leading from a core sample to relative permeability and capillary pressure curves, after Ryazanov (2012).

3.2 Pore Network modelling tool

The quasi-static two-phase flow pore network modelling tool used in this study is similar to previously developed models (Oren et al., 1998, Patzek, 2001, Valvatne and Blunt, 2004). It has been thoroughly described by Ryazanov (Ryazanov et al., 2009, Ryazanov, 2012, Ryazanov et al., 2014). It requires as input networks consisting of pore bodies (nodes) connected by pore throats (bonds). Throughout this work, we generically refer to both pore bodies and pore throats as pores. The porosity of the network is simply estimated using the total volume of pores relative to the volume of the enclosing domain. Permeabilities are computed based on the total flow through the network for the phase cluster of interest, for a given applied pressure gradient and application of Darcy's law.

The input networks can be either synthetically generated or extracted from 3D micro-CT images. Extracted networks are topologically and geometrically equivalent representations of the porous media. On the one hand, they preserve the pore-space connectivity through identification of the nodes that represent the main junctions; and the bonds that consist of the remaining narrower connections. On the other hand, network extraction preserves the main geometrical pore properties (inscribed and hydraulic radii, shape factor, volume, etc.) by idealising pore shapes into straight tubes with simple cross-sections (e.g. circle, triangle, star). This leads to easy analytical calculations of flow properties.

3.2.1 Pore shapes

The shape of the pore cross-section is important for conductance and capillary entry pressure computations. Additionally, pore shapes are central to the models that we developed in the following chapters, since they may control the wettability and primary drainage patterns. Although in earlier works, pore shapes have been approximated as circles, these fail to capture important features such as corner films and layers found in angular pores. Our pore network simulator takes into account a wide range of pore sizes, including circles, triangles, squares and n-cornered stars. This section summarises the methodology for idealising the pore shapes using information from the input network. The equations for single and two-phase conductances and the capillary entry pressures for each of the idealised shapes were thoroughly described by Ryazanov (2012).

a) Circle-Triangle-Square (CTS)

The pores cross-sectional shape is usually characterised using the shape factor, G, to idealise it as a Circle, Triangle or Square (the CTS approach). The shape factor is defined as $G = {A}/{L^2}$, where A and L are the pore cross-section area and perimeter, respectively. Depending on the value of G, the cross-sectional shape is approximated as one of the idealised shapes, using the following rules:

- if $G \leq \frac{\sqrt{3}}{36}$: (Arbitrary) Triangle, keeping the same G.
- if $\frac{\sqrt{3}}{36} \leq G \leq \frac{1}{16}$: Square with $G = \frac{1}{16}$ (approximation).
- if $\frac{1}{16} < G$: Circle with $G = \frac{1}{4\pi}$ (approximation).

The main shortcoming of the CTS method is that it leads strictly to convex pores, thus fails to represent non-convex pores that exist in real pore spaces. We may use the dimensionless hydraulic radius, H, as an indicator of the convexity of a shape (Ryazanov, 2012). H is defined as $H = (A/L)/R_{ins}$, where A and L are as defined above, and R_{ins} is the inscribed radius. Notice that shapes with $H \geq 1/2$ are (generally) convex. Since all the CTS shapes are characterised by $H = 1/2$, they are labelled as convex.

b) n-cornered star shapes

In addition to the shape factor, we use the previously defined dimensionless hydraulic radius, H, to idealise the pore shape as regular non-convex n-cornered stars, along with the CTS (Helland et al., 2008, Ryazanov et al., 2009, Ryazanov, 2012, Ryazanov et al., 2014). As shown in Figure 3.2, regular n-cornered stars are characterised by two parameters, the number of corners, n, and the half-angle γ. While several (n, γ) pairs may exist for a given shape factor G, a given (G, H) pair generally satisfies a unique (n, γ) i.e. a single regular star shape (Helland et al., 2008). However, the working network needs to specifically include an extra information on the hydraulic radius. Practically, this corresponds to an additional column in the input file.

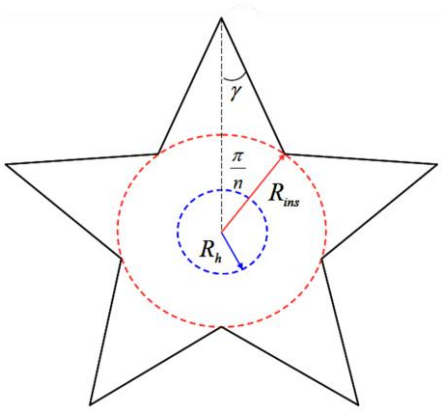

Figure 3.2: An example of a n-cornered star shape ($n = 5$), with inscribed and hydraulic radii R_{ins} and R_h, respectively, and half-angle γ.

The methodology for shapes characterisation from the (G, H) pair is illustrated in Figure 3.3, and described as follows:

- For $H < 1/2$, the curves correspond to star shapes with different number of corners. Keeping the same value of the shape factor G as the initial arbitrary shape, two number of corners values, n_1 and n_2 are possible. The nearest n-cornered star curve is chosen, which corresponds to an approximated H, slightly different from the initial shape's value. The half-angle γ is then deduced, and the idealised shape is fully characterised.
- The vertical line $H = 1/2$ represents the arbitrary triangles ($n = 3$), along with regular shapes like n-cornered polygons, including squares ($n = 4$) and circles ($n = +\infty$). Note that the polygons are a limiting case of stars, satisfying the following condition: $\gamma = \frac{\pi}{2} - \frac{\pi}{n}$.
- The curves at $H > 1/2$ correspond to some more convex shapes that will not be taken into account in this study.

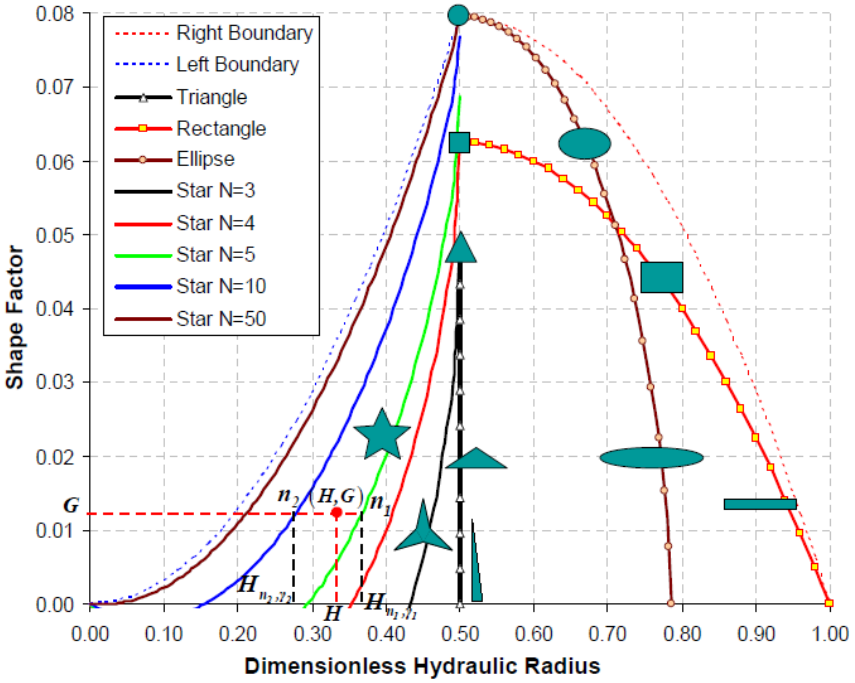

Figure 3.3: Shape factor, G, as a function of dimensionless hydraulic radius, H, for some cross-sectional shapes. The right and left boundaries represent the shapes theoretical limiting (G, H) pairs (Ryazanov, 2012).

3.2.2 Fluid configuration

The network modelling tool is a two-phase flow model, for which oil and water are the two phases of interest. The fluid configuration of every pore may consist of different fluid elements, such as oil/water bulk (centre of the pore), oil/water corner films and oil layers (sandwiched between water in the corners and bulk). All the possible cross-sectional fluid configurations incorporated in the model are shown in Figure 3.4. Note that we define a phase cluster as an interconnected set of pores that contains at least one fluid element of the corresponding phase. Since a single pore may contain elements from each of the two phases, it can be part of both an oil and a water cluster.

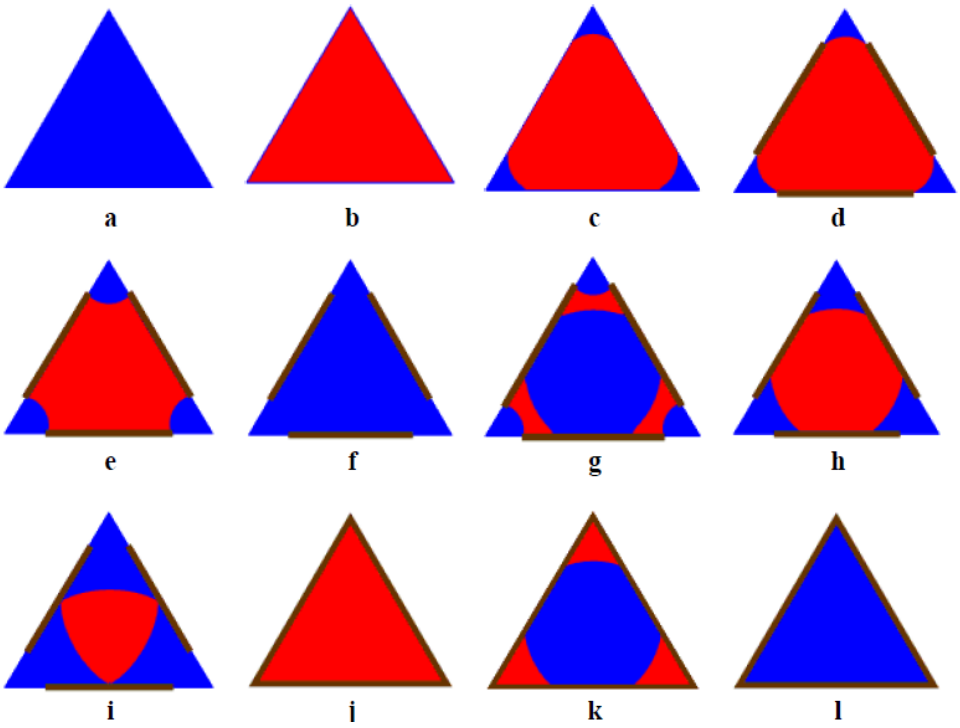

Figure 3.4: Possible cross-sectional fluid configurations following primary drainage and imbibition for regular n-cornered star shapes (represented by equilateral triangles for simplicity). Oil is red; water is blue and surfaces of altered wettability are brown (Ryazanov, 2012).

3.2.3 Pore-level displacements

The displacement process is quasi-static, as the capillary forces are assumed to dominate over viscous forces i.e. the capillary number satisfies the following condition (Blunt and Scher, 1995):

$$N_c = \frac{q\mu}{\sigma_{ow}} \leq 10^{-4} \qquad (3.1)$$

where q is the Darcy flux, μ is the viscosity and σ_{ow} the oil-water interfacial tension. The capillary-driven flow is simulated using a classical Invasion Percolation (IP) process with trapping, where an invading phase is eligible to displace a defending phase from a pore if the pore satisfies two conditions:

i. accessible, i.e. it has at least a neighbouring pore that is part of the invading cluster and is connected to the inlet; we may distinguish between a strong or a weak accessibility condition, where the connection to the inlet is exclusively

fulfilled through a neighbouring bulk fluid element or can additionally be realised through a neighbouring film, respectively.

ii. non-trapped, i.e. it is part of a defending cluster that is connected to the outlet.

The quasi-static IP process is driven by a gradual change of the overall capillary pressure. Each capillary pressure corresponds to an equilibrium fluid configuration within a pore (Figure 3.4). This is determined by pore-level displacements that occur sequentially according to well-defined capillary pressure criteria. Indeed, the so-called MS-P theory (Mayer and Stowe 1965) assigns to each pore displacement a capillary entry pressure, $P_{entry} = \frac{\sigma_{ow}}{R_{entry}}$, where R_{entry} is the entry radius of the specific shape and displacement. A pore displacement occurs when its entry pressure is overcome and the pore satisfies conditions i. and ii. described above.

Lenormand et al. (1983) identified 3 distinct displacement mechanisms as shown in Figure 3.5: Piston-like (PL), snap-off (SO) and pore body filling (PBF). Further, we identify a 4th distinct pore-displacement, namely the oil layers formation and collapse mechanism. Note that when the invading phase is the non-wetting wetting phase, it is called drainage. Otherwise, we refer to it as imbibition. Further, for the sake of simplicity, we consider water to be the wetting phase and oil the non-wetting phase in the description below.

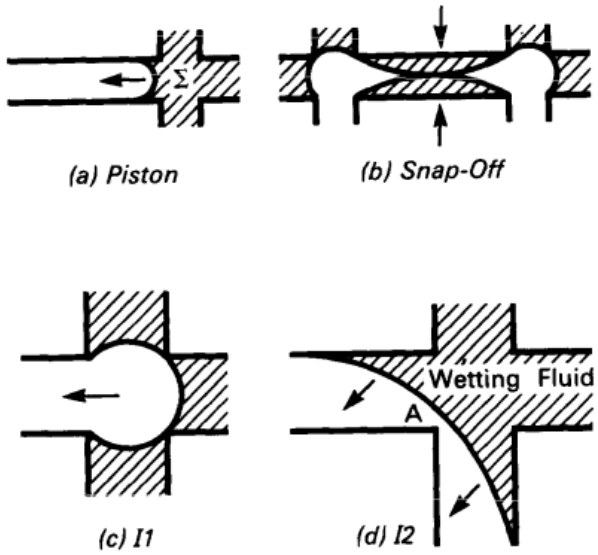

Figure 3.5: Pore-level displacement mechanisms, (a) piston-like, (b) snap-off, (c) and (d) I1 and I2 PBF events, with 1 and 2 adjacent pores filled with the non-wetting oil phase, respectively, as observed from micromodel experiments by Lenormand et al. (1983).

a) Piston-like (PL)

In this type of displacement, the bulk fluid element is displaced in a piston-fashion from the centre of the pore. It is the only displacement modelled during drainage, and can occur as well during imbibition. PL requires a strong accessibility condition i.e. the pore needs to have at least a neighbouring pore that is bulk-filled with the invading phase and connected to the inlet; Note that a phenomenon, that we refer to as "bypassing", is likely to occur during imbibition when water in the corner is present. As illustrated in Figure 3.6(a), it consists of a PL filling when the neighbouring pore that is bulk-filled with water is connected to the inlet through corner water rather than bulk. "Bypassing" tends to create trapped oil clusters, hence to reduce the residual oil saturation, in contrast to an efficient oil sweep from the inlet when water in the corners is absent (Figure 3.6(b)).

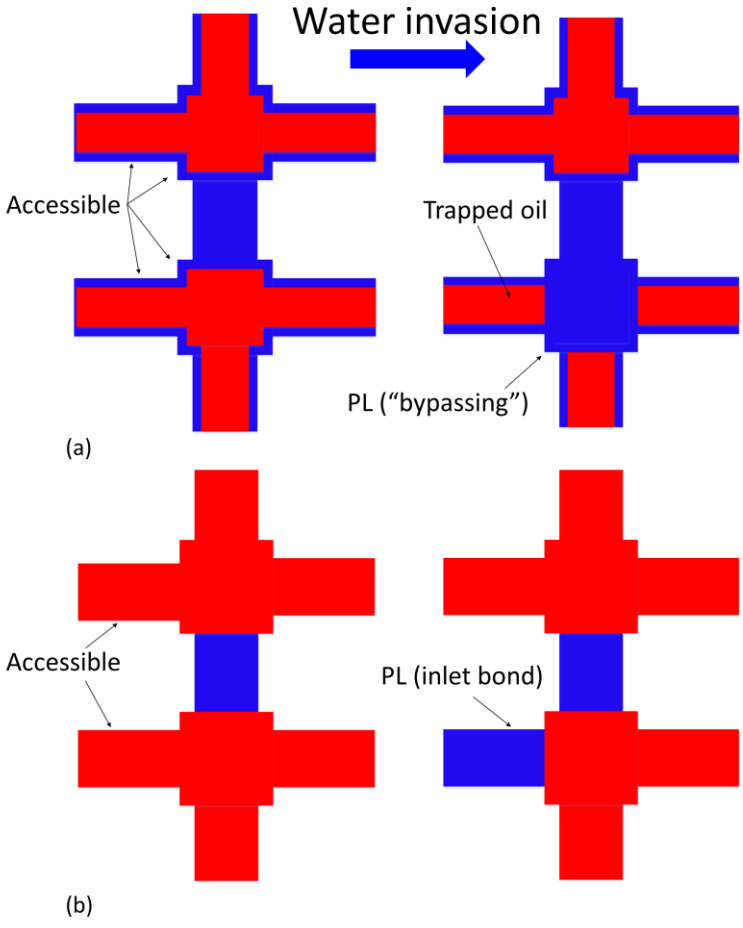

Figure 3.6: Illustration of different water invasion patterns, depending whether water in the corners is (a) present or (b) absent. In the first case, "bypassing" is likely to occur, which tends to create trapped oil clusters, as opposed to an efficient oil sweep from the inlet for the second case. Note that water (blue) displaces oil (red) from the inlet (left) to the outlet (right) of a 2D regular network.

b) Snap-off (SO)

Snap-off is an imbibition process that consists of the swelling of the water film until destabilisation of the oil/water interface and eventual water-invasion of the pore (Figure 3.5(b)). Unlike PL, SO requires a weak accessibility condition, since it may take place within a pore where water is only connected through films (rather than bulk) to the inlet. Nonetheless, SO is less favoured than PL in terms of entry pressures. Consequently, SO will only occur if there is no adjacent element whose centre is filled with water. Additionally, SO usually occurs under strongly water-wet conditions, is less likely to happen at weakly water-wet states, and is inhibited at intermediate and oil-wet conditions.

SO is considered to be the major mechanism for trapping of the non-wetting phase in the imbibition process since it tends to create disconnected non-wetting clusters all through the network. This leads to high levels of residual oil saturation.

c) Pore Body Filling (PBF)

Pore body filling (PBF), as illustrated in Figure 3.5(c)-(d), is an imbibition mechanism that corresponds to the displacement of the non-wetting oil phase from the centre of a node by the cooperative interfaces movement from the adjacent water-filled bonds.

If the node is directly connected to z bonds, $z-1$ possible entry pressures related to I_n ($n \in [1, z-1]$) events are computed beforehand, different from each other, using a bunch of parametric models available in the literature (Blunt, 1997, Blunt, 1998, Oren et al., 1998, Patzek, 2001, Valvatne and Blunt, 2004). Each PBF event I_n corresponds to a distinct possible configuration related to the number of connected oil-filled bonds n at the time of invasion. Notice that the displacement I_1 coincides with the PL displacement, and is the most favoured event (highest P_{entry}). Moreover, the I_n entry pressures should be positive, hence the PBF only occurs for spontaneous imbibition ($P_c \geq 0$).

Note that multiple PBF models have been previously implemented within the pore network model (Ryazanov, 2012). However, none of these models is rigorous, but rather based on arbitrary assumptions. In fact, they depend on random parameters and ad-hoc weighing coefficients. Hence, we decided to exclude the PBF events from this work.

d) Oil layers formation and collapse

During imbibition, oil layers may form in pores where parts of the surface are altered to strongly oil-wet; they are sandwiched between water in the centre and corners of the pores (Figure 3.7). While the contribution of these layers to oil volume and flow is small compared to that of bulk fluid, they play an important role in preserving the oil phase connectivity and driving it to very low saturations. However, they may get destabilised and collapse at a critical capillary pressure. In previous pore network (Blunt, 1998, Patzek, 2001, Valvatne and Blunt, 2004), the collapse of oil layers depends on a geometrical criterion as it takes place when the surrounding oil/water interfaces meet. In our simulator, the formation and collapse of the layers is more physically consistent, as it occurs according to a realistic thermodynamic criterion (van Dijke and Sorbie, 2006).

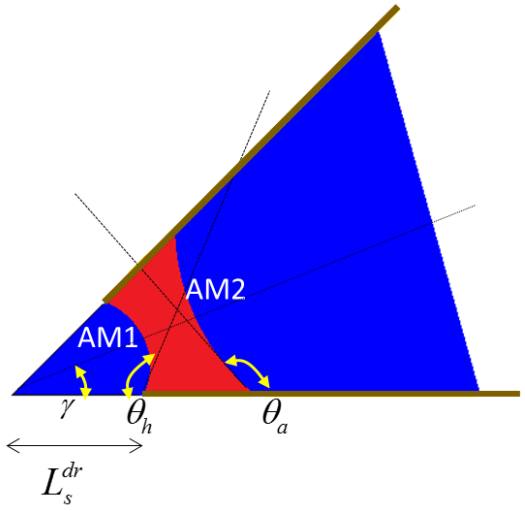

Figure 3.7: Illustration of the oil-layer configuration at the corner of a triangular cross-section, bounded by inner and outer arc menisci AM1 and AM2, with contact angles θ_h and θ_a, respectively. L_s^{dr} is the distance of AM1 from the corner edge. γ is the half-angle. Oil is red, water is blue and surfaces of altered wettability are brown.

3.2.4 Flooding cycle

We simulate the commonly used flooding cycle: primary drainage, ageing and water invasion, which mimics the flooding process undergone by a real hydrocarbon reservoir.

a) Primary Drainage (PD)

First, PD is simulated in a network where all pores are initially fully saturated with water and water-wet. In a first typical approach in Chapter 4, each pore is assigned a single

water-wet contact angle θ_{pd} that ranges between 0 and $90°$ and is chosen to be the same throughout the network. Alternatively, we developed in Chapter 5 a novel approach where each pore's contact angle evolves during primary drainage, depending on the concentration of polar compounds in the oil phase.

To establish the primary drainage pore-filling sequence, pore displacements entry pressures, P_{entry}, are explicitly computed for each pore prior to the PD simulation. The equations are detailed by Ryazanov (2012). Only one of two possible displacements is computed for each n-cornered pore, depending on its shape (γ) and wettability (θ_{pd}):

- If $\theta_{pd} < \frac{\pi}{2} - \gamma$, the pore is sufficiently water-wet to retain water in the corners, hence a PL displacement with formation of water corner films applies, called A-Dr (corresponds to the change in fluid configuration a->c in Figure 3.4).
- If $\theta_{pd} \geq \frac{\pi}{2} - \gamma$, a PL displacement with the complete removal of water from the pore, B-Dr, applies (a->b in Figure 3.4).

To decide the preliminary sequence of invasion events, the displacements for all the pores are then sorted in order of increasing P_{entry} .

During PD, while the inlet oil phase pressure, P_o , is increased in the inlet, the outlet water phase pressure, P_w is kept constant. This results in the gradual increase of the overall network capillary pressure, $P_c = P_o - P_w$. During this process, accessible and non-trapped bulk water-filled pores with the lowest P_{entry} (which turn below P_c) are invaded first by oil according to either A-Dr or B-Dr. Only 3 fluid configurations are possible for each pore (a, b and c in Figure 3.4). Note that as long as P_c is increasing, the corner water films with an outlet connection keep shrinking, as the length of contact of the water film with the solid in a corner, L_s, decreases in accordance with Equation (3.2). This results in a continuous decrease in the water saturation.

$$L_s = \frac{\sigma_{ow}}{P_c} * \frac{\cos(\theta_{pd} + \gamma)}{\sin \gamma} \qquad (3.2)$$

The process of oil invasion may be artificially stopped at a fixed initial water saturation, S_{wi}, related to a predefined maximum capillary pressure, ${P_c}^{max}$. We refer to it as S_{wi} at ${P_c}^{max}$. Alternatively, PD may continue until the irreducible water saturation is reached

where no further pore-scale displacements are possible under capillary controlled processes. We refer to it as S_{wi} at ${P_c}^{max} \rightarrow +\infty$. Note that in the latter case, ${P_c}^{max}$ is practically finite, corresponding to the highest entry pressure amongst the invaded pores. Additionally, notice that while the corner water films generated by displacement A-Dr maintain the water phase connectivity and may lead to water saturations close to zero, their absence following B-Dr displacement generates trapping of water clusters. Hence, the water structure at the end of PD consists of corner films and trapped bulk elements.

b) Wettability Alteration (ageing)

Subsequent to PD, the model allows for wettability alteration (ageing) of the oil-filled pores. This has consequences at two different scales i.e. intra-pore and inter-pore, as described in Figure 2.9, and further explained below.

Inter-pore scale

Ageing may result in a mixed-wettability state within the network. In fact, each pore is assigned either a water-wet advancing contact angle, $\theta_{a,ww} \epsilon [\theta_{pd}, 90°[$, or an oil-wet advancing contact angle, $\theta_{a,ow} \epsilon]90°, 180°]$. This allocation depends on two predefined parameters: the oil-wet fraction, f_{ow}, and the distribution type. The former is defined as the volumetric fraction of oil-wet pores among all the pores in the network, theoretically ranging between 0 and 1. For the latter, we choose from the commonly used wettability alteration distributions (Section 2.1.4), the pore-size related mixed-wet large (MWL) and mixed-wet small (MWS) distributions, or to the fractionally-wet (FW) size-independent distribution. Alternatively, we have implemented a physically based wettability alteration scenario that depends on both pore size and shape Chapter 4, leading to the Altered-Wet (AW) distribution.

Intra-pore scale

Ageing may result in a non-uniform wettability within a single oil-filled pore (Kovscek et al., 1993). Indeed, due to polar species adsorption from the oil, only the wettability of oil-contacted surfaces changes. These surfaces acquire an advancing (either water-wet or oil-wet) contact angle $\theta_a \geq \theta_{pd}$. Depending on the initial fluid configuration within the pore following PD, two transitions are possible: $b \rightarrow j$ or $c \rightarrow d$ (Figure 3.4). In the

latter case, different parts of the pore wall have different contact angles, with θ_a assigned to the central surfaces and θ_{pd} to the corners area.

c) Waterflooding

<u>Pore displacements</u>

Pore displacement entry pressures, P_{entry}, are computed for each pore before waterflooding, some explicitly and others iteratively, using equations described by Ryazanov (2012). Different displacement types exist for each n-cornered star-shaped pore, depending on its shape's corner half angle (γ, refer to Figure 3.2), wettability (θ_a and θ_{pd}) and accessibility.

- Initial configuration with corner water

If $\theta_{pd} < \frac{\pi}{2} - \gamma$, water films exist in the corners prior to waterflooding (configuration d in Figure 3.4). For this case, distinct PL displacements may be possible

  - If $\theta_a \geq \frac{\pi}{2} - \gamma$: two successive displacements are considered:
    - PL with the formation of oil layer, sandwiched between water in the corner and bulk, A-Imb ($e \rightarrow g$ in Figure 3.4).
    - Oil layers collapse, according to a thermodynamic criterion, C-Imb ($g \rightarrow f$ in Figure 3.4).

    Note that A-Imb and C-imb only exist together, and a condition for this is that $P_{entry}^{A-Imb} > P_{entry}^{C-Imb}$. The range of contact angles and capillary pressures for which layers exist has been thoroughly examined by Ryazanov (2012). If the condition is not satisfied, the displacement B-Imb below applies.

  - If $\theta_a < \frac{\pi}{2} - \gamma$ or $P_{entry}^{A-Imb} > P_{entry}^{C-Imb}$: PL with complete removal of oil applies, B-Imb ($e \rightarrow f$ in Figure 3.4).

Note that either of the PL displacements A-Imb (and C-Imb) or B-Imb are stored in the pore's list of possible displacements. Additionally, regardless of the value of θ_a, an extra snap-off displacement is computed for each pore and added to the list. Depending on the pore accessibility during waterflooding, either SO or PL will take place.

- Snap-off, D-Imb ($e \rightarrow f$ in Figure 3.4). As stated above (Section b)), $P_{entry}^{SO} < P_{entry}^{PL}$;

- Initial configuration without corner water

If $\theta_{pd} \geq \frac{\pi}{2} - \gamma$, the pore is initially fully saturated with oil (configuration *j* in Figure 3.4). Similar to PD (but with swapped phases), two displacements are possible, depending on γ and θ_a:

- If $\theta_a > \frac{\pi}{2} - \gamma$: the pore is sufficiently oil-wet to retain oil in the corners, thus a PL displacement with formation of oil corner films PL applies, called A1-Imb ($j \rightarrow k$ in Figure 3.4).
- If $\theta_a \leq \frac{\pi}{2} - \gamma$: a PL displacement that completely removes oil from the pore, B2-Imb, is computed ($j \rightarrow l$ in Figure 3.4).

Eventually, the preliminary invasion sequence prior to water invasion for all the pores is sorted in order of decreasing displacement entry pressures

Invasion process

At the start of waterflooding, the length of the contact of water with the solid in the corner is fixed at L_s^{dr}, computed from Equation (3.2) at $P_c = P_c^{max}$. Following ageing, the jump in contact angles ($\theta_{pd} \rightarrow \theta_a$) at L_s^{dr} leads to the pinning of the meniscus AM1 (Morrow, 1990, Kovscek et al., 1993) with a related "hinging" contact angle, θ_h, as illustrated in Figure 3.7. While the overall network P_c is decreased, θ_h increases from θ_{pd} to θ_a, corresponding to the change in fluid configuration $d \rightarrow e$ in Figure 3.4. As the waterflood carries on, accessible and non-trapped pores from the ordered displacements list whose P_{entry} are above P_c are invaded by water, in accordance to either A, A1, B, B1, C or D-Imb. Note that in the particular case of θ_a being low enough ($\theta_a < \frac{\pi}{2} - \gamma$), θ_h may overcome θ_a, then AM1 may start moving towards the surface with altered wettability at the centre of the pore ($d \rightarrow h$ in Figure 3.4). Particularly, if the AM1s meet at the centre (configuration i in Figure 3.4), they are destabilised and a particular case of snap-off occurs ($i \rightarrow f$ in Figure 3.4).

In our simulations, we assume that the process is carried on until the residual oil saturation, S_{or}, is reached, below which no further oil mobilisation can take place by capillary forces (S_{or} at $P_c^{min} \rightarrow -\infty$).

3.2.5 Network and phases connectivity

The Euler number χ is a topological invariant utilised as a measure of the connectivity of a fluid phase (either oil or water) within a network (Vogel, 2002, Herring et al., 2013). The fluid phase may consist of both bulk and film elements**.** The Euler number can be calculated as $\chi = \beta_0 - \beta_1$, where β_0 is the 0th Betti number, or the number of separate fluid phase elements in the network; and β_1 is the 1st Betti number, consisting of the number of redundant connections or loops in the fluid phase structure. β_1 can be regarded as the maximum number of cuts that can be applied to the fluid phase structure without breaking it into separate parts. Note that by definition, the more negative is χ, the more connected is the structure.

The Euler number of the network as a whole, considered as if fully saturated with only one phase, is simply computed as $\chi_{Net} = N_N - N_B$, where N_N is the number of nodes, including the "notional" boundary nodes, and N_B is the number of bonds. As for the Euler number of a particular phase of interest "ph", it is calculated as $\chi_{ph} = N_{N_{ph}} - N_{B_{ph}}$, where $N_{B_{ph}}$ is the number of bonds filled with phase "ph"; and $N_{N_{ph}}$ is the number of nodes, either "ph"-filled, or directly adjacent to a "ph"-filled bond (including the "notional" boundary nodes). Note that in the particular case where two "ph"-filled bonds share a node that is filled with the other phase, the node is counted twice. An example of Euler number calculations is performed in Figure 3.8.

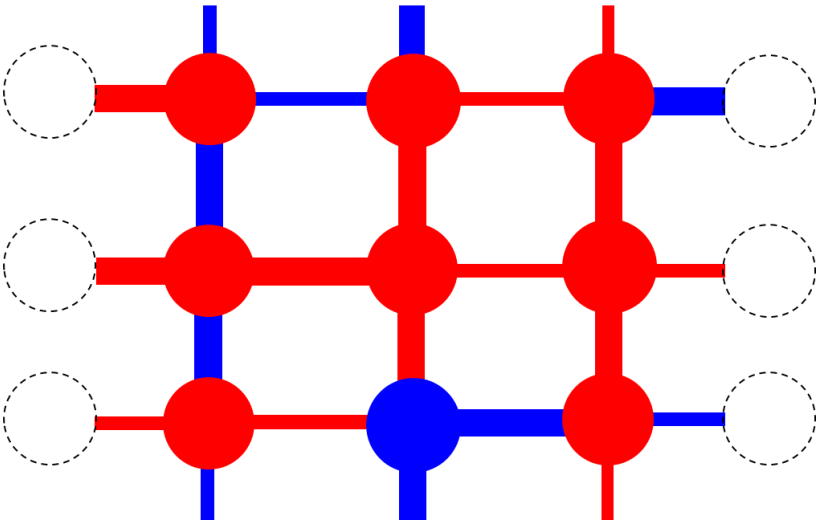

Figure 3.8: An example of Euler number calculations carried out on an illustrative 2D regular cubic network consisting of spherical nodes and tubular bonds. Periodic boundary conditions apply between the bottom and top. Oil (red) displaced water (blue) from the inlet (left) to the outlet (right); the "notional" boundary nodes are illustrated as dashed hollow circles. The network is a single object ($\beta_0 = 1$) with 7 redundant loops ($\beta_1 = 7$). Further, $N_N = 15$ (9 actual + 6 boundary nodes) and $N_B = 21$; hence $\chi_{Net} = \beta_0 - \beta_1 = N_N - N_B = -6$. Similarly, for the oil phase, $(\beta_{0_{oil}}, \beta_{1_{oil}}) = (3, 2)$ and $(N_{N_{oil}}, N_{B_{oil}}) = (14, 13)$, hence $\chi_{oil} = 1$.

The Euler number is used in Section 3.3 below to derive the connectivity function of a given network, which describes its connectivity as a function of the pores size (Vogel, 2002). Besides, in the next chapters, we use the normalized Euler number $\hat{\chi}$ as a measure of the connectivity of a fluid phase within the network (Herring et al., 2013). For a given phase (either oil or water), $\widehat{\chi_{ph}} = \frac{\chi_{ph}}{\chi_{Net}}$ is the ratio of the Euler number of the selected phase over the network's Euler number. By definition, $\widehat{\chi_{ph}} = 1$ corresponds to maximum phase connectivity, while $\widehat{\chi_{ph}} \leq 0$ corresponds to a disconnected phase ($\chi_{ph} \geq 0$) within a connected network ($\chi_{Net} < 0$).

3.3 Input networks

In this thesis, two input networks with different topologies will be used: a homogeneous Berea sandstone network with a relatively narrow range of pore sizes, and a heterogeneous two-scale carbonate network with a wide range of pore sizes, where the smallest pores provide overall connectivity to the otherwise disconnected network.

3.3.1 Berea sandstone network

The network (Figure 3.9(a)) has been extracted from a 3D micro-computed tomography image of a Berea sandstone sample, using the enhanced extraction technique described by Jiang et al. (2007). Its characteristics are summarized in Table 3.1. Figure 3.9(b) shows that the pore size distribution is unimodal, and that larger pores tend to have more corners.

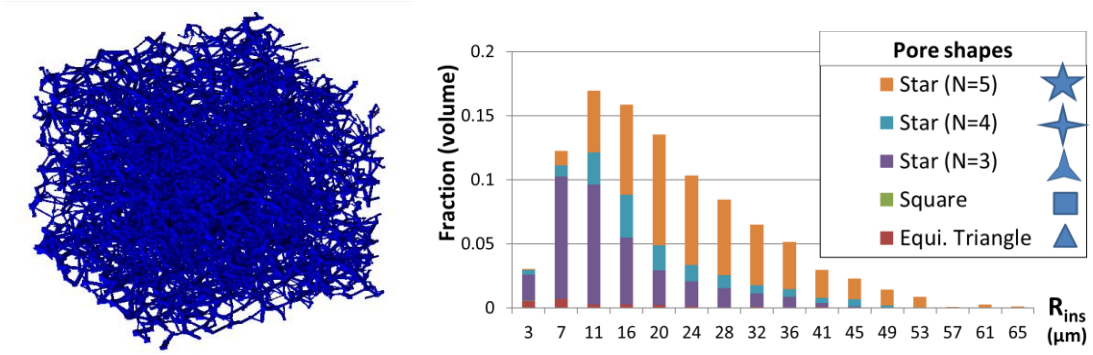

(a) *(b)*

Figure 3.9: Berea network: (a) 3D representation and (b) pore size (inscribed radius) and shape distributions.

Number of pore elements (nodes and bonds)	*22,251*
Average coordination number	*3.7*
Porosity (%):	*18.97*
Absolute Permeability (mD):	*1576.38*

Table 3.1: Main properties of the Berea network.

3.3.2 Multiscale carbonate network

We present here a heterogeneous network (Figure 3.10) constructed from a multiscale dataset for a microporous carbonate, and whose characteristics are summarised in Table 3.2. The methodology and workflow of the two-scale network generation have been presented by Jiang et al. (2013) and summarised in Section 2.2.4. Note that the coarse scale network clearly lacks overall connectivity (Figure 3.10(b)), and has only become connected through integration with the well-connected fine scale network (Figure 3.10(a)).

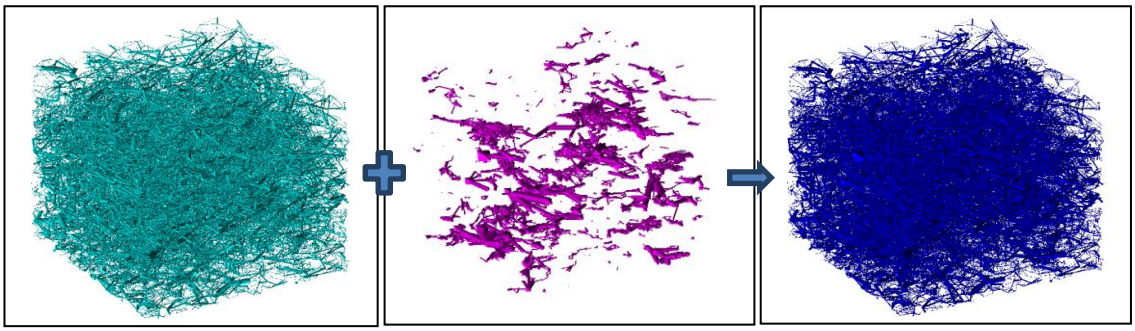

(a) (b) (c)

Figure 3.10: (a) Statistically generated fine network extracted from a micro-CT image at $2.86\ \mu m$ *resolution, (b) coarse network extracted from another micro-CT image at* $14.29\ \mu m$ *resolution and (c) the resulting integrated two-scale network. Note that both images are derived from the same microporous carbonate dataset.*

Number of pore elements	*26,349*
Average coordination number	*3.5*
Porosity (%):	*21*
Absolute Permeability (mD):	*59*

Table 3.2: Main properties of the carbonate network.

Figure 3.11 indicates a wide distribution of pore radii in the resulting two-scale network, ranging from 1 to 146 µm, and that micropores ($R_{ins} < 5\mu m$) represent around 15 % of the network volume (corresponding to the first bin in the pore size distribution). Additionally, note that the micropores are represented by a wide range of cross-sectional shapes.

The connectivity functions of the carbonate and Berea networks are compared in Figure 3.12. Each one is obtained by removing pores from the network in order of increasing size and re-computing χ_{Net} at each step. Suppressing larger and larger pores leads to a decrease in connectivity i.e. increase in χ_{Net} from negative values. The radius at which the network (just) gets disconnected i.e. $\chi_{Net} = 0$, may correspond to the network's percolation radius. Figure 3.12 shows that the carbonate network's percolation radius of around $5\ \mu m$ is much smaller than the Berea's value of $13\ \mu m$. This further confirms that the carbonate network connectivity is mainly controlled by its micropores.

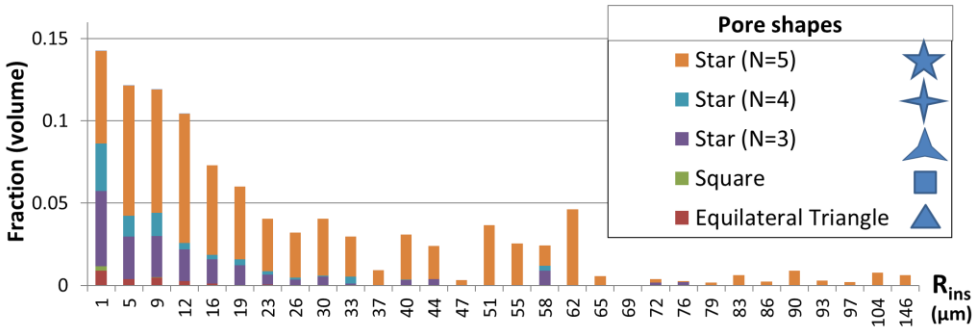

Figure 3.11: Carbonate network pore size (inscribed radius) and shape distributions.

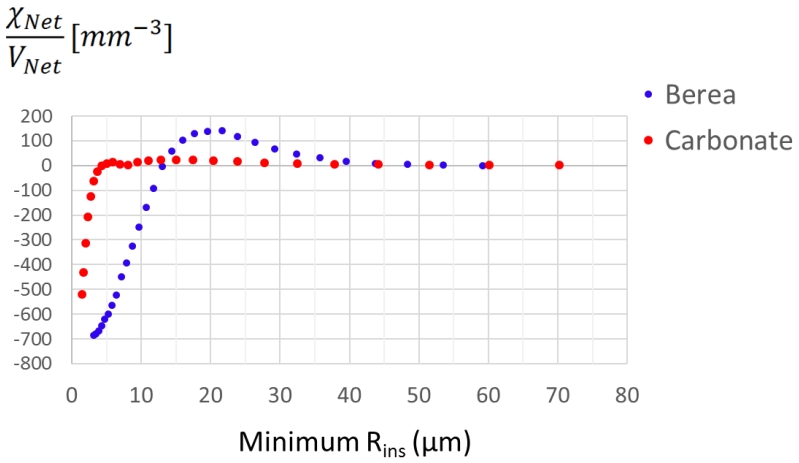

Figure 3.12: Comparison between the connectivity functions of the carbonate and Berea networks, where χ_{Net}/V_{Net} is the Euler number of the network divided by its total volume.

3.4 Conclusion

In this chapter, we described the pore network multi-phase model that we use throughout this work. The model has two main specifics compared to other pore network models available from the literature:

- Involves a wider variety of cross-sectional pore shapes, mainly the N-star shapes, as compared to standard CTS (Circle-Triangle-Square) shapes. This leads to a broad range of possible fluid configurations and the corresponding pore-scale displacements;
- Incorporates a physically-based thermodynamic criterion for oil layer formation and collapse, instead of the previously used geometrical criterion.

Note that the model described in this chapter was created by Ryazanov (2012), except for the new connectivity calculations using the Euler number. In the following chapters,

we describe the two novel models that we have incorporated in the original pore network model as part of this thesis:

- Scenario 1: Wettability alteration *following* primary drainage and subsequent to ageing (Chapter 4). This scenario is faithful to the traditional flooding cycle described in Section 3.2.4. We incorporated into it a physically-based wettability distribution, based on Kovscek et al. (1993)'s model, that takes into account both the pore size and shape.
- Scenario 2: Wettability alteration starting *during* primary drainage (Chapter 5). In this scenario, we modify the way primary drainage is modelled. Indeed, based on the work by Bennett et al. (2004), we model a wettability alteration that occurs as the primary drainage occurs, as a result of the adsorption of polar species from the oil. This wettability evolution changes the primary drainage patterns.

Chapter 4 : Scenario 1 – Wettability alteration following ageing

4.1 Introduction

In this chapter, we implemented the Kovscek et al. (1993)'s model in our pore network model that takes into account a variety of pore shapes, representative of the complexity of real carbonate rocks. In Section 4.2, we present the model where equivalent pore wall curvatures are assigned to pores based on their size and shape. Moreover, the disjoining pressure is inferred from the fraction of oil-wet pores and the maximum achieved capillary pressure. In Section 4.3 we investigate the role of the wettability distribution in oil recovery for pore space structures of different complexities, starting with the relatively simple Berea sandstone network, which is then compared with the complex multiscale carbonate network. For the carbonate case, we further examine the importance of the wettability state of the micropores for oil recovery.

4.2 Model description

We model the physically-based wettability alteration scenario suggested by Kovscek et al. (1993)**,** thoroughly described in Section 2.1.1, for which the wettability is controlled by the stability of the thin films through the disjoining pressure. All pores are initially assumed to be filled with water and completely water-wet, and at this point we start injecting oil. At the end of the primary drainage, a maximum capillary pressure, P_c^{max}, is reached, either predefined, or corresponding to the highest entry pressure amongst the oil-invaded pores. For each of the pores invaded, if the oil phase is still connected to the outlet i.e. not-trapped, the local capillary pressure reached coincides with the network's P_c^{max}. Otherwise, it corresponds to the capillary pressure at which trapping occurred. Besides, the local threshold capillary pressure, P_c^*, is computed for each invaded pore using Equation (2.2). If P_c^* was overcome by the local maximum capillary pressure, we assume that the thin film had collapsed and the pore is rendered oil-wet following ageing. Otherwise, the pore remains water-wet.

However, in our pore network model, pore walls are represented by flat surfaces with zero curvature (regular polygon and star shapes), hence thin films would collapse simultaneously in all pores, as all P_c^* are equal for constant Π_{crit} (Equation (2.2)). As it is difficult to obtain the real pore wall curvatures from a digitised image, we assign equivalent curvatures to the flat pore walls based on the overall pore shapes, for

wettability alteration purposes only, as indicated in Figure 4.1. The curvature, $c = -\frac{1}{r_c}$, is assumed negative as the radius of curvature, r_c, is located outside the shapes. For regular polygons, r_c is computed using Equation (4.1) (Joekar-Niasar et al., 2010) in which $\cos\varphi$ is randomly chosen. For regular stars, r_c is computed from Equation (4.2). Note that while one random parameter ($\cos\varphi$) is introduced for polygons, the radius of curvature is fully determined for stars.

$$r_c^{n-polygon} = R_{ins}\frac{\sin\frac{\pi}{n}}{\cos\varphi - \sin\frac{\pi}{n}} \qquad (4.1)$$

$$r_c^{n-star} = R'_{ins}\frac{\sin\frac{\pi}{n}}{\cos\gamma - \sin\frac{\pi}{n}} = R_{ins}\frac{\sin\left(\gamma+\frac{\pi}{n}\right)\sin\frac{\pi}{n}}{\sin\left(\gamma+\frac{\pi}{n}\right).\cos\gamma - \sin\frac{\pi}{n}} \qquad (4.2)$$

where R_{ins} and R'_{ins} denote the original and new inscribed radii, respectively; $cos\varphi$ ranges between $sin\frac{\pi}{n}$ and 1; and γ is the corner half-angle of the pore.

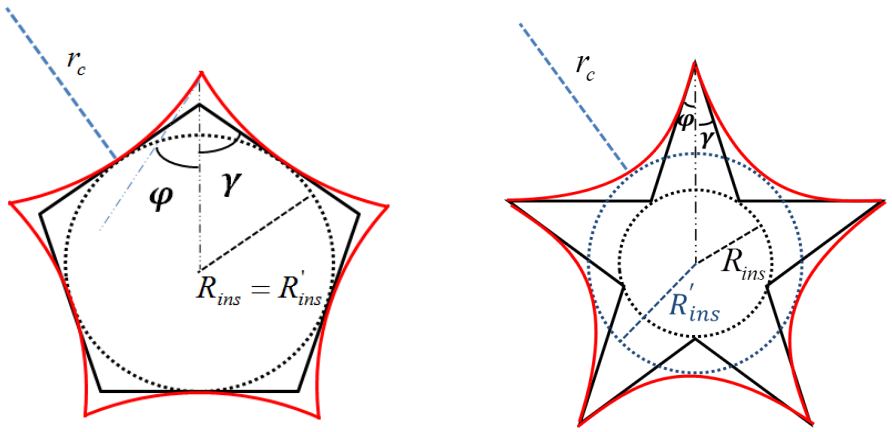

(a) *(b)*

Figure 4.1: Equivalent pore wall curvature assignment for (a) n-cornered Polygon and (b) n-cornered Star shape, where R_{ins} and R'_{ins} denote the original and new inscribed radii, respectively; r_c denotes the radius of curvature and φ the angle between the tangent to the newly obtained (red) curved shape at a vertex and the line connecting the vertex to the centre (φ coincides with the corner half-angle, γ, for the original shapes).

According to Equation (2.2), by strictly using the negatively-curved star shapes introduced in Figure 4.1, the more curved the pore surface is (in absolute value), the

more accessible (lower) is the capillary pressure at which the thin film collapses (P_c^*). Therefore, smaller pores of the same shape are more likely to be oil-wet. This is also the case for pores of the same size and shape but with a larger number of corners, which can be interpreted as corresponding to increased pore roughness. Therefore, the model qualitatively reproduces the pattern shown by high-resolution imaging in carbonate rocks (Marathe et al., 2012) where oil deposition on calcite microparticles was limited to the anhedral (curved, rough and poorly formed) faces.

Π_{crit} depends on the fluid system and mineralogy of the rock surface. We will assume in our model that it is constant throughout the network, reflecting a mono-mineral rock. Π_{crit} is computed by the simulator, given a prescribed final drainage capillary pressure, ${P_c}^{max}$, and a targeted volumetric oil-wet fraction, f_{ow}, the ratio of the oil-wet to the total pore volumes. Note that a higher ${P_c}^{max}$ leads to a higher f_{ow}, as thinner films are more prone to collapse. On the other hand, higher Π_{crit} causes f_{ow} to decrease, since a higher P_c would need to be achieved to reach film rupture (at P_c^*).

Throughout the thesis, we refer to the resulting wettability distribution as Altered-Wet (AW). Below (Sections 4.3.1(b) and 4.3.2(b)) we describe how this new AW distribution compares to previously described wettability distributions MWL, MWS and FW.

Note that since no comprehensive model is available for the distribution of the values of the advancing contact angle θ_a, these are assumed to be uniformly distributed within prescribed ranges in both the water-wet and oil-wet pores.

4.3 Results and discussion

The simulations are carried out on the two distinctly different networks presented in Section 3.3: a homogeneous sandstone network and a heterogeneous network derived from a microporous carbonate dataset. The same base case is chosen for both networks (Table 4.1). At ageing, we uniformly distribute the water-wet and oil-wet advancing contact angles as $\theta_{a,ww}\epsilon[\theta_{pd}, 90°[$ and $\theta_{a,ow}\epsilon[120°, 180°]$, respectively. Note that the value of $\theta_{pd} = 30^0$ corresponds to an initially water-wet rock.

S_{wi}	*0*
θ_{pd}	*30°*
f_{ow}	*0.5*
Wettability distribution	*AW*

Table 4.1: Base case parameters for Scenario 1 simulations.

4.3.1 Berea sandstone network

a) Primary drainage

In the base case, the primary drainage (PD) process is continued until the irreducible water saturation is reached at $P_c{}^{max} = 22kPa$ (Figure 4.2). As shown in Figure 4.3, all invaded pores are sufficiently water-wet ($\theta_{pd} < \frac{\pi}{2} - \gamma$) to hold water in the corners, which forms the irreducible water saturation $S_{wi} < 0.01$. In a second case, oil invasion is stopped at prescribed initial water saturation $S_{wi} = 0.3$ ($P_c{}^{max} = 5kPa$). As expected, water is mainly left behind in the smallest pores, for which the P_{entry} are highest.

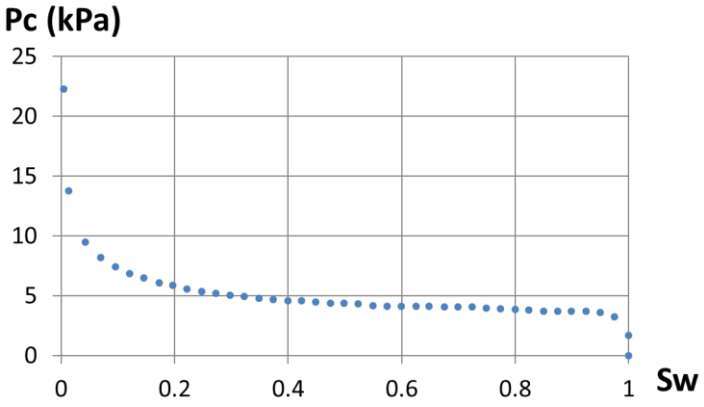

Figure 4.2: Primary drainage P_c curve for the Berea network.

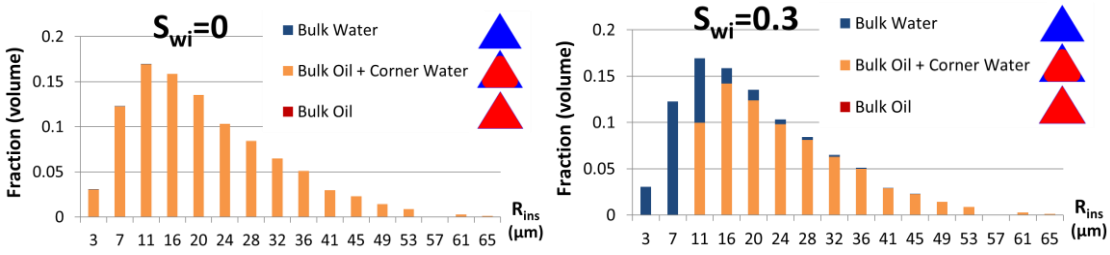

Figure 4.3: Pore occupancies for the Berea network shown on the pore size distribution following PD to different S_{wi} values.

b) Ageing

The different wettability distributions (MWL, MWS, FW and AW) at $\mathrm{f_{ow}} = 0.5$ resulting after PD are plotted in Figure 4.4 on the volumetric pore size distributions. In the MWL (resp. MWS) distribution, oil-wet pores are evidently the largest (respectively smallest). The FW distribution results in half the pores being oil-wet for each bin size. On the other hand, AW exhibits a more complex distribution, where both pore size and shape determine the wettability distribution. For instance, the size of the largest pores ($\mathrm{R_{ins}} \geq$

41μm) prevents them from having sufficient curvature for the water film to break, thus leaving them water-wet. Moreover, few small pores are found to be oil-wet. Indeed, the smallest pores are mostly characterised by 3-cornered star shapes (Figure 3.9), and as previously stated (Section 4.2), pores with smaller number of corners (reduced roughness) are less likely to be oil-wet.

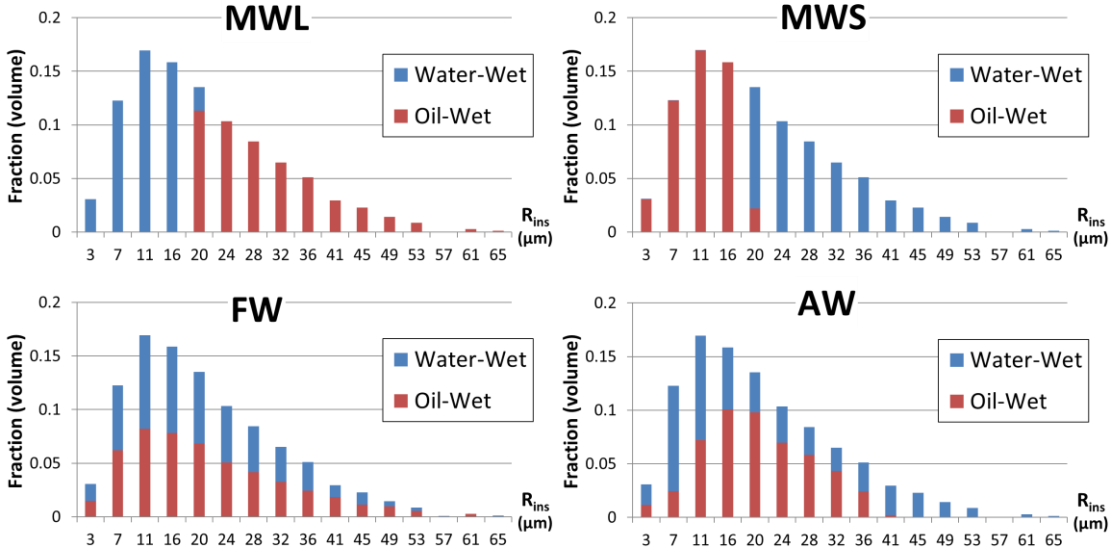

Figure 4.4: Different wettability distributions shown on the pore size distributions for the Berea network at $f_{ow} = 0.5$, established after PD for the base case; red: oil-wet, blue: water-wet. Darker blue (respectively red) indicates stronger water- (respectively oil) -wetness.

c) Waterflood

<u>Effect of wettability distribution</u>

The effect of varying the wettability distribution on the residual oil saturation, S_{or}, was found to be small (Figure 4.5(a)). This behaviour could be explained by the homogeneity of the sandstone structure, where pores are connected to one another regardless of size. We will show below that the effect of the wettability distributions on S_{or} is much more profound for the heterogeneous carbonate network (Section 4.3.2(c), Figure 4.15), whose topology is much more complex. On the other hand, from the pore occupancies at $f_{ow} = 0.5$ (Figure 4.6) it is clear that the residual oil distribution (unlike the residual oil saturation) is affected by the wettability distribution. In all cases, we find that the residual oil is mostly present in oil-wet pores, as expected. A few oil layers formed near the end of the waterflood process, mainly in the largest oil-wet pores, whose layers

formation P_{entry} are highest. The effect of the presence of oil layers on S_{or} is shown for the AW distribution in Figure 4.5(b). The "with layers" case corresponds to the base case where oil layers formation is enabled. On the contrary, the oil layers formation was disabled in the "no layers" case. As expected, oil layers allow oil to drain to lower S_{or} when f_{ow} is sufficiently large (for this network $f_{ow} \geq 0.5$) for a spanning (percolating) oil-wet pathway to be formed.

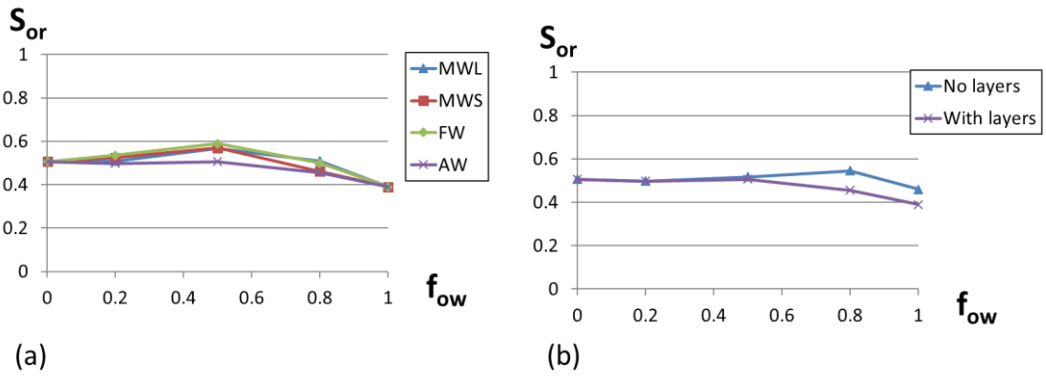

Figure 4.5: Waterflood residual oil saturations as a function of oil-wet fractions for the Berea network (a) for the different wettability distributions, and (b) for the AW distribution, with and without oil layers.

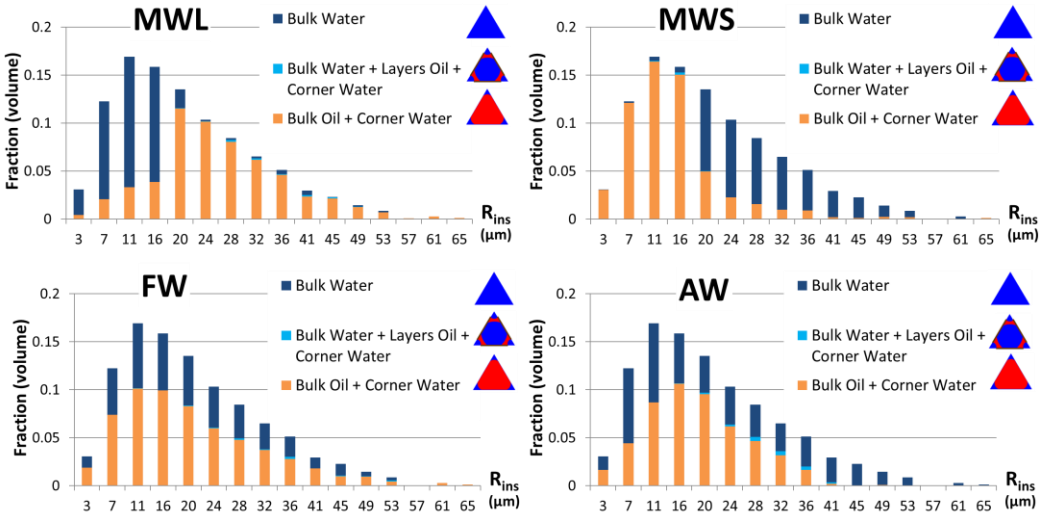

Figure 4.6: Pore occupancies at the end of the waterflood for the different wettability distributions shown on the pore size distribution for the Berea network at $f_{ow} = 0.5$.

Effect of initial water saturation

A sensitivity study to S_{wi} was conducted for the AW distribution. Note that because f_{ow} is defined as a fraction of all pores, the maximum value that it can take is $1 - S_{wi}$, since the remaining fraction S_{wi} is water-filled and water-wet. This explains the different curve endpoints for the different S_{wi} in Figure 4.7.

Figure 4.7(a) shows that at $f_{ow} = 0.5$, with S_{wi} increasing from 0 to 0.1, i.e. strongly decreasing P_c^{max} (see Figure 4.2), S_{or} slightly increases. This is mainly due to the fact that the oil layer formation is inhibited at relatively low P_c^{max}. The trend is amplified for higher $f_{ow} = 0.8$, for which the oil layers are more abundant, thus more effective in maintaining the oil connectivity. Further increasing S_{wi} leads to monotonically decreasing S_{or}, as the oil saturation before waterflood, $1 - S_{wi}$, decreases. Nevertheless, the effect of S_{wi} on the S_{or} curves is considered to be small compared to the heterogeneous carbonate case (Figure 4.16).

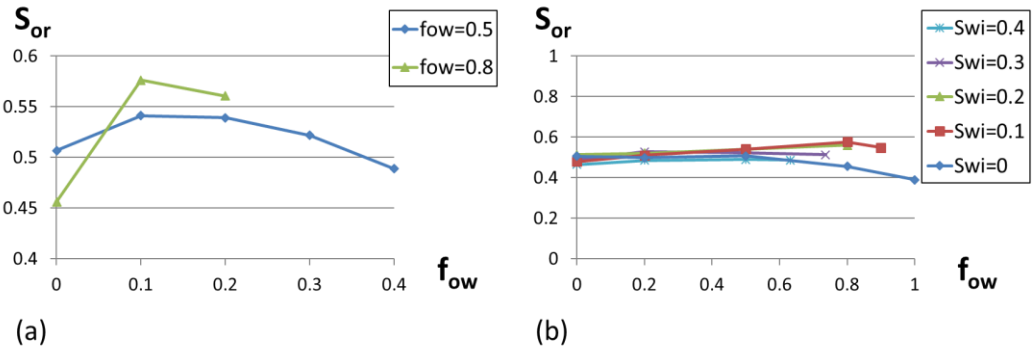

Figure 4.7: Waterflood residual oil saturations for the AW distribution in the Berea network as a function of (a) S_{wi} and (b) f_{ow}.

4.3.2 Carbonate network

a) Primary drainage

As for the Berea network, the primary drainage (PD) process is continued until the irreducible water saturation, approximately $S_{wi} = 0$, is reached at a relatively high $P_c^{max} = 48kPa$ (Figure 4.8), due to the small size of the micropores. At $S_{wi} = 0.3$, remaining water resides mainly in the micropores, since their P_{entry} are highest (Figure 4.9). Moreover, as for the Berea network (Figure 4.3), a small fraction of larger not-yet-accessible pores still retain water.

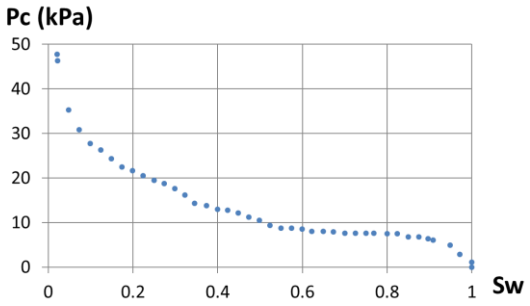

Figure 4.8: Primary drainage P_c curve for the carbonate network.

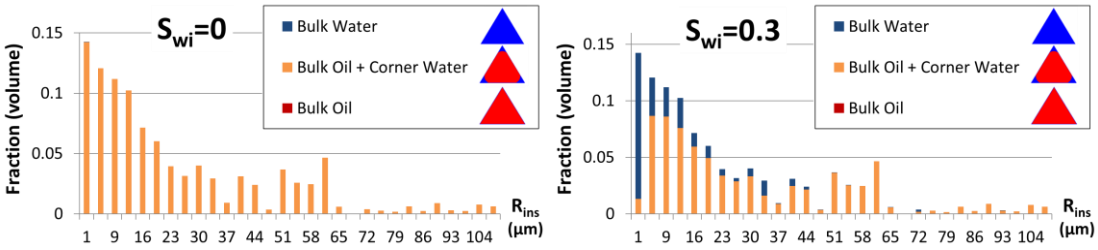

Figure 4.9: Pore occupancies for the carbonate network shown on the pore size distribution following PD to different S_{wi} values.

b) Ageing

Following ageing, the resulting wettability distributions within the carbonate network are shown in Figure 4.10. When comparing them with those for the Berea network in Figure 4.4, it can be seen that the MWL, MWS and FW distributions are (by definition) qualitatively quite similar. The AW distributions are similar as well, but only for the largest pores, as that remain water-wet. However, the striking difference for AW occurs in the smallest pores. Indeed, for the carbonate network, unlike for the Berea, 85% of the micropores are oil-wet, since their small sizes provide sufficient curvature for the water films to break for most of their shapes.

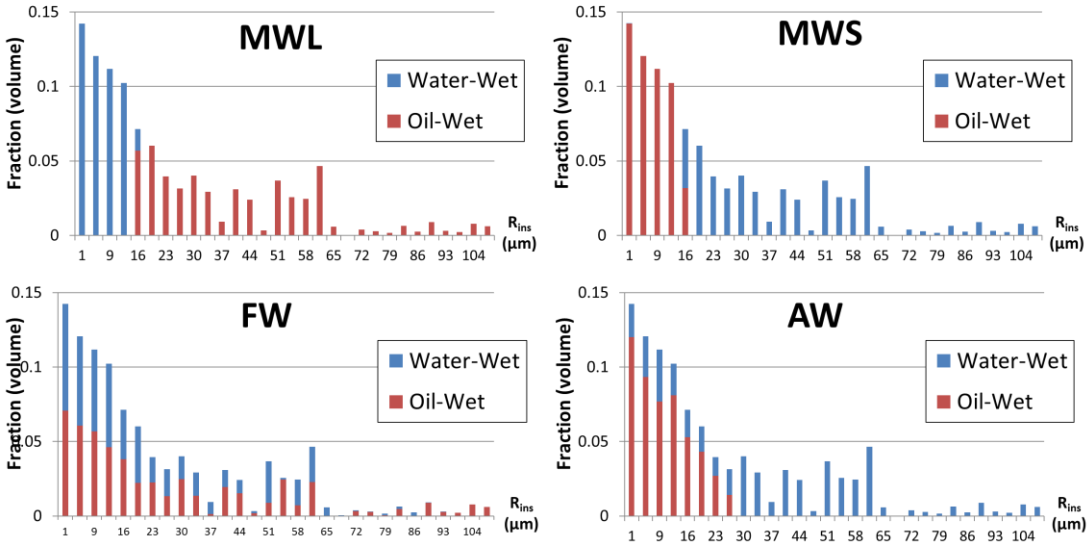

Figure 4.10: Different wettability distributions shown on the pore size distributions for the carbonate network at $f_{ow} = 0.5$, established after PD for the base case; red: oil-wet, blue: water-wet.

c) Waterflood

<u>Effect of wettability distribution</u>

The wettability distribution significantly affects the petrophysical properties for the carbonate network (Figure 4.11). Indeed, the residual oil varies greatly, as S_{or} decreases from 0.7 for MWL to 0.24 for MWS. In addition, P_c curves are found to be dissimilar as a result of the different pore-filling sequences. With regard to relative permeabilities, K_r, they are highly sensitive to the fluid saturations; hence we are not drawing any specific conclusions except that they are at some extent affected by the wettability distribution (Figure 4.11(c)). Since the relative permeabilities of water, K_{rw}, are too low to be actually seen, we derived the fractional flow of water, F_w, from the K_r curves, computed assuming identical phase viscosities as:

$$F_w = \frac{1}{1 + \frac{K_{ro}}{K_{rw}}} \qquad (4.3)$$

F_w appears in the Buckley-Leveret equation when modelling water flooding at the continuum-scale and it shows here that water breakthrough ($K_{rw} > 0$) occurs at very different water saturations for the different wettability distributions (Figure 4.11(d)).

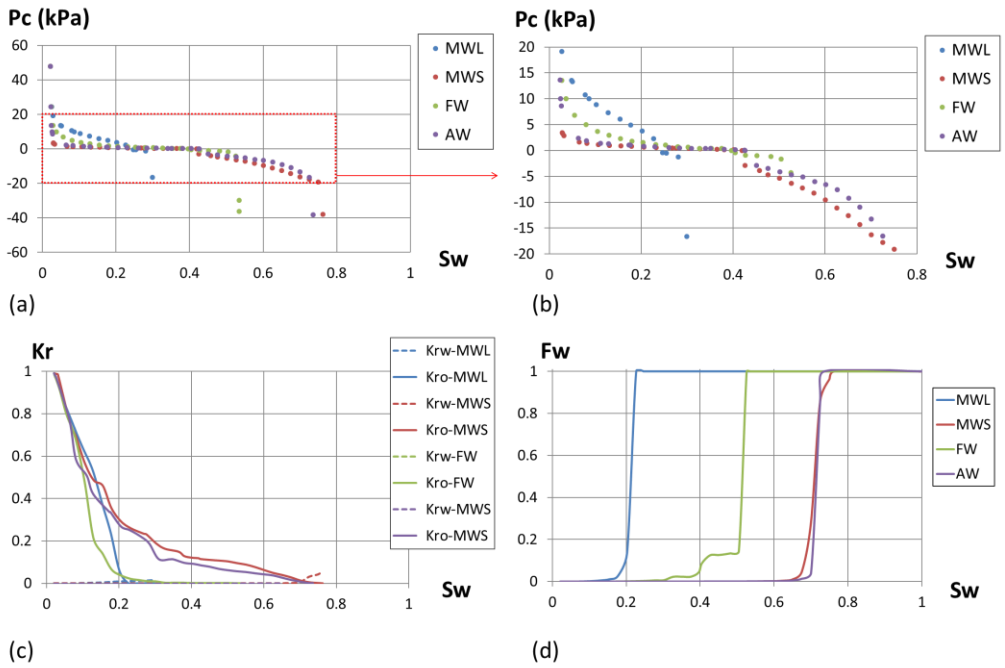

Figure 4.11: (a) P_c curves, (b) enlarged P_c curves (red box), (c) K_r curves and (d) fractional flow of water, F_w, curves after waterflood for the different wettability distributions at $f_{ow} = 0.5$ for the carbonate network.

The pore occupancies at the end of the waterflood are presented in Figure 4.12 for all four wettability distributions. Note that, in general, water would start filling water-wet pores (from small to large), then oil-wet pores (from large to small), unless this is prevented by lack of accessibility and trapping. Since the fine scale pores provide the overall connectivity for the disconnected coarse scale pores (Section 3.3.2), two interesting limiting cases stand out, MWL and MWS.

In the MWL distribution, a fraction of the fine scale pores are water-wet, thus first filled with water. However, these water-filled pores now block the escape of oil from the coarse scale pores, thus leaving much oil trapped in the largest pores, as well as in intermediate-sized pores and some micropores. The capillary pressure curve for this case (see Figure 4.11(a) and (b)), confirms that almost exclusively small, i.e. water-wet, pores are invaded. Hence, trapping in the MWL case is high compared to the other distributions.

Conversely, in the MWS case, water first starts filling the larger water-wet pores. Note that all pores have corner wetting films (see Figure 4.8). Therefore, all pores are accessible to the invading water, even though the coarse scale network is disconnected.

Water invasion then continues in the smaller oil-wet pores as a drainage process. The corresponding jump in invaded pore size is translated into a large drop in P_c over a small saturation range in the capillary pressure curve (Figure 4.11(b)). By leaving the micropores to be filled at the end of the process, MWS has the lowest trapping of all wettability distributions.

The pore occupancy for the AW distribution (Figure 4.12) is quite similar to that for MWS, in contrast to the occupancies for the Berea network, while the occupancy for FW exhibits behaviour intermediate to MWS and MWL.

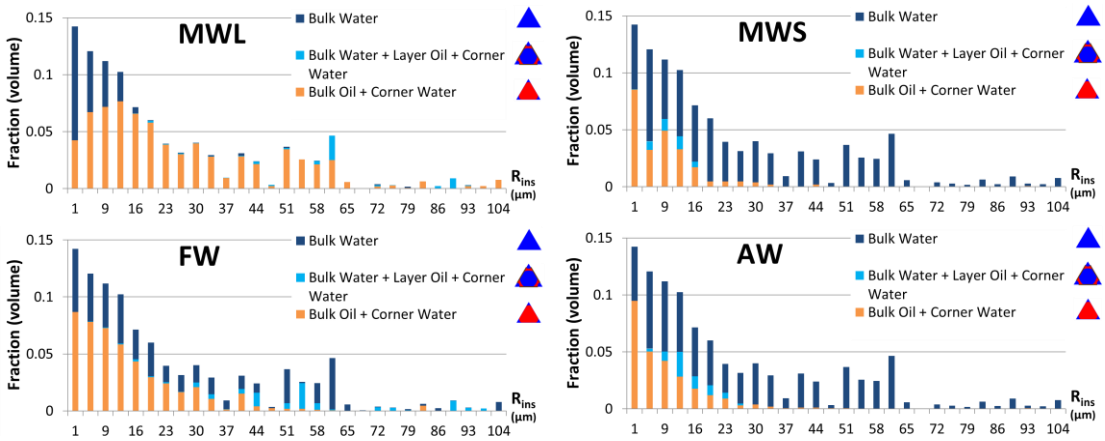

Figure 4.12: Pore occupancies at the end of the waterflood for the different wettability distributions shown on the pore size distribution for the carbonate network at $f_{ow} = 0.5$.

The oil phase connectivity, translated into $\widehat{\chi_{oil}}$, is shown in Figure 4.13 as a function of the water saturation during waterflood for the different wettability distributions. It confirms that the residual oil saturation is controlled by the rate of trapping of the oil phase during water injection. In fact, MWL, FW, AW and MWS systems exhibited slower decrease in $\widehat{\chi_{oil}}$, in order, which resulted in decreasing residual oil saturations, in order.

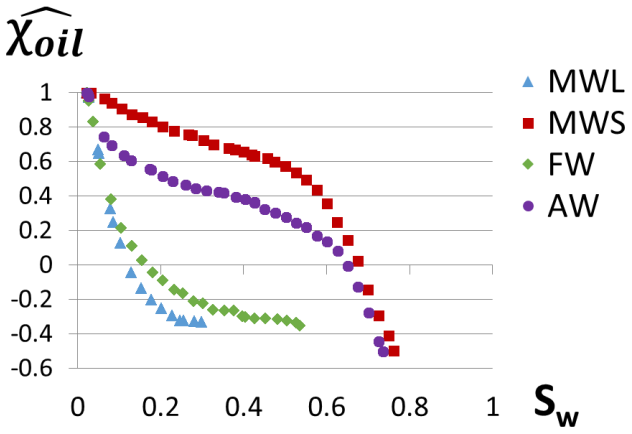

Figure 4.13: Evolution of the oil phase connectivity (normalised Euler number) during waterflood for the different wettability distributions at $f_{ow} = 0.5$ in the carbonate network.

Effect of oil-wet fraction

We now consider the AW distribution, and study the impact of changing the fraction of oil-wet pores, f_{ow}, on the petrophysical properties. As expected, P_c curves are lower for larger fractions of oil-wet pores (Figure 4.14). Considering the residual oil saturation, the trend is visibly monotonic, as S_{or} decreases with f_{ow}. We note as well that the switch from fully water-wet ($f_{ow} = 0$) to less water-wet ($f_{ow} = 0.2$) leads to a large reduction in S_{or}, as a fraction of the micropores become oil-wet. However, further changing to fully oil-wet has a relatively small effect. The impact of the presence of oil layers on S_{or} shown in Figure 4.15(b) is similar to that seen in the Berea network (Figure 4.5(b)).

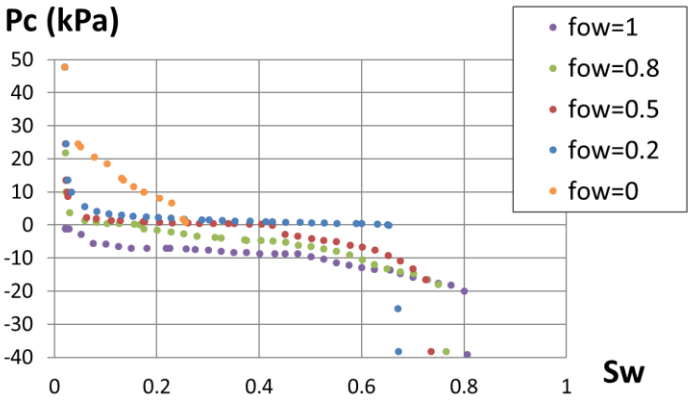

Figure 4.14: P_c curves after waterflood for different oil-wet fractions for the carbonate network.

The results of this sensitivity study are summarised in Figure 4.15(a), where both the wettability distribution and f_{ow} are varied. Unlike for the Berea sandstone (see Figure 4.5(a)), the S_{or} values are very different for the various wettability distributions in this microporous carbonate. The MWS and MWL distributions clearly form the limiting boundaries for the residual oil saturations. Indeed, the best recovery is exhibited by MWS, while MWL shows the worst recovery. On the other hand, recoveries for the developed AW distribution and the FW distribution lie between the two extreme cases, but they still differ significantly from each other.

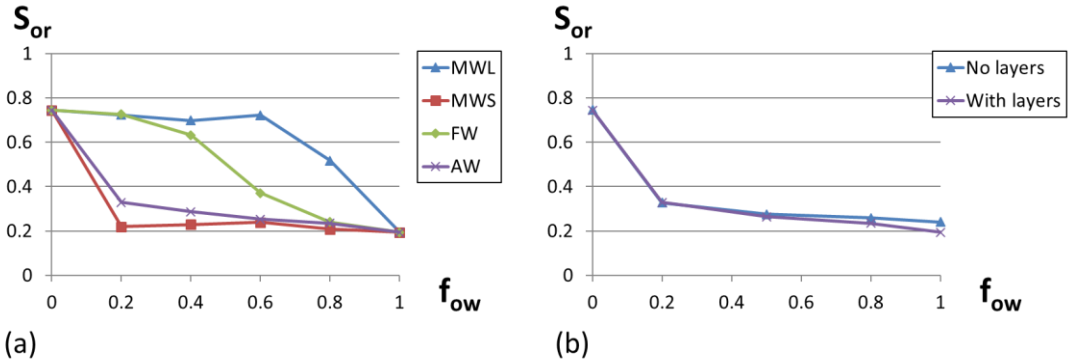

Figure 4.15: Waterflood residual oil saturations as a function of oil-wet fractions for the carbonate network (a) for the different wettability distributions, and (b) for the AW distribution, with and without oil layers.

Effect of initial water saturation

S_{or} curves are plotted in Figure 4.16 for different S_{wi} values for the AW distribution. The trends are similar to those observed in the Berea network (Figure 4.7) but the variations and the differences between the curves for varying f_{ow} are much larger. Actually, while increasing S_{wi}, added to the fact that fewer oil layers form, more water is retained in the micropores at the start of the waterflood, which in turn blocks the escape of oil in the bigger pores due to the particular connectivity of the carbonate network.

To examine the structure of the residual oil, we show in Figure 4.17 the pore occupancies at the end of the water flood for different S_{wi} values at $f_{ow} = 0.5$. Since the initial water resides mostly in the micropores (see Figure 4.9), the nature of the residual oil changes with higher S_{wi}, as oil is increasingly trapped in intermediate-sized pores and less so in

micropores. Besides, as previously stated, oil layers are less likely to develop at lower P_c^{max}, i.e. at higher S_{wi}.

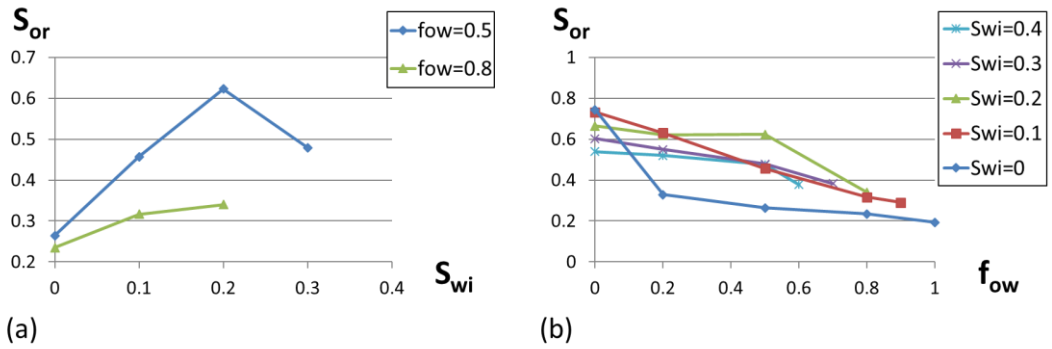

Figure 4.16: Waterflood residual oil saturation for the AW distribution in the carbonate network as a function of (a) S_{wi} and (b) f_{ow}.

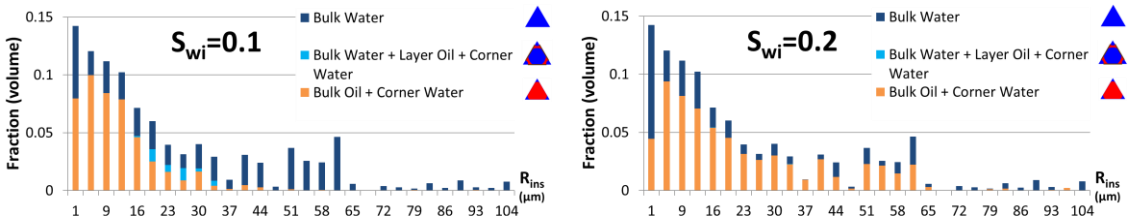

Figure 4.17: Pore occupancies at the end of the waterflood for different S_{wi} values shown on the pore size distribution for the carbonate network at $f_{ow} = 0.5$.

Note that by keeping f_{ow} constant (equal to 0.5) and increasing S_{wi} (decreasing P_c^{max}) (Figure 4.16), the corresponding Π_{crit} value is decreasing. This may not be realistic since Π_{crit} is assumed to be an intrinsic property of the rock mineral and water film sub-system. Indeed, the "right" way would be to keep Π_{crit} constant, increase S_{wi}, and consequently obtain a lower f_{ow} (see Figure 4.18, moving along vertical lines). For instance, if $\Pi_{crit} = 48.33kPa$ was chosen such that $f_{ow} = 0.5$ for $S_{\mathrm{wi}} = 0$ ($\mathrm{P_c}^{\max} = 47.8kPa$), changing S_{wi} to 0.1 would reduce P_c^{max} to 27.8kPa. The latter value would be below the critical capillary pressure P_c^* of all pores, keeping all water films intact, thus $f_{ow} = 0$.

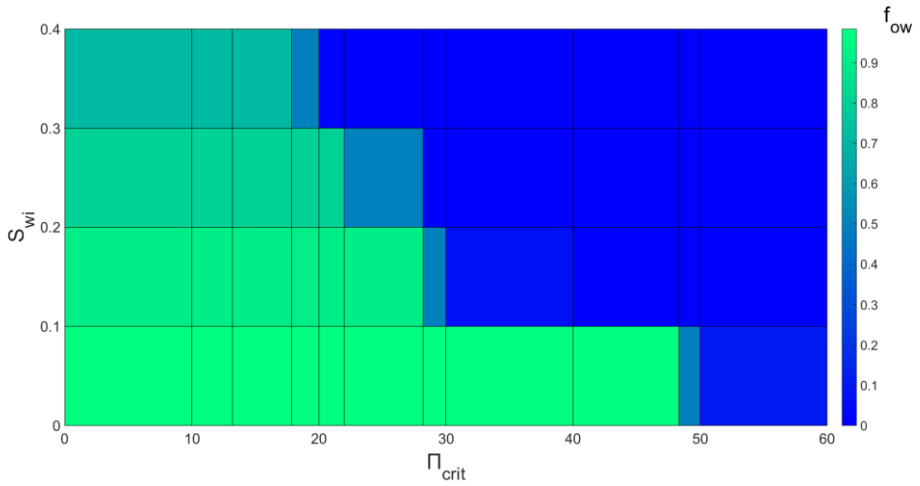

Figure 4.18: Contour chart describing the relationship between Π_{crit}, S_{wi} and f_{ow}.

4.4 Discussion

First, note that since we are lacking real S_{wi} (or $P_c{}^{\max}$) data, zero initial water saturation, $S_{wi} = 0$, was chosen as a base case to highlight the impact that the wettability of micropores has on recovery. In fact, oil presence in micropores has been reported in many real carbonate rocks, especially towards the top of the oil column. This could happen if the reservoir has a sufficiently large oil column such that a high capillary pressure is reached in the upper oil column, or if some pores have somehow undergone a change in size (e.g. by means of dissolution/cementation) or in wettability (e.g. due to polar species in the oil) over geological time.

Wettability has long played the role of a sort of "tuning parameter" in simulations, although in actual calculations it is the consequent petrophysical function (P_c and K_{ro}) that is actually used or varied; no "number for wettability" appears in any oil displacement calculation. However, there is strong evidence from pore network modelling (supported again by the results presented here) that the actual assumptions on the wetting distribution do strongly influence these petrophysical functions as well as the S_{or} value. Thus, if we had some prior knowledge of these wetting patterns, then we might be able to forward model the petrophysical functions. Working petrophysicists and core analysts in the oil industry do have views on the physical forms of these wetting patterns. Therefore, we suggest building up "Type diagrams" of wetting patterns in carbonate rocks by consideration of the possible mechanisms involved, such as those incorporated in the developed AW model. The patterns generated can then be presented to petrophysics experts who will recognise the most

likely physically realistic patterns. This approach is used in other industries and is known as expert elicitation (Curtis and Wood, 2005). At best such a scenario might generate in a systematic manner prior probabilities of certain wetting patterns for realistic carbonates. We believe that this is the only way that a combination of flow physics, forward modelling and industry expertise/knowledge can be combined to make some advances in modelling complex mixed-wet systems at the pore level.

4.5 Conclusions

We developed a physically-based wettability alteration scenario, dependent on both pore size and shape, which incorporates a plausible view of the wetting change mechanism. The scenario qualitatively reproduced a pattern of wettability observed in microporous carbonates through high-resolution imaging, where anhedral (curved, rough and poorly formed) faces become preferentially oil-wet. We implemented the scenario in a two-phase quasi-static pore network model which involves a variety of pore shapes. We considered as input two pore networks with very different levels of complexity in their pore structure, (a) a fairly homogeneous connected Berea sandstone network with a relatively narrow range of pore sizes, and (b) a heterogeneous two-scale carbonate network whose coarse scale pores were not connected, but where the fine scale pores provided overall connectivity to the network. We considered the widest possible range of wettability distributions including the newly developed Altered-Wet (AW) distribution, along with the commonly used MWL, MWS and FW distributions. This resulted in a correspondingly wide range of outcomes in terms of pore occupancies, P_c and K_r curves and S_{or} values.

After ageing was carried out, the AW distribution resulted in the largest pores being water-wet, as their large size prevented them from having sufficient curvature for the water film to collapse. Conversely, owing to their tiny size, most of the carbonate network's micropores were found to be oil-wet, provided that they were invaded by oil during primary drainage. Yet, the AW distribution was still distinct from the MWS, as well as from any of the other common wettability distributions. Following waterflooding, we showed from the pore occupancies that the specific wettability distribution affects the structure of the residual oil. In addition, wettability proved to have some effect on the residual oil saturation (S_{or}) for the Berea network, but it had a much larger impact for the multiscale carbonate network. Indeed, since the connectivity

of this network is mainly driven by pore size, the MWS and MWL distributions formed limiting cases for the S_{or} values, with the recoveries for the AW and FW distributions lying between these two extremes. The MWL case exhibited by far the lowest oil recovery since the first-filled water-wet micropores blocked the escape of oil from the larger pores. Conversely, the MWS distribution showed the best recovery as the oil-wet micropores are left to be filled with water at the end of the waterflood. In addition, the relative permeability curves for the carbonate network were very sensitive to the chosen wettability distribution. This was emphasised by the corresponding fractional flow curves, which showed very different water breakthrough saturations. Furthermore, we demonstrated that oil layers did indeed allow oil to drain to lower S_{or}, but only at a sufficiently high f_{ow}. Moreover, by increasing S_{wi}, we first observed higher S_{or}, due to fewer oil layers being formed, and then lower S_{or} because of a decreasing oil saturation before waterflood. We proved that these trends are amplified at higher f_{ow} values where more oil layers form, as well as in the carbonate network where the effect of the network's particular connectivity contributes notably. Indeed, the increased volumes of connate water left behind in the micropores consequently trap the oil in the larger pores.

Chapter 5 : Scenario 2 – Wettability alteration starting during primary drainage

5.1 Introduction

In the previous chapter, we examined a physically-based wettability alteration model, referred to as Altered-Wet (AW), and assessed the consequences of wettability distributions in pore network models. Indeed, we described in a simple manner the rule-based wetting change mechanism that strictly occurs *following* primary drainage, due to the surface adsorption of such species as asphaltenes subsequent to ageing in crude oil. This corresponds to the traditional approach that mimics the 3-stage process experienced by an initially water-wet reservoir: primary drainage, ageing and waterflood. Interestingly, we demonstrated the importance of the wettability of micropores on oil recovery, but only if they are actually invaded by oil. Although this may seem unlikely due to the very high capillary pressures needed to invade such tiny pores, oil has actually been detected within micropores in carbonates (Al-Yousef et al., 1995, Clerke, 2009, Knackstedt et al., 2011, Fung et al., 2011, Clerke et al., 2014, Dodd et al., 2014) which may be explained by a wettability change that occurred progressively over geological time.

In this chapter, we present a more mechanistic physically-plausible model for the initial stages of wetting change from water-wet to more intermediate-wet conditions, which may occur *during* primary drainage. We implement the model in the quasi-static pore network model described in Section 3.2, to explain and numerically simulate the wettability alteration mechanism suggested by Bennett et al. (2004), described in Section 2.1.1, involving smaller polar compounds from the oil. We have added a "scaled" time-dependency to the common oil invasion-percolation algorithm to be able to incorporate a time-dependent transport model for polar compounds. The time scaling referred to incorporates the balance between the oil invasion/migration timescale and the timescale of diffusion of small polar species and their adsorption which triggers a wetting change. The physical and chemical processes in this model will affect the final phase distributions and initial water saturations in the oil column after oil migration. Particularly, the model provides a clear and precise mechanism of how oil can migrate into micropores, without necessarily reaching the excessively high capillary pressures

that would be required for oil invasion into strongly water-wet micropores. Subsequently, we model the full "ageing" change associated with asphaltenes and the resulting oil-wet conditions. In Section 5.2, details are given of how small polar non-hydrocarbon molecules diffuse from the oil into and through the water phase within the pore network, thus leading to wettability alteration which can progress as the primary drainage process occurs. In Section 5.3, we present the resulting fluid distributions at the pore level (pore occupancies) and the consequences of these changes on the phase saturation profiles within the oil column during primary drainage, and their effect on subsequent imbibition. These calculations are based on the two networks with distinct pore-structures introduced in Section 3.3: the homogeneous Berea network and the heterogeneous multi-scale carbonate network.

5.2 Model Description

The model starts with initially water-filled and perfectly water-wet pores, the initial oil/water contact angle, $\theta = 0°$. Commonly in quasi-static pore network modelling simulators (Chapter 4), oil invasion occurs pore by pore at discrete invasion percolation (IP) events. These are assumed to happen instantaneously, hence time is not explicitly taken into consideration. In this chapter, we separate these invasion events in time, based on an assumed flow rate Q, corresponding to a charge time for an oil reservoir by oil migration.

In fact, we assume that the invading volumes of oil, $V_{oil}[m^3]$ linearly increase over time: $\mathrm{V}_{oil}(t) = Q * t$, where t[s] is the migration time; $Q[m^3 s^{-1}]$ is the flow of hydrocarbons invading a reservoir rock. Q is chosen low enough to remain in the capillary-dominated regime by satisfying Equation (3.1) using $q = Q/A_{inlet}$, with A_{inlet} the total cross-sectional area at the system inlet. We effectively replace a discrete process done in steps by a continuous process described by the straight line in Figure 5.1. Note that the individual volumes of the invaded pores are expected to decrease in time during primary drainage, since oil generally fills the water-wet pores from large to small in size.

At time t_i during instantaneous oil invasion of pore i, we consider the polar compounds to be transported through the oil phase. The details of this process are provided in Section 5.2.1. Additionally, during the period of time $t_{i+1} - t_i$ separating two successive pore invasion events, a diffusion/adsorption model for polar compounds is applied using constant discrete time steps, Δ_t^{TR} (Figure 5.1). In fact, we assume that the polar

compounds diffuse to - and adsorb in - the oil-filled pores, as well as in the water-filled pores due to their high solubility in water (Bennett et al., 2004), as detailed in Section 5.2.2. The initial conditions for the diffusion/adsorption process are related to the oil/water configuration and their relative concentrations at time t_i.

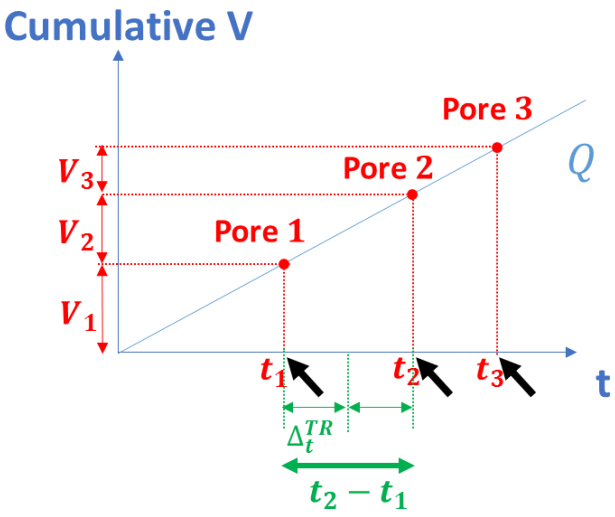

Figure 5.1: Illustration of the separation in time of the oil invasion events, where the cumulative volume of pores invaded linearly increases over time based on the assumed flow rate, Q; and the incorporation of a diffusion/adsorption model for polar compounds using discrete time steps, Δ_t^{TR} , during the period of time $t_{i+1} - t_i$ separating two successive pore invasion events.

Note that some particular cases may arise as a consequence of the assumptions that we have made:

- The period $t_{i+1} - t_i$ is known based on the next anticipated invasion. Hence, if a spontaneous invasion, usually of a smaller pore, takes place as a result of contact angle changes, t_{i+1} will be smaller and the period $t_{i+1} - t_i$ will be shorter. Therefore, we may already have diffused for too long.
- When the predefined maximum capillary pressure, P_c^{max}, is reached and no more invasions are anticipated, the diffusion/adsorption model is carried out and Δ_t^{TR} incremented until a spontaneous invasion becomes available due to contact angle change.
- The period $t_{i+1} - t_i$ is generally not a multiple of Δ_t^{TR}. Thus, we assume that the diffusion/adsorption model stops before the next invasion at time t_{i+1} is exceeded when incrementing Δ_t^{TR}.

- In the particular case of a very high flow rate where $t_{i+1} - t_i < \Delta_t^{TR}$, the two successive pore invasions at t_i and t_{i+1} occur and the diffusion step is delayed until the above condition does no longer hold or until the predefined P_c^{max} is reached and no more invasions are anticipated.

5.2.1 Transport through oil invasion

Throughout this section, we will consider a single pore i and define $C_{i_o}(\mathrm{t})\ [^{mg}/_{L}]$ and $C_{i_w}(\mathrm{t})\ [^{mg}/_{L}]$ as the mobile concentrations of polar compounds in the oil phase and water phase, respectively, and $\Gamma_{\mathrm{i}}(\mathrm{t})\ [^{mg}/_{m^2}]$ as the corresponding adsorption level of polar compounds per unit area in pore i at time t. Note that we assume perfect mixing within each phase.

If pore i is water-wet and has corners, water remains in the pore corners, as well as in a thin film lining the pore wall following oil invasion (Kovscek et al., 1993)**.** When polar compounds are transported into the oil-phase of pore i, either through oil invasion or through diffusion, we assume that they instantaneously partition between the oil and water phases within the same pore, since they are highly soluble in water, and that they instantly adsorb onto the surface from the water-phase. These are reasonable assumptions given the timescales of diffusion compared to the slower migration of oil. An illustration of the partitioning and adsorption within an angular oil-filled pore is shown in Figure 5.2. We also assume that the concentration of polar compounds in the water-phase, $C_{i_w}(t)$, is linearly related to the oil-phase concentration, $C_{i_o}(t)$, as follows:

$$C_{i_w}(t) = PC_{i_o}(t)\ , \forall t > 0 \qquad (5.1)$$

where P is the partitioning coefficient, input to the model ($0 < P < 1$).

During oil invasion of pore i at time t_i, as illustrated in Figure 5.2, we consider the polar compounds to be carried by the oil phase. Hence, we assume that $C_{i_o}(t_i)$ is equal to the concentration at the oil invasion front, computed as an average of the oil phase concentrations in the connecting oil-filled pores:

$$C_{i_o}(t_i) = \frac{\sum_{k=1}^{z_o} C_{k_o}(t_i)\, V_{k_o}}{\sum_{k=1}^{z_o} V_{k_o}} \qquad (5.2)$$

We define V_{k_o} and V_{k_w} as the volumes of the oil phase and water phase of pore k, respectively, satisfying $V_{k_o} + V_{k_w} = V_k$. Besides, z_o is the number of oil-filled pores adjacent to pore i, $z_o \leq z$, where z is the total number of pores connected to pore i; z is equal to 2 for a bond, corresponding to its two connecting nodes ($z = 1$ for a boundary bond) and $z \geq 1$ for a node, corresponding to its coordination number (number of neighbouring bonds).

The oil invasion of pore i at time t_i results in a gain in the mass of polar compounds in the oil-phase in the network, equal to $C_{i_o}(t_i) * V_{i_o}$. In order to satisfy the mass balance of polar compounds, we assume that this extra mass is supplied at the inlet. Besides, if prior to invasion, pore i had a non-zero concentration of polar compounds, $C_{i_w}(t_i^-)$, we assume that this concentration is unchanged immediately after oil invasion, i.e. $C_{i_w}(t_i) = C_{i_w}(t_i^-)$, resulting in a loss of some mass of polar compounds from the water phase due to the decrease in its volume, equal to $C_{i_w}(t_i) * V_{i_o}$. This mass is assumed to be expelled through the outlet. The total mass within the pore at time t_i, $m_{\mathrm{i}}(t_i)$, is equal to $C_{i_o}(t_i) * V_{i_o} + C_{i_w}(t_i) * V_{i_w} + \Gamma_i(t_i) * SA_i$, where SA_i $[m^2]$ is the total surface area of pore i. Afterwards, at t_i^+, this mass is supposed to instantaneously distribute between the phases within the same pore and to adsorb onto the surface in accordance with a Langmuir isotherm as follows:

$$\Gamma_i(t_i^+) = \Gamma_{max} \frac{K C_{i_w}(t_i^+)}{1 + K C_{i_w}(t + \Delta_t^{TR})} \qquad (5.3)$$

$$m_{\mathrm{i}}(t_i^+) = C_{i_o}(t_i^+) * V_{i_o} + C_{i_w}(t_i^+) * V_{i_w} + \Gamma_i(t_i^+) * SA_i = m_{\mathrm{i}}(t_i)$$

where Γ_{max} $[{}^{mg}/_{m^2}]$ and K $[{}^{L}/_{mg}]$ are the Langmuir maximum adsorption level per unit area and adsorption constant, respectively.

By combining Equations (5.1) and (5.3), we obtain a single quadratic equation that we solve for $C_{i_o}(t_i^+)$, knowing $C_{i_o}(t_i)$, $C_{i_w}(t_i)$, and $\Gamma(t_i)$:

$$KP.C_{i_o}(t_i^+)^2 + \left(1 + \frac{KP}{V_{i_o} + PV_{i_w}}(\Gamma_{max}.SA_i - m_{\mathrm{i}}(t_i))\right).C_{i_o}(t_i^+) - \frac{m_{\mathrm{i}}(t_i)}{V_{i_o} + PV_{i_w}} = 0 \qquad (5.4)$$

Afterwards, $C_{i_w}(t_i{}^+)$ and $\Gamma_i(t_i{}^+)$ are directly derived from equations (5.1) and (5.3), respectively.

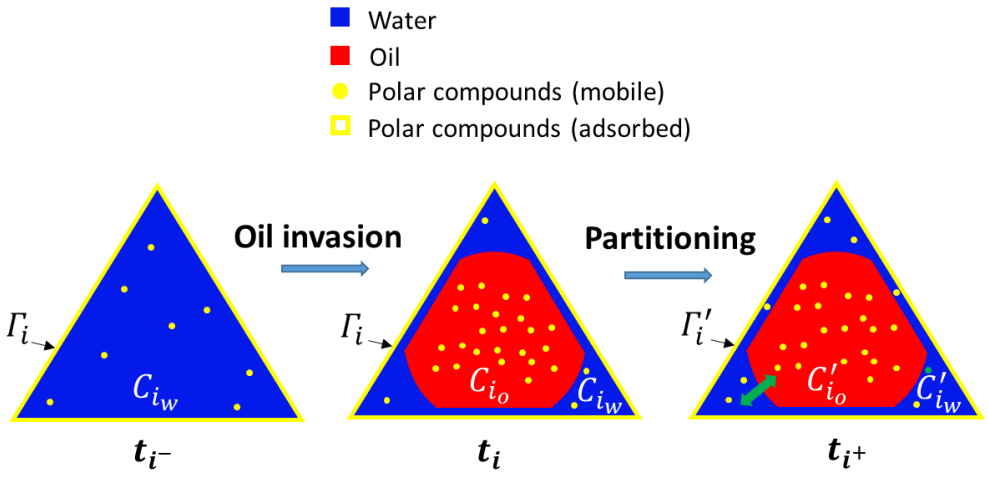

Figure 5.2: Illustration of the transport of polar compounds within a pore i with triangular cross-section during oil invasion (at time t_i); as well as their distribution between the phases within the same pore and their adsorption onto the surface, which are assumed to happen right after invasion (at time $t_i{}^+$). Note that C_{i_o} and C_{i_w} are the mobile concentrations of polar compounds in the oil phase and water phase, respectively, and Γ_i is the corresponding adsorption level of polar compounds per unit area.

5.2.2 Transport through diffusion

As previously stated, polar compounds diffuse into both oil-filled and water-filled pores during the period of time separating two successive pore invasions at discrete time-steps Δ_t^{TR} .

a) Mass balance equations

Oil-filled pores

The material balance of the polar compounds within pore i is described by the one-dimensional diffusion-adsorption equation in the following discretized from:

$$\frac{\Delta C_{i_o}}{\Delta_t^{TR}} = \frac{C_{i_o}(t+\Delta_t^{TR}) - C_{i_o}(t)}{\Delta_t^{TR}} = \frac{1}{V_{i_o}\Delta_t^{TR}}\left(\Delta m_{d_i} - \Delta m_{ex_i}\right)$$
$$\frac{\Delta C_{i_w}}{\Delta_t^{TR}} = \frac{C_{i_w}(t+\Delta_t^{TR}) - C_{i_w}(t)}{\Delta_t^{TR}} = \frac{1}{V_{i_w}\Delta_t^{TR}}\left(\Delta m_{ex_i} - \Delta m_{a_i}\right) \qquad (5.5)$$

where Δm_{d_i}, Δm_{ex_i} and Δm_{a_i} $[mg]$ are the masses of polar compounds that diffused into the bulk phase (here oil), that exchanged between the oil and the water phases and that adsorbed onto the surface, respectively, in pore i during time increment $\Delta_t^{TR}[s]$; Additionally, we assume that the diffusion occurs only through the bulk phase, neglecting any mass exchanged with the neighbouring pores through the corner water phase. Since Δm_{ex_i} is the same mass exchanged between oil and water, the two Equations in (5.5) lead to a single equation:

$$V_{i_o}\left(C_{i_o}(t+\Delta_t^{TR}) - C_{i_o}(t)\right) + V_{i_w}\left(C_{i_w}(t+\Delta_t^{TR}) - C_{i_w}(t)\right) = \Delta m_{d_i} - \Delta m_{a_i} \quad (5.6)$$

<u>Water-filled pores</u>

Additionally, due to their supposedly high water solubility, polar compounds are assumed to diffuse into the water-filled pores where they also adsorb onto the surface. Since the pore only contains a water phase, the material balance for the polar compounds is simply provided by the following equation:

$$\frac{\Delta C_{i_w}}{\Delta_t^{TR}} = \frac{C_{i_w}(t+\Delta_t^{TR}) - C_{i_w}(t)}{\Delta_t^{TR}} = \frac{1}{V_i \Delta_t^{TR}}(\Delta m_{d_i} - \Delta m_{a_i}) \quad (5.7)$$

b) Diffusion model

We apply a discretized form of Fick's diffusion equations for the diffusion of polar compounds within pore i (Equation (5.8)), with the diffusion front only advancing to the directly adjacent pores ahead at each time-step Δ_t^{TR}.

$$\Delta m_{d_i} = \Delta_t^{TR} \sum_{k=1}^{z} J_{ki}.\min(A_i, A_k)$$
$$J_{ji} = -D\frac{C_i(t) - C_j(t)}{L_{ji}} \quad (5.8)$$

where z is the number of pores connected to pore i (as defined above); J_{ji} $[{}^{mg}/_{m^2 s}]$ is the diffusion flux from pore j to pore i, which occurs across the minimum bulk phase cross-sectional area, A $[m^2]$, between the two adjacent pores; L_{ji} $[m]$ is the distance between the centre of pore j and centre of pore i; D $[{}^{cm^2}/_{s}]$ is the diffusion coefficient; Note that at fixed "realistic" diffusion constant D, we should carefully choose a low Δ_t^{TR}

in order to avoid instabilities that arise from the discretised diffusion model. Indeed, unless every pore satisfies the condition below, mass conservation fails:

$$\Delta m_{d_i} + m_{i_{bulk}}(t) \geq 0 \qquad (5.9)$$

where $bulk$ corresponds to the pore's bulk phase, through which the diffusion occurs; and $m_{i_{bulk}}(t)$ is the mass at the beginning of the time-step in the bulk phase, defined as $m_{i_{bulk}}(t) = C_{i_{bulk}}(t)V_{i_{bulk}}$.

As for the boundary conditions, the concentration at the inlet is taken as constant over time, equal to C_0. At the outlet, a "no flow" boundary condition is assumed. The boundary conditions are translated into the following equations:

$$\begin{aligned} C_{i_o}(t) &= C_0\,, \forall t > 0,\ \forall i \text{ "notional" inlet node} \\ C_{j_o}(t) &= C_{(j-1)_o}(t)\,, \forall t > 0,\ \forall j \text{ "notional" outlet node} \end{aligned} \qquad (5.10)$$

where $(j-1)$ is the outlet bond connected to the "notional" outlet node j. The "notional" boundary nodes are illustrated in Figure 3.8.

We model the diffusion between two pores sharing the same bulk phase using the bulk phase concentrations i.e. the diffusion from oil- to oil-filled, and water- to water-filled pores is computed in Equation (5.8) using $C_{i_o}(t) - C_{j_o}(t)$ and $C_{i_w}(t) - C_{j_w}(t)$ respectively (Figure 5.3(a)). For the case of cross-phase diffusion i.e. from water- to oil-filled pores and vice-versa, we use the difference in water concentrations: $C_{i_w}(t) - C_{j_w}(t)$. Indeed, we assume that the polar compounds partition first from the oil to the water phase at the interface between two adjacent pores, then they diffuse within the water phase (Figure 5.3(b)). In this particular case, L_{ji} is taken as only half the length of the water-filled pore.

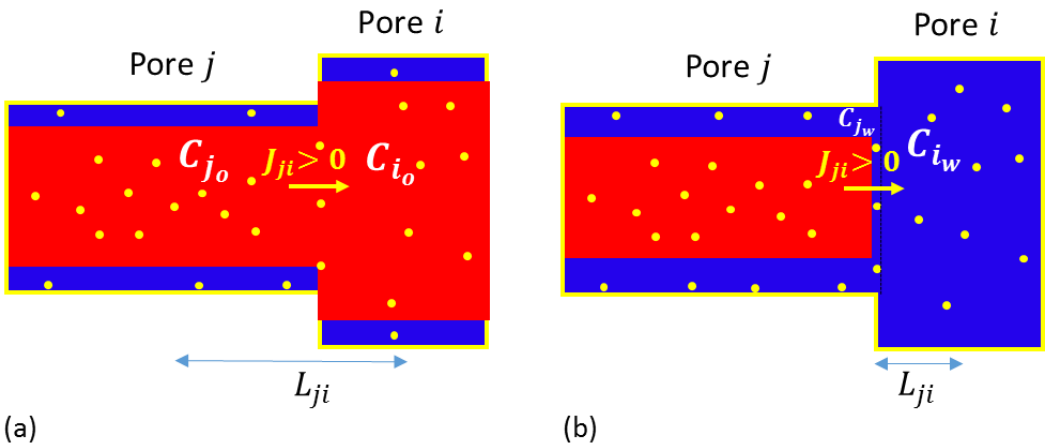

Figure 5.3: Illustration of the diffusion process between (a) two adjacent pores sharing the same bulk (oil) phase and (b) an oil-filled pore adjacent to a water-filled pore (cross-phase diffusion) with the partitioning of polar compounds from the oil to the water phase at the interface and their diffusion within the water phase. Note that C_{i_o} and C_{i_w} are the mobile concentrations of polar compounds in the oil phase and water phase, respectively; J_{ji} and L_{ji} are the diffusion flux and length, respectively, from pore j to pore i. Note as well the colour key provided in Figure 5.2.

c) Adsorption model

The adsorption of polar compounds is assumed to occur from the water phase instantaneously. However, since the polar compounds concentration changes through diffusion at discrete time-steps Δ_t^{TR}, adsorption is only computed at each Δ_t^{TR}. It is described by a Langmuir isotherm which has the following form:

$$\Delta m_{a_i} = SA_i\left(\Gamma_i(t+\Delta_t^{TR}) - \Gamma_i(t)\right)$$
$$\Gamma_i(t+\Delta_t^{TR}) = \Gamma_{max}\frac{KC_{i_w}(t+\Delta_t^{TR})}{1+KC_{i_w}(t+\Delta_t^{TR})} \qquad (5.11)$$

d) Equations summary

<u>Oil-filled pores</u>

To summarise, in an oil-filled pore i at $t+\Delta_t$, we have $\Delta m_{d_i} = \Delta m_{d_i}\left(C_i(t)\right)$ and $\Delta m_{a_i} = \Delta m_{a_i}\left(\Gamma_i(t), \Gamma_i(t+\Delta_t^{TR}), C_{i_w}(t+\Delta_t^{TR})\right)$. Hence, Knowing $\Gamma_i(t)$, $C_{i_o}(t)$ and $C_{i_w}(t)$ from the previous time-step, we combine Equations (5.6), (5.8) and (5.11) to obtain a single quadratic equation that we solve for $C_{i_o}(t+\Delta_t^{TR})$:

$$KP.C_{i_o}(t+\Delta_t^{TR})^2+\left(1-KPB+\frac{\Gamma_{max}KP.SA_i}{V_{i_o}+PV_{i_w}}\right).C_{i_o}(t+\Delta_t^{TR})-B=0 \quad (5.12)$$

where $B=C_{i_o}(t)+\frac{\Delta m_{d_i}+\Gamma_i(t).SA_i}{V_{i_o}+PV_{i_w}}$.

Afterwards, $C_{i_w}(t+\Delta_t^{TR})$ and $\Gamma_i(t+\Delta_t^{TR})$ are directly derived from equations (5.1) and (5.11), respectively. Since the concentration of polar compounds in the inlet is constant, equal to C_0, C_{i_o} and C_{i_w}increase from 0 to C_0 and PC_0, respectively, following the transport model.

We will show below that both the water present in corners and present as a film may collapse in some pores due to polar compounds adsorption; but when this happens, adsorption is assumed to carry on from the oil phase using Equation (5.12), which coincides with Equation (5.13) below for water-filled pores with swapped phases and an adsorption constant equal to $K\times P$.

Water-filled pores

Similarly, for a water-filled pore i, we combine equations (5.7), (5.8) and (5.11), and solve for the unknown $C_{i_w}(t+\Delta_t^{TR})$:

$$K.C_{i_w}(t+\Delta_t^{TR})^2+\left(1-KB+\frac{\Gamma_{max}K.SA_i}{V_i}\right).C_{i_w}(t+\Delta_t^{TR})-B=0 \quad (5.13)$$

where $B=C_{i_w}(t)+\frac{\Delta m_{d_i}+\Gamma_i(t).SA_i}{V_i}$.

$\Gamma_i(t+\Delta_t^{TR})$ is directly derived from equation (5.11). Besides, C_{i_w}increases from 0 to PC_0 following the transport model.

5.2.3 Wettability alteration

Due to the polar species adsorption, the pore surface undergoes a wettability alteration (Bennett et al., 2004). We simply assume that the cosine of the contact angle changes as a linear function of the adsorption level of polar compounds:

$$\cos\theta_i=1-(1-\beta)\frac{\Gamma_i}{\Gamma_{max}} \quad (5.14)$$

While $\Gamma_i=0$, the initial contact angle remains unchanged i.e. $\cos\theta_i=1$. Note that β is an input parameter ranging between 0 and 1, and corresponds to the limiting contact

angle value where $\Gamma_i = \Gamma_{max}$. However, in accordance with the Langmuir adsorption isotherm Equation (5.11), the actual maximum value Γ_{max_actual} that Γ_i can reach as the transport model is carried out is:

$$\Gamma_{max\_actual} = \Gamma_{max} \frac{KPC_0}{1 + KPC_0} \tag{5.15}$$

Hence, by combining Equations (5.14) and (5.15), $\cos \theta_i$ decreases during the simulation from 1 to a minimum value, related to a maximum contact angle θ_{max}:

$$cos\ \theta_{max} = \frac{1 + \beta KPC_0}{1 + KPC_0} \tag{5.16}$$

Consequently, β can be defined as $\beta = cos\ \theta_{max}\ (K \to +\infty)$ at finite C_0 (or as $cos\ \theta_{max}\ (C_0 \to +\infty)$ at finite K). We identify distinct effects of the wetting change in the oil-filled and water-filled pores, as described below.

a) Oil-filled pores

The wetting change in an oil-filled pore may lead to two consequences: the shrinking (and possible collapse) of the water films in the corners, and destabilisation (and possible collapse) of the thin water films that coat the pore walls.

Corner water shrinking

Due to the uniform contact angle change in any angular pore i, water in the pore corners shrinks if it is connected to the outlet. Water may be completely expelled from the pore if it satisfies the condition below:

$$\theta_i > \frac{\pi}{2} - \gamma_i \tag{5.17}$$

where γ_i is the half-angle of the angular cross-sections, as illustrated in Figure 5.4.

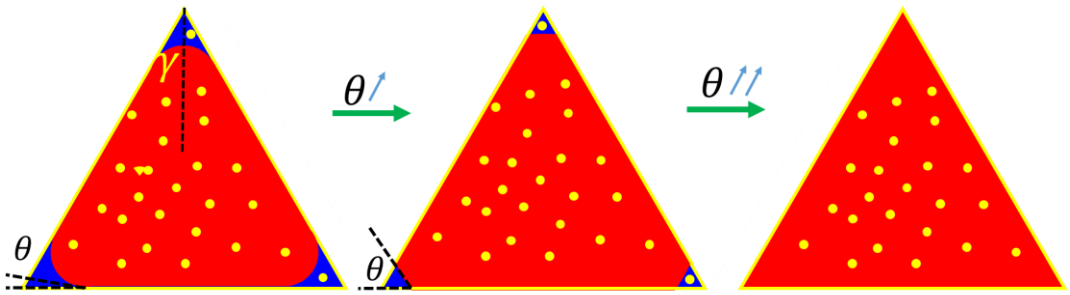

Figure 5.4: Illustration of the corner water shrinking (and possible collapse) due to the contact angle, θ, increase within a pore with triangular cross-section and half-angle γ. Note the colour key provided in Figure 5.2.

A direct consequence of this mechanism is that water may get surrounded by oil in the vicinity of the water films collapse, which generates trapping of water in the network. In fact, the water phase connectivity may drop significantly at this stage due to large contact angle changes.

Notice that during the corner water shrinking process in pore i, we assume for simplicity that Γ_i, C_{i_o} and C_{i_w} are kept constant. As a consequence, if the change in the oil phase volume within the pore is $\Delta V_{i_o} > 0$, an extra mass of polar compounds, $C_{i_o}\Delta V_{i_o}(1-P)$, is assumed to be supplied to the pore from the inlet.

Thin water films destabilisation

The adsorption of polar species affects the stability of thin water films by weakening the bonds that keep them in place. Indeed, at fixed time t, corresponding to a fixed capillary pressure, P_c, thin-film forces exist within the stable water film that support it. The related pressure is the so-called disjoining pressure, Π_i. It is linked to P_c through the augmented Young-Laplace equation (Equation (2.2)), that we have slightly modified by incorporating an adsorption coefficient, $\alpha_i \in [0,1]$:

$$P_c = \alpha_i \Pi_i + \sigma_{ow} c_i \qquad (5.18)$$

where c_i is the equivalent wall curvature of pore i introduced in Section 4.2.

We model α_i as $\alpha_i = \cos\theta_i$. Indeed, when the surface of pore i adsorbs polar compounds, thus increasing Γ_i (Equation (5.14)), α_i decreases from its initial value 1 (no

adsorption). Consequently, Π_i rises to counterbalance it (since P_c is fixed) and the water film gets thinner (Figure 5.5). If Π_i increases enough to reach the critical disjoining pressure Π_{crit} i.e. $P_c > P_{c_i}^* = \alpha_i \Pi_{crit} + \sigma_{ow} c_i$, the film is no longer stable and collapses. Because Π_{crit} is an intrinsic property of the rock (depending on the fluid system and mineralogy of the rock surface), we suppose it is uniform throughout the rock and constant throughout the process.

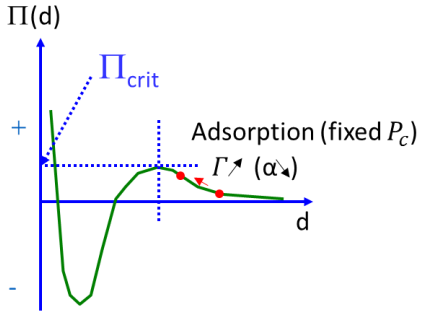

Figure 5.5: Evolution of thin film stability during polar compounds adsorption (increasing Γ i.e. decreasing $\alpha = cos\,\theta$, where Γ and θ are the adsorption level of polar compounds per unit area and contact angle, respectively, linked through Equation (5.14)) at fixed P_c, illustrated on an example of disjoining pressure isotherm $\Pi(d)$.

b) Water-filled pores

As the adsorption levels increase during the transport process in a water-filled pore i adjacent to the oil front, the contact angle increases. Consequently, the pore entry pressure, P_{entry}, decreases, which makes the pore more prone to oil invasion. Oil may then spontaneously invade pore i when its wettability has changed enough for its entry pressure, P_{entry}, to decrease below the current capillary pressure value P_c. Notice that this particular time of spontaneous oil invasion cannot be explicitly determined because of the non-linearity of the relationship between P_{entry} and the contact angle θ.

Note that at θ sufficiently close to $90°$, all the corner water films are removed if connected to the outlet, in accordance with Equation (5.17), and all the entry pressures are close to zero, so all invasions are possible at ${P_c}^{max} > 0$. This justifies the upper limit of $90°$ for θ ($\beta = 0$) introduced above in Equation (5.14), since choosing a higher contact angle has little effect, if any, on the final S_{wi} following primary drainage.

The simulation is stopped when no more invasions are possible at a predefined maximum capillary pressure, P_c^{max} and the adsorption steady-state is reached. The adsorption steady-state is defined as the condition where all the remaining accessible and non-trapped water-filled pores have adsorbed their maximum capacity of polar compounds, i.e. their contact angles have reached a final value equal to θ_{max} (Equation (5.16)). The ultimate water saturation obtained at the predefined P_c^{max} will simply be referred to as S_{wi} (corresponding to an oil saturation $S_{oi} = 1 - S_{wi}$), which is reached at a final time denoted as t_f. We refer to the newly developed model of Primary Drainage during which a Wettability Evolution occurs as PD/WE. An example of the first steps of the simulation is carried out on a regular 2D network and shown in Figure 5.6. It illustrates the various processes involved in the PD/WE model.

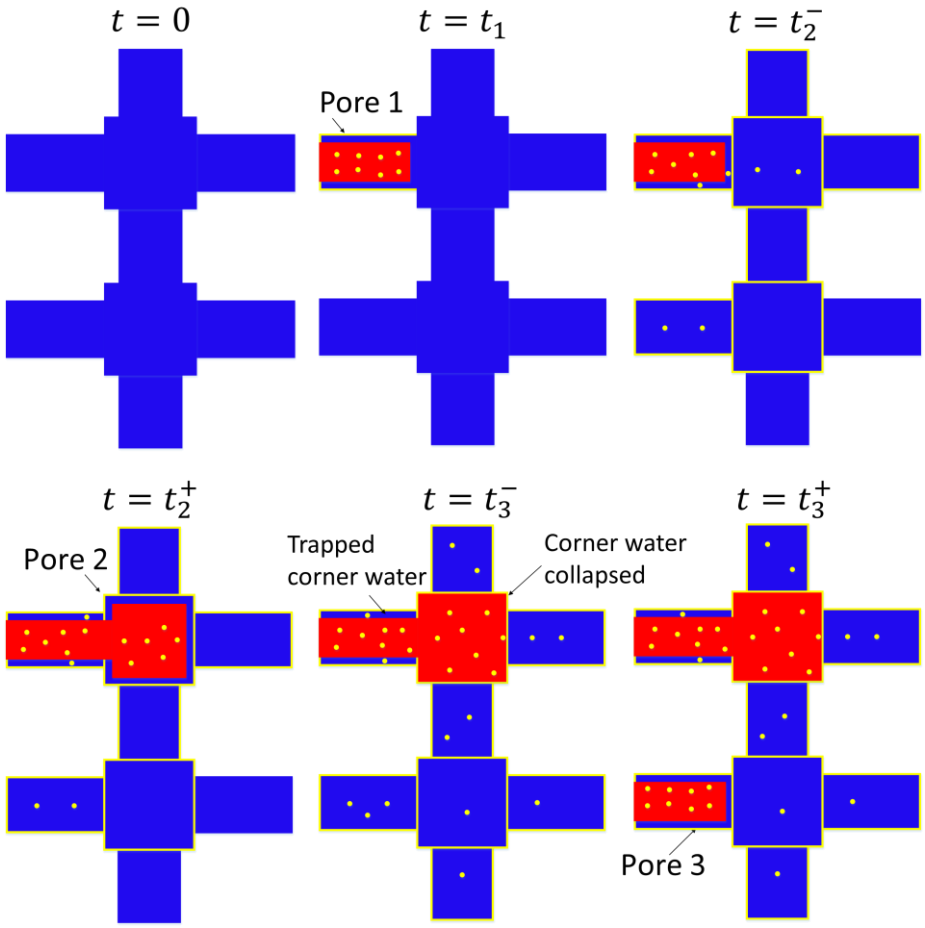

Figure 5.6: Network-scale representation of the PD/WE model, involving the time-dependent oil invasion coupled with the transport model for polar compounds; t_i is the invasion time of pore i, in accordance with the example in Figure 5.1. Oil displaces water from the inlet (left) to the outlet (right) of a 2D regular network. Note the colour key provided in Figure 5.2.

5.3 Results and discussion

The simulations are performed on the same two networks described in Section 3.3. Each network consists of pores with different cross-sectional geometries including regular n-cornered polygons and stars. Note that the 5-cornered star shapes are predominant in both networks, with their corresponding half-angle γ ranging between 5 and $54°$. The latter value corresponds to the pentagon shape.

In this section, we link the pore-scale simulations to the reservoir scale. In fact, we associate each P_c reached locally in the network with a corresponding height, h, in the oil column:

$$h = \frac{P_c}{\Delta\rho . g} \tag{5.19}$$

where $\Delta\rho = \rho_w - \rho_o$ denotes the difference between the fluid volumetric mass densities (here chosen as $0.2\ kg/L$); g denotes the gravity ($9.81\ m/s^2$).

Actually, two main effects will be demonstrated in our simulations, both of which dictate the initial water saturation for waterflooding, S_{wi}:

- The effect of the contact angle, θ_{max} on S_{wi}: while K, P and C_0 are kept constant, β will be varied to induce changes in the contact angles (Equation (5.16)). We either assign a unique β throughout the network, corresponding to a single θ_{max} for all the pores, or uniformly distribute β among the pores, generating a range of contact angles θ_{max}.
- The effect of the balance between oil invasion and wettability alteration on S_{wi}: while we keep the oil flow rate, Q, constant, we vary the maximum adsorptive capacity, Γ_{max}. Hence, the polar compounds adsorption level required to reach the fixed maximum contact angle θ_{max} is changed (Equation (5.15)). This induces changes in the balance between the processes of oil invasion and wettability alteration.

Note that for the latter sensitivity study at fixed θ_{max}, two limiting cases arise:

- In the case of an extremely fast wettability alteration relative to flow rate, a full wetting change within every pore precedes its invasion by oil. Hence, we can

simply model it as a conventional PD with an initial contact angle equal to θ_{max}. We call this special case the Fast Wetting Boundary (FWB).

- If the oil flow rate is much faster than the wetting change, all invasions are supposed to happen instantly. The oil invasion process is carried out until the imposed maximum capillary pressure, P_c^{max}, is reached. Only after this point the wettability alteration takes effect, starting from the inlet, resulting in subsequent spontaneous oil invasions. We refer to this limiting case as Slow Wetting Boundary (SWB).

5.3.1 Berea sandstone network

We simulate the above PD/WE model on the homogeneous Berea network described in Section 3.3.1. The base case parameters of the simulations are summarised in Table 5.1. Note that the chosen β, K, P and C_0 parameters correspond to $\theta_{max} = 80°$ (Equation (5.16)). Although our base case parameters have not been derived from a particular experiment, they are physically realistic, chosen in order to scan all the possible outcomes of our model during the sensitivity analysis that will follow.

$Q\ [m^3/s]$	5e-13
$C_0\ [mg/L]$	500
$\Delta_t^{TR}[s]$	0.007
P	0.01
$D\ [cm^2/s]$	1e-5
$K\ [L/mg]$	1
$\Gamma_{max}[mg/m^2]$	0.3
β	0.0083
$P_c^{max}\ [kPa]$	6600

Table 5.1: Base case parameters for Scenario 2 simulations in the Berea network. Only the last three parameters are varied during the sensitivity study.

a) Primary Drainage

We first start with the case where polar compounds remain in the oil phase (no partitioning, $P = 0$), hence they do not react with the surface i.e. $\theta_{max} = 0$ (Equation (5.16)). This corresponds to the conventional PD simulation at a predefined P_c^{max}. The pore occupancies are shown in Figure 5.7. Note that in the absence of wetting change, the water saturation reaches $S_{wi} = 0.2$, after which no more invasions are possible at fixed P_c^{max}.

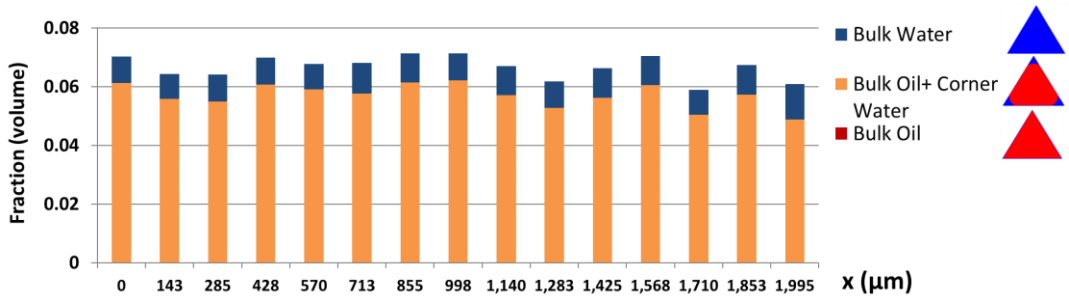

Figure 5.7: Pore occupancies for the Berea network shown on the x-axis (parallel to flow, from inlet (left) to outlet (right)) following a conventional PD at $P_c^{max} = 6600\ Pa$ (i.e. PD/WE for the base case parameters – with $P = 0$ or $\theta_{max} = 0°$). The simulation reached $S_{wi} = 0.2$ at P_c^{max} after time $t_f = 53\ min$.

We now run the PD/WE model for the base case parameters (Table 5.1). Two effects are opposing each other in terms of changing S_{wi} following the PD/WE model. On the one hand, the corner water collapse in oil-filled pores due to the contact angle change, as described in Section 5.2.3(a), results in a loss in water phase connectivity. This effect, that we call "trapping", tends to increase S_{wi}. On the other hand, the decrease of entry pressures, P_{entry}, due to the contact angle change as described in Section 5.2.3(b), results in a gain in entry pressure accessibility. This effect, that we call "enterability", tends to counterbalance the "trapping" effect by decreasing S_{wi}. It follows from the definitions that both the "enterability" and "trapping" effects increase with θ_{max}.

The pore occupancies and wettability change following PD/WE at intermediate-wet conditions ($\theta_{\max} = 80°$) are shown in Figure 5.8. The PD/WE at $\theta_{max} = 80°$ resulted in a slightly higher $S_{wi} = 0.22$ compared to the PD $S_{wi} = 0.2$, meaning that the "trapping" effect is slightly dominating in this case. In fact, in the intermediate-wet conditions that we are considering (80^0), the drop in water connectivity is so large that the water phase gets disconnected at $S_w = 0.4$ ($\widehat{\chi_{wat}} = 0$ in Figure 5.9). Note that for $\theta_{max} = 80^0$, the

majority of the remaining corner water at t_f (shown in Figure 5.8(b)-upper) must be trapped. Indeed, most of the shapes half-angles γ are larger than $10°$, thus according to Equation (5.17), the corner films should have been expelled, if there was any outlet connection. Note as well that only a fraction of the pores belonging to the last column in the x-axis in Figure 5.8 represent the outlet bonds, since it also includes pores with a range of distances from the outlet. This explains the presence of trapped water in the corners of these particular pores. Besides, it is clear from the transition Figure 5.8(a)-lower to Figure 5.8(b)-lower that the wettability change occurs preferentially near the inlet at the beginning of the simulation, with the contact angle values, θ, ranging from 0 to θ_{max}. This qualitatively reproduces the early wetting alteration observed by Bennett et al. (2004) using FESEM imaging on surfaces near the inlet. Eventually, the adsorption steady state is reached at t_f where a single contact angle θ_{max} governs the pore space.

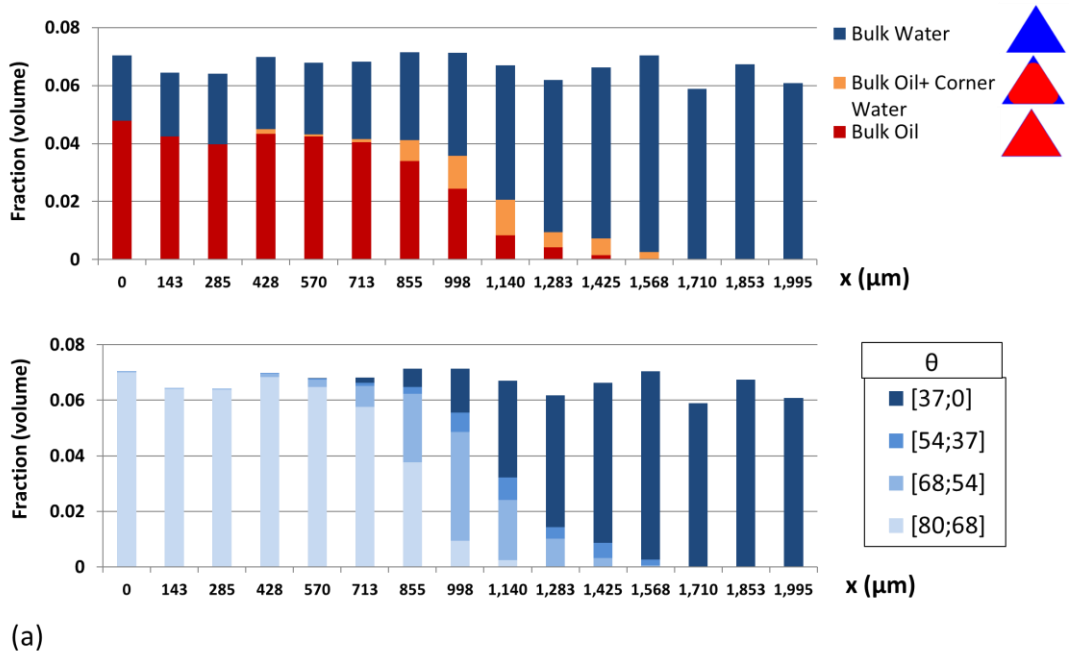

(a)

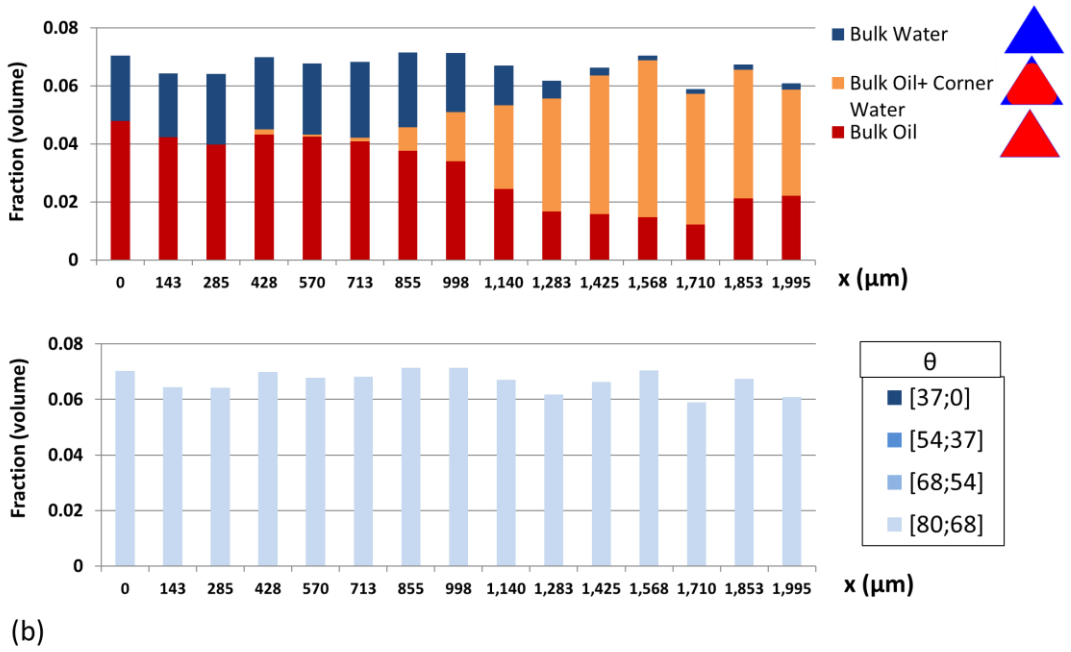

(b)

Figure 5.8: Pore occupancies (upper) and (altered) contact angles (lower) for the Berea network shown on the x-axis (parallel to flow, from inlet (left) to outlet (right)) following PD/WE for the base case parameters after (a) $t_{1/2} = 31\ min$ (at which $S_w \approx \frac{S_{wi}+1}{2}$) and (b) $t_f = 315\ min$ ($S_{wi} = 0.22$ at $P_c{}^{max}$).

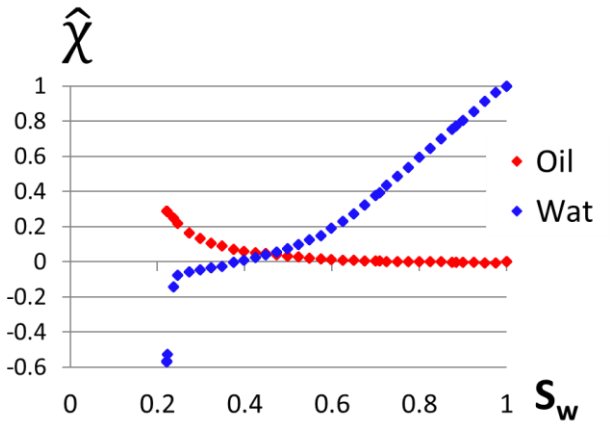

Figure 5.9: Evolution of the oil and water phases connectivities (normalised Euler numbers) during PD/WE for the base case parameters in the Berea network.

Effect of θ_{max} on S_{wi}

The pore occupancies and wettability change following PD/WE at water-wet conditions ($\theta_{max} = 30°$) are shown in Figure 5.10. Note that at this relatively low θ_{max}, corner water mostly persists and is not trapped. This is shown in the pore occupancies (Figure 5.10-upper) and confirmed in Figure 5.11 as the water phase connectivity remains at its maximum level ($\widehat{\chi_{wat}} = 1$). Consequently, the "trapping" effect is inhibited in this case, which leaves the "enterability" effect. Thus, quite a modest change in wetting in the PD/WE model in this case has led to the value of $S_{wi} = 0.14$ i.e. the invasion of an additional $\Delta S_o = 0.06$ above the PD oil saturation. Note that the pore occupancies at $t_f = 16762s$ ($S_{wi} = 0.14$ at P_c^{max}) are similar to the $\theta_{max} = 0°$ case shown in Figure 5.7, and the corresponding full wetting change up to $\theta_{max} = 30°$ is analogous to that showed in Figure 5.8(b)-lower.

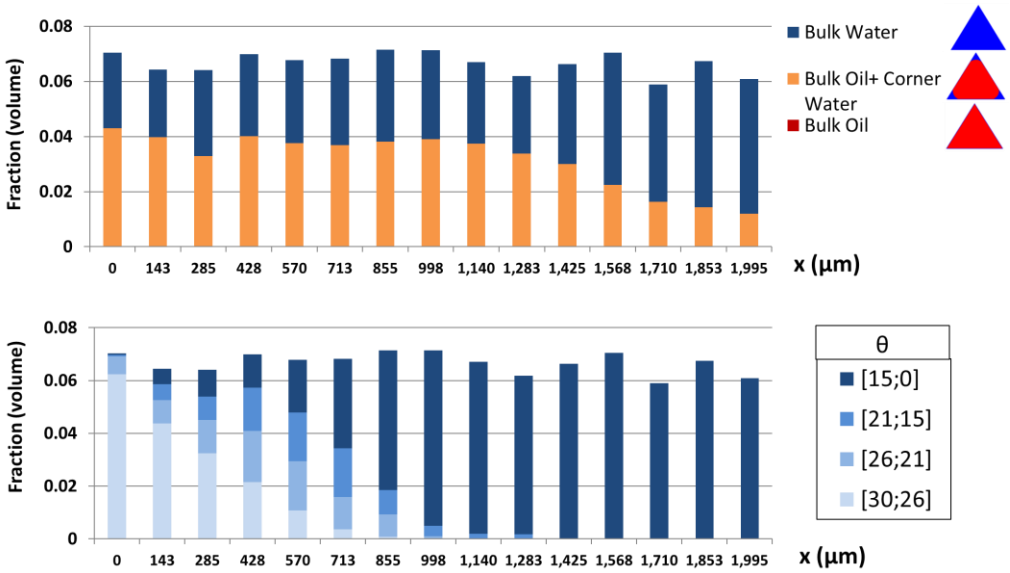

Figure 5.10: Pore occupancies (upper) and (altered) contact angles (lower) for the Berea network shown on the x-axis (parallel to flow, from inlet (left) to outlet (right)) following PD/WE for the base case parameters – with $\theta_{max} = 30°$ – after $t_{1/2} = 29\ min$ (at which $S_w \approx \frac{S_{wi}+1}{2}$).

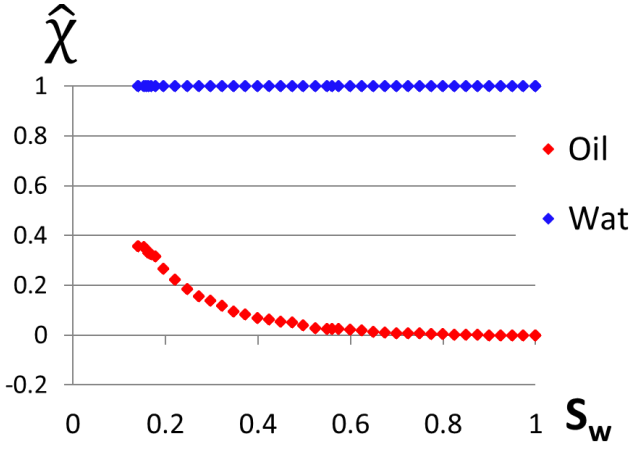

Figure 5.11: Evolution of the oil and water phases connectivities (normalised Euler numbers) during PD/WE for the base case parameters – with $\theta_{max} = 30°$ – in the Berea network.

The dependency of S_{wi} on the number of Pore Volumes (PV) of oil injected for each θ_{max} value is described in Figure 5.12. It shows that each PD/WE simulation curve ($\theta_{max} > 0$) is made up of two distinct portions:

- An oblique line at low PV (< 1), where most of the water is displaced by oil.

- A nearly-horizontal portion at higher PV, reaching up to 5 PV, where the decrease in water saturation is slow. This occurs after oil break-through when the predefined P_c^{max} is reached and the oil keeps flowing through the outlet, while the polar compounds are resupplied from the inlet and further interact with the surface. Consequently, the entry pressures of the remaining water-filled pores keep deceasing and whenever one of them decreases below P_c^{max}, it is invaded by oil. This keeps going for as much PV as needed for the adsorption steady-state to be reached (corresponding to the curves endpoints).

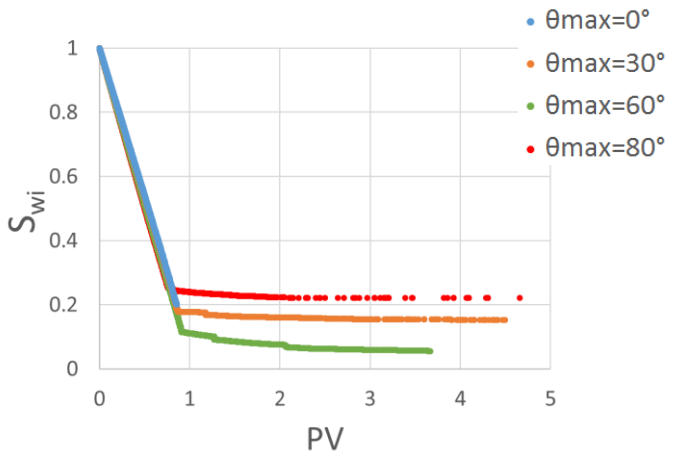

Figure 5.12: S_{wi} as a function of PV for the base case parameters – with different θ_{max} imposed, in the Berea network.

The pore occupancies shown on the pore-size distribution (PSD) in Figure 5.13 demonstrate quite clearly that the PD/WE model enables the oil to reach the smallest pores that would not have been accessible following the conventional PD ($\theta_{max} = 0°$) at the same fixed P_c^{max}.

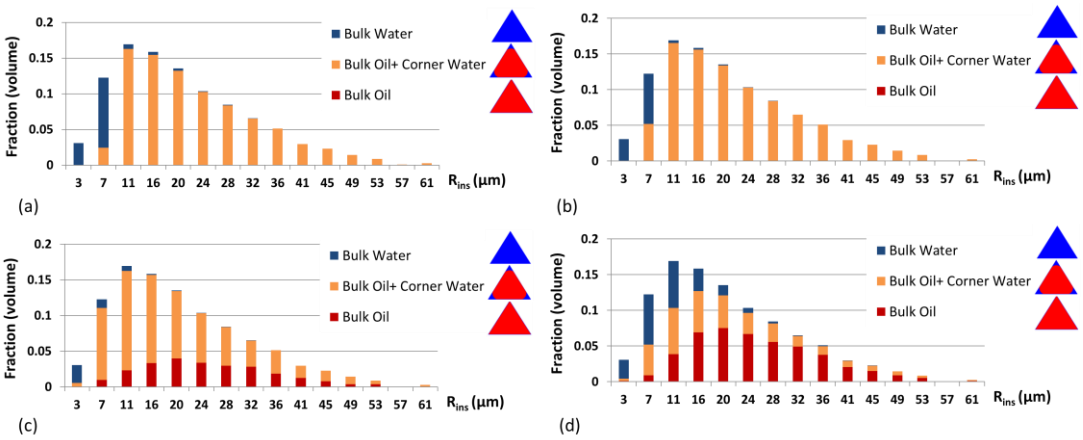

Figure 5.13: Pore occupancies for the Berea network shown on the pore-size distribution following PD/WE for the base case parameters – with (a) $\theta_{max} = 0°$ *(*$S_{wi} = 0.2$*); (b)* $\theta_{max} = 30°$ *(*$S_{wi} = 0.14$*); (c)* $\theta_{max} = 60°$ *(*$S_{wi} = 0.05$*) and (d)* $\theta_{max} = 80°$ *(*$S_{wi} = 0.22$*).*

Effect of Γ_{max} on S_{wi}

We now keep θ_{max} as the base case value (80°) and increase Γ_{max} from 0.3 to 1.5 $\frac{mg}{m^2}$ i.e. induce a slower wetting change relative to oil invasion by requiring a higher polar component adsorption level to alter the contact angle. It is clear from the pore occupancy and wettability change in Figure 5.14(a) that, during the PD/WE process, the oil front is well ahead of the wettability alteration front in the direction of flow. This behaviour is different from that shown for the base case in Figure 5.8(a) where the two processes are clearly more synchronised. This higher Γ_{max} results in a slower decrease in the water phase connectivity, as shown in Figure 5.15, with $\widehat{\chi_{wat}} = 0$ at a water saturation $S_w = 0.14$, which is significantly lower than the base case value (0.4). As a consequence, the "trapping" effect is delayed and its effect is weaker. Since the "enterability" effect is insensitive to Γ_{max}, only depending on θ_{max}, this results in $S_{wi} = 0.09$ being significantly lower than the base case value (0.22). Note that the final wettability distribution at t_f is identical to that shown in Figure 5.8(b)-lower.

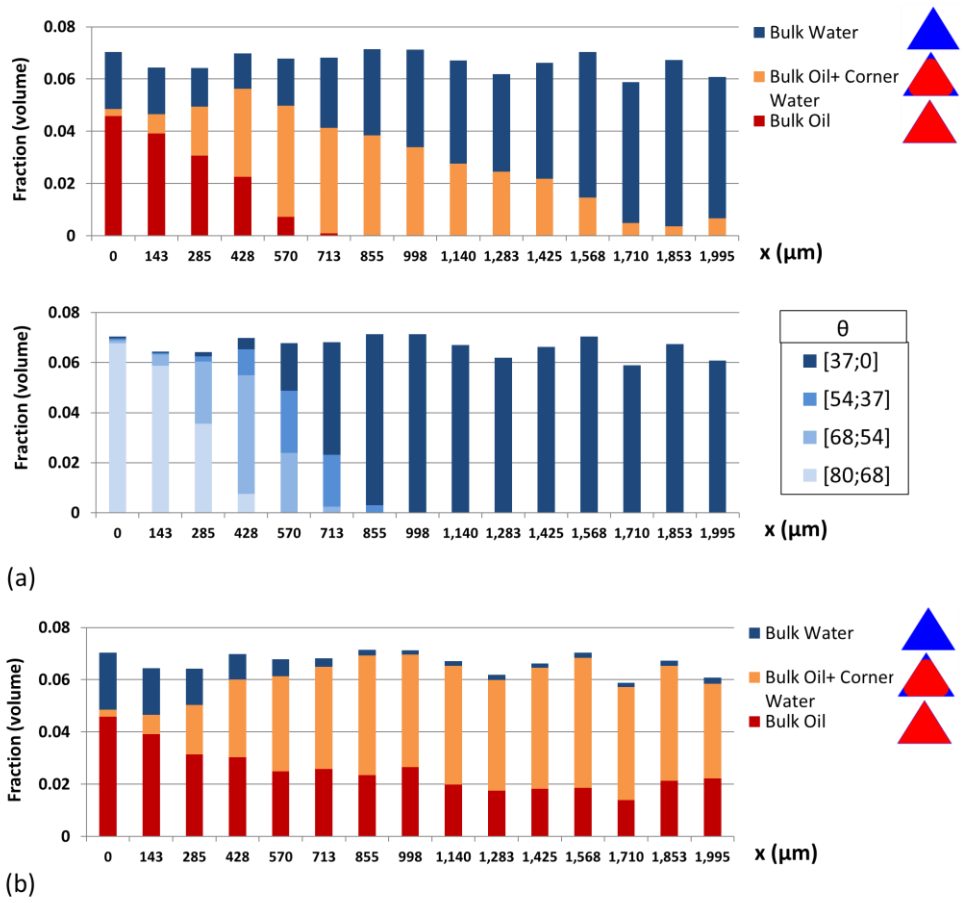

Figure 5.14: (a) Pore occupancies (upper) and (altered) contact angles (lower) for the Berea network shown on the x-axis (parallel to flow, from inlet (left) to outlet (right)) following PD/WE for the base case parameters – with $\Gamma_{max} = 1.5\ \frac{mg}{m^2}$ *– after* $t_{1/2} = 32\ min$ *(at which* $S_w \approx \frac{S_{wi}+1}{2}$*) and (b) Pore occupancies (only) at* $t_f = 433\ min$ *(*$S_{wi} = 0.09$ *at* P_c^{max}*).*

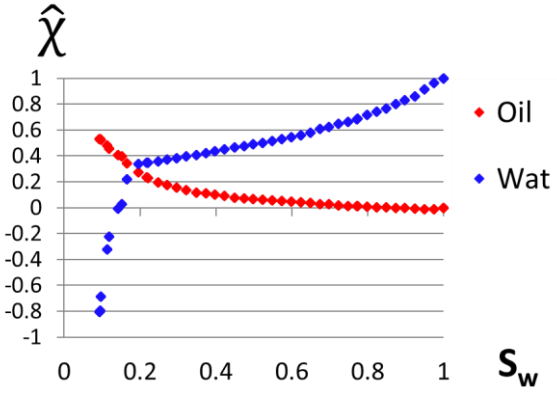

Figure 5.15: Evolution of the oil and water phases connectivities (normalised Euler numbers) during PD/WE for the base case parameters – with $\Gamma_{max} = 1.5\ \frac{mg}{m^2}$ *– in the Berea network.*

Similar to Figure 5.12, we show S_{wi} as a function of network PV throughput for each Γ_{max} value in Figure 5.16. The behaviour is generally the same, with the presence of the two distinctive portions at low and high PV. Nonetheless, an exception occurred at the lowest chosen Γ_{max} (0.03) for which the simulation stopped early. In this case, the high amount of trapping generated due to the fast wetting change relative to oil invasion resulted in no further displacements being available at a relatively early stage, which is purely due to a lack of physical accessibility, regardless of the increased entry pressure accessibility i.e. "enterability".

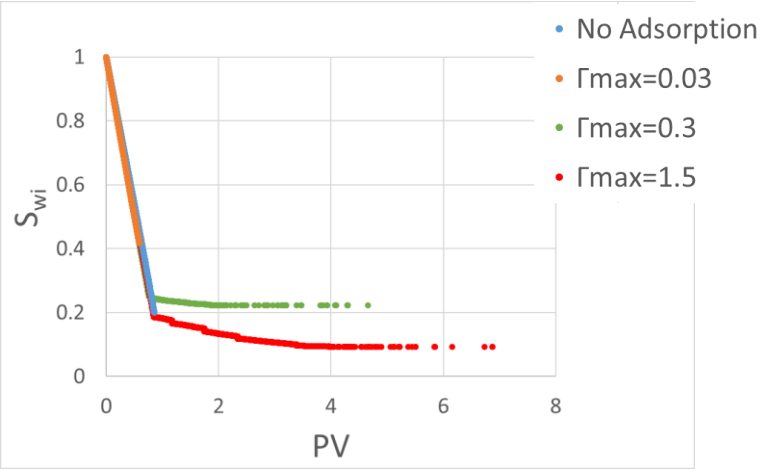

Figure 5.16: S_{wi} as a function of PV for the base case parameters – with different $\Gamma_{max}[\frac{mg}{m^2}]$ imposed – and the "No Adsorption" case, in the Berea network.

We now aim to link the simulations to the behaviour observed by Bennett et al. (2004) in their core-flood experiment. To do so, we focus on the evolution of the average mobile concentration of polar compounds in the oil phase at the outlet bonds, depending on the system adsorptive capacity, as described by Figure 5.17. For the "No partitioning" case, describing a conventional PD process where polar compounds do not partition from the oil into the water phase, these polar species emerge at the outlet at their maximum concentration and exactly when oil breaks through ($t = 707s$). Besides, when the adsorptive capacity, Γ_{max}, increases, we observe a clear delay in the appearance of polar compounds at the outlet due to a higher surface activity. Additionally, the high concentration at which they appear for the $\Gamma_{max} = 0.03$ case is mainly a contribution of the oil invasion process which carries polar compounds all through the network in the absence of any substantial surface activity, as described in 5.2.1. For higher Γ_{max}, when the adsorptive capacity of the system is significant, the oil

phase appears at the outlet depleted of polar species, which are then resupplied from the inlet through a diffusion process, as described in 5.2.2. The simulations qualitatively reproduce the experimental trends provided in Figure 2.3(a), with the polar species "fluoren-9-one", "carbazole", "benzocarbazole" and "p-cresol" corresponding to an increasing surface activity (i.e. higher Γ_{max}), in order. Note that each curve's endpoint corresponds to the adsorption steady-state being reached. At the latter, all the pores in the network have reached maximum adsorption levels, hence maximum wetting change, regardless of the final mobile concentrations. Ultimately, the average mobile concentration of polar compounds in the oil phase at the outlet bonds (normalised by C_0), $\widehat{C_{outlet}}$, would reach its maximum value, equal to 1, but this would not affect the final contact angles and initial water saturation attained.

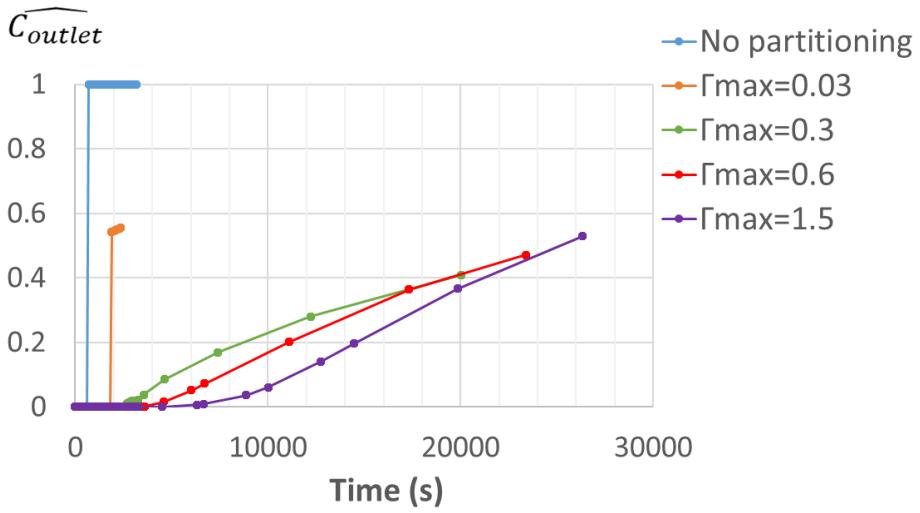

Figure 5.17: The evolution in time of the average mobile concentration of polar compounds in the oil phase at the outlet bonds, normalised by C_0, for the base case parameters – with different $\Gamma_{max}[\frac{mg}{m^2}]$ imposed – and the "No partitioning" case, in the Berea network.

The pore occupancies shown on the pore-size distribution in Figure 5.18, combined with Figure 5.13(d) (for $\Gamma_{max} = 0.3\frac{\mathrm{mg}}{\mathrm{m}^2}$), reveal that a slower wetting change relative to oil invasion i.e. higher Γ_{max}, at intermediate-wet conditions, leads to a higher volume of small pores being invaded following PD/WE. Indeed, the invasion process is driven further due to a weaker "trapping" effect.

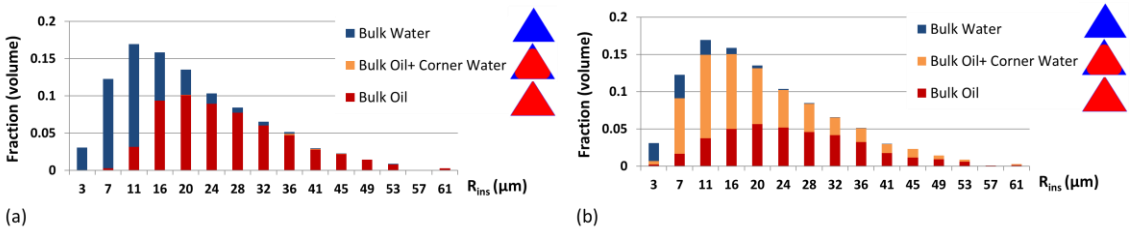

Figure 5.18: Pore occupancies for the Berea network shown on the pore-size distribution following PD/WE for the base case parameters – with (a) $\Gamma_{max} = 0.03$ *(*$S_{wi} = 0.42$*) and (b)* $\Gamma_{max} = 1.5\ \frac{mg}{m^2}$ *(*$S_{wi} = 0.09$*).*

Combined effect of θ_{max} and Γ_{max} on S_{wi}

The combined effects of θ_{max} and Γ_{max} on S_{wi} at fixed P_c^{max} are summarised in Figure 5.19. Note that the case $\theta_{max} = 0°$, corresponding to the conventional PD, is shown for comparison purposes, as the notion of Γ_{max} is not applicable in the absence of adsorption. The results are clearly non-monotonic with regard to θ_{max}, which can be interpreted by the competition between the two opposing effects: "enterability" and "trapping", as follows:

- For intermediate-wet conditions ($\theta_{max} = 80°$), where both the "trapping" and "enterability" effects are significant, S_{wi} monotonically decreases with faster oil invasion relative to wetting change i.e. higher Γ_{max}. Indeed, S_{wi} decreases from a value of 0.41, significantly higher than the $\theta_{max} = 0°$ case (0.2), to a value as low as 0.09. This, as explained above, is due to the "trapping" effect getting delayed at higher Γ_{max}.
- Switching to weakly water-wet conditions ($\theta_{max} = 60°$), leads to much lower S_{wi}, with the gap narrowing at high Γ_{max}. In fact, while both the "enterability" and "trapping" effects get weaker, the loss in "enterability" is lower than the decrease in "trapping", meaning that the former dominates.
- For water-wet conditions ($\theta_{max} = 30°$) where "trapping" is inhibited, S_{wi} is not sensitive to Γ_{max}. This is reasonable since by slowing down the wettability alteration compared to the oil invasion, only the pore-filling sequence is likely to change due to the wettability alteration. And in the absence of any generated trapping, this does not affect the final S_{wi}.

- Finally, by uniformly distributing $\theta_{max} \in [0,80°]$, the resulting "S_{wi} vs. Γ_{max}" curve lies between the $\theta_{max} = 60$ and $80°$ cases.

Note that S_{wi} for both $\theta_{max} = 60$ and $80°$ reside between their respective slow and fast wetting boundaries (SWB and FWB, respectively), as expected. Moreover, while the FWB increases with higher θ_{max} due to a more important "trapping" effect, the SWB coincides for the two contact angles considered.

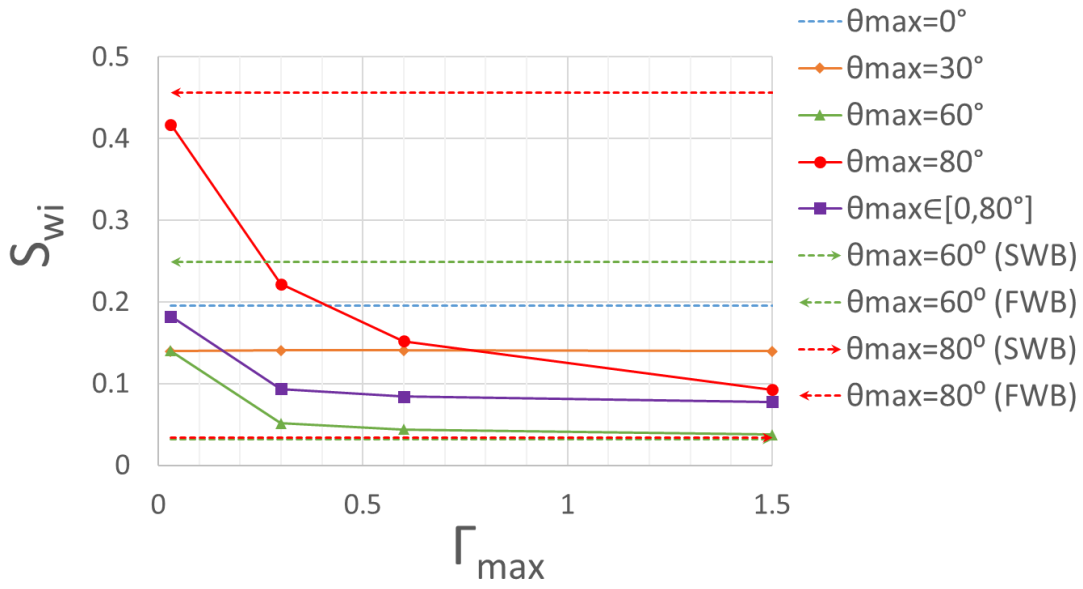

Figure 5.19: The resulting S_{wi} as a function of Γ_{max} $[\frac{mg}{m^2}]$ following the PD/WE model in the Berea network for the base case parameters – with different θ_{max} values. FWB and SWB are the limiting fast wetting and slow wetting boundaries, respectively.

The predicted effect of the PD/WE model on conventional calculations of the oil column saturation are now described. The S_w vs. height, h, above the oil water contact (OWC) is traditionally calculated using the PD curve, and this is shown in Figure 5.20 (denoted $\theta_{max} = 0°$). A series of simulations of the PD/WE model were carried out by varying the main pair of parameters $(\theta_{max}, \Gamma_{max})$ at different P_c^{max} values, each corresponding to a different height, h, in the oil column (Figure 5.20). This is a generalisation of the previous simulations shown in Figure 5.19 that correspond to a fixed P_c^{max} i.e. a horizontal line in the oil column ($h = 3.3m$). By applying the PD/WE model ($\theta_{max} > 0°$), significant changes in phase saturations occur within the oil column, depending on θ_{max} and Γ_{max}, as follows:

- For $\theta_{max} = 80°$, the curves for the different chosen Γ_{max} lie between the boundaries FWB and SWB, with higher Γ_{max} leading to monotonically lower S_{wi}. Additionally, the model may result in significant non-zero water saturations, even high in the oil column. In fact, for a relatively fast wetting change ($\Gamma_{max} = 0.03$), we observe a vertical curve. This is due to the significant amount of water trapping being created at a relatively early stage that inhibits any further displacement, independent of how high the attained P_c^{max} (or h) becomes.
- The $\theta_{max} = 60°$ curves follow the same behaviour as the $\theta_{max} = 80°$ case, but with a narrower gap between these curves as FWB is shifted to the left. Indeed, a less important "trapping" effect compared to the previous case leads to S_{wi} being lower all along the oil column. Note that the two slow wetting boundaries (SWB) for $\theta_{max} = 60$ and $80°$ coincide.
- The $\theta_{max} = 30°$ curve, which is insensitive to Γ_{max}, is shifted to the left as compared to the conventional PD curve. In other words, PD/WE at water-wet conditions leads to lower water saturations all along the oil column. In fact, even at the highest point of the curve where all the pores are prone to invasion at $\theta_{max} = 0°$, S_{wi} is slightly lower due to the shrinking of water in the corners.

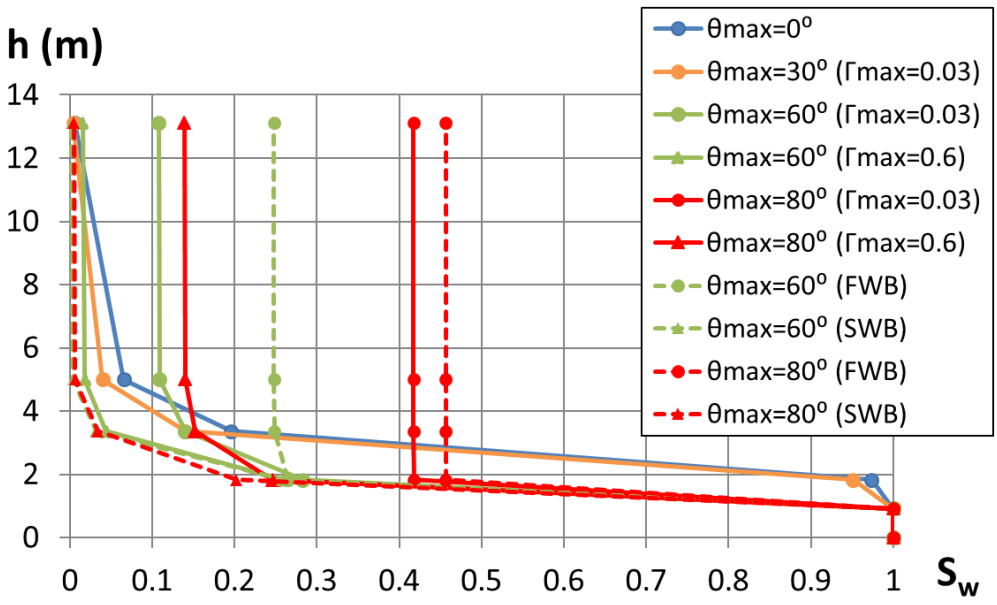

Figure 5.20: Distribution in the oil column in the Berea network following the PD/WE model for the base case parameters – with different combinations of θ_{max} and $\Gamma_{max}[\frac{mg}{m^2}]$ values. FWB and SWB are the limiting fast wetting and slow wetting boundaries, respectively.

Sensitivities to other parameters

- ***Impact of Q***

In this subsection, we assess the impact of the oil flow rate, Q, on S_{wi} while keeping Γ_{max} constant. In other words, the balance between the oil invasion and wetting change processes is changed by varying the oil flow speed while keeping the system adsorptive capacity constant. Note that this model is not truly dynamic but it assigns a relative time ratio between the oil charge rate and changes in the wetting state (governed by the adsorptive capacity).

The dependency of S_{wi} on Q for different θ_{max} values is illustrated in Figure 5.21. The qualitative behaviour is identical to the base case (see Figure 5.19). Hence, as expected, the effect of the balance between oil invasion and wetting change on S_{wi} is similar by changing the speed of either of the processes while keeping the other one constant.

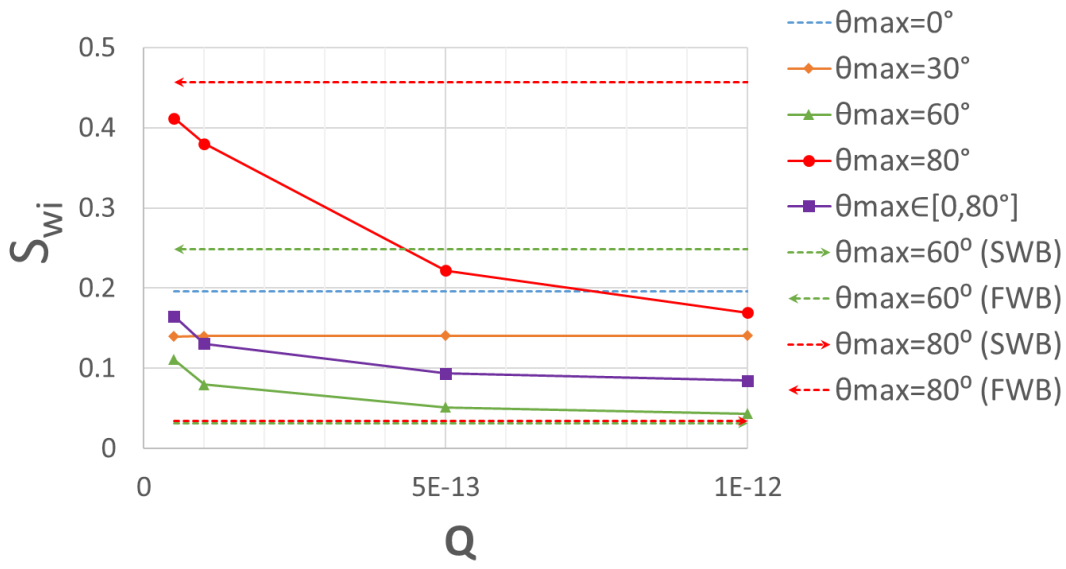

Figure 5.21: The resulting S_{wi} as a function of Q $[\frac{m^3}{s}]$ following the PD/WE model in the Berea network for the base case parameters – with different θ_{max} values. FWB and SWB are the limiting fast wetting and slow wetting boundaries, respectively.

- ***Impact of the invasion model***

As a further sensitivity analysis, we evaluate the impact of the time-dependent invasion model on the overall behaviour. We propose a model different from that described in Section 5.2, for which the cumulative volume increases linearly over time. Instead, we

assume in this subsection that the *capillary pressure*, P_c, increases linearly over time: $P_c(t) = \psi * t$, where t[s] is the migration time and ψ is an input parameter with the unit of $Pa.s^{-1}$. We assume that a pore i is instantaneously invaded when its entry pressure, P_{entry_i}, is overcome. However, this linear increase ceases when P_c reaches the predefined P_c^{max}, as described in Figure 5.22. Note that, at $P_c = P_c^{max}$, all the remaining invasions become instantaneous, given that the pore is accessible, non-trapped and its entry pressure is overcome. As in the previous model, the transport model for polar compounds is carried out at discrete time-steps Δ_t^{TR} between two successive invasions. Note that due to the adsorption of polar compounds and the resulting decrease in P_{entry} (see Section 5.2.3(b)), the invasion process is speeded up, especially at large contact angles.

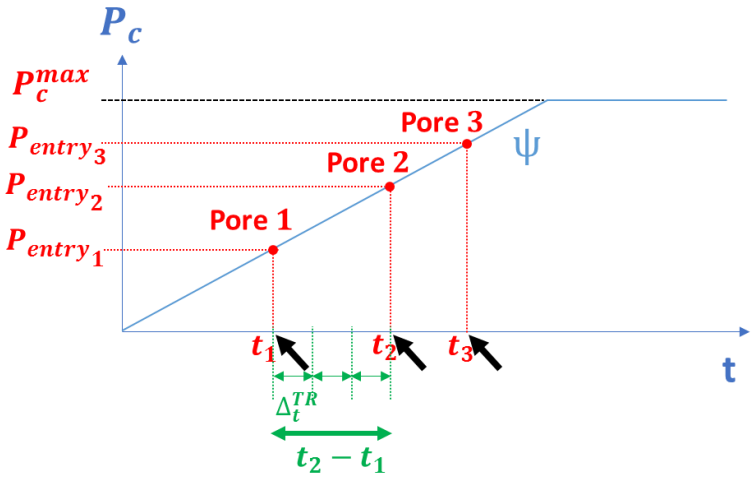

Figure 5.22: Illustration of the alternative time-dependent oil invasion model, similar to that described in Figure 5.1 , but here the capillary pressure increases linearly over time at constant ψ $[Pa.s^{-1}]$ *until it reaches the predefined maximum capillary pressure,* P_c^{max}. *Note that* P_{entry_i} *denotes the entry pressure of pore* i.

The resulting S_{wi} curves as a function of Γ_{max} for the different imposed θ_{max} is shown in Figure 5.23, using the base case parameters shown in Table 4.1, with the exception that Q is here replaced by ψ (introduced above), chosen equal to $10\ Pa.s^{-1}$. It is clear that the time-dependent capillary pressure model exhibits the same qualitative trends as the initial model. Indeed, on the one hand, S_{wi} is insensitive to Γ_{max} for $\theta_{max} = 30°$. On the other hand, S_{wi} monotonically decreases with higher Γ_{max} for $\theta_{max} = 60°$ and $80°$, and lies between the fast and slow wetting boundaries FWB and SWB, respectively. Since the models are qualitatively similar, all earlier conclusions must hold.

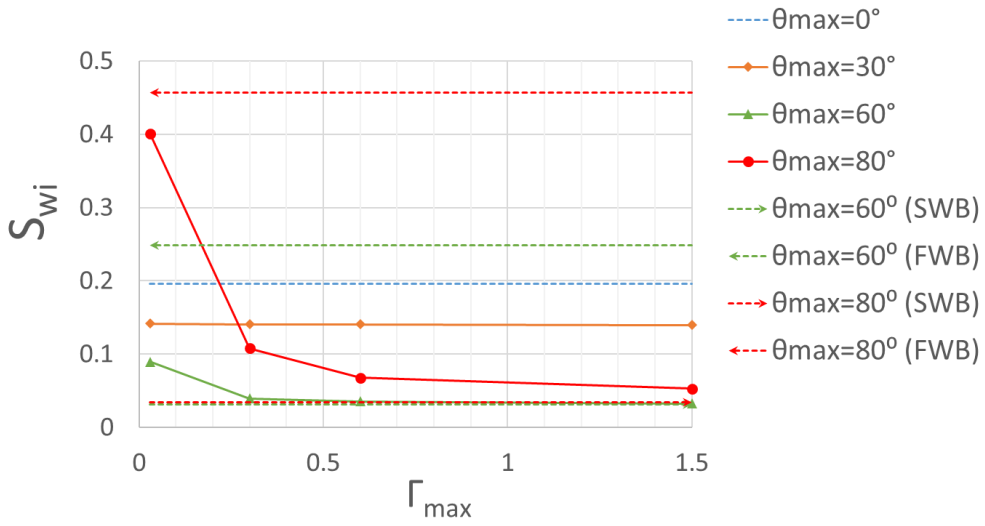

Figure 5.23: The resulting S_{wi} as a function of Γ_{max} $[\frac{mg}{m^2}]$ following the PD/WE model using an alternative time-dependent capillary pressure model in the Berea network. The base case parameters are used – except for Q replaced by $\psi = 10\ Pa.s^{-1}$– with different θ_{max} values. FWB and SWB are the limiting fast wetting and slow wetting boundaries, respectively.

b) Waterflood

In the previous Section 5.3.1(a), we have applied the Primary Drainage/Wettability Evolution (PD/WE) model. This has resulted in a range of final pore-scale fluid configurations and wetting states, characterised by the main parameters of the PD/WE model: θ_{max}; Γ_{max} at fixed Q (or vice-versa) and P_c^{max} (or h). In this section, we consider subsequent imbibition processes by simulating water displacements in the Berea network.

No ageing

In this first part, we simulate a waterflood in the Berea network, assuming it does not undergo any changes in wettability other than the mild wettability alteration at θ_{max} that occurred during primary drainage.

The pore occupancies at the end of the waterflood at fixed $h = 3.3m$ for different θ_{max} values are shown in Figure 5.24, corresponding to the PD/WE simulations shown in Figure 5.13. For pores exclusively filled with water, we distinguish whether it was initially water-filled, or invaded through snap-off or piston-like displacements. We observe a decrease in the frequency of snap-off displacements in favour of regular piston-like

displacements when switching from perfectly (0°) to slightly less water-wet conditions (30°). Further, close to intermediate-wet conditions ($\theta_{max} = 60°$ and $\theta_{max} = 80°$), snap-off is completely inhibited; this results in the mechanism of water invasion becoming not directly dependent on θ_{max}, but rather indirectly through the initial oil configuration (mainly S_{oi} and the amount of corner water), which is different for each θ_{max}.

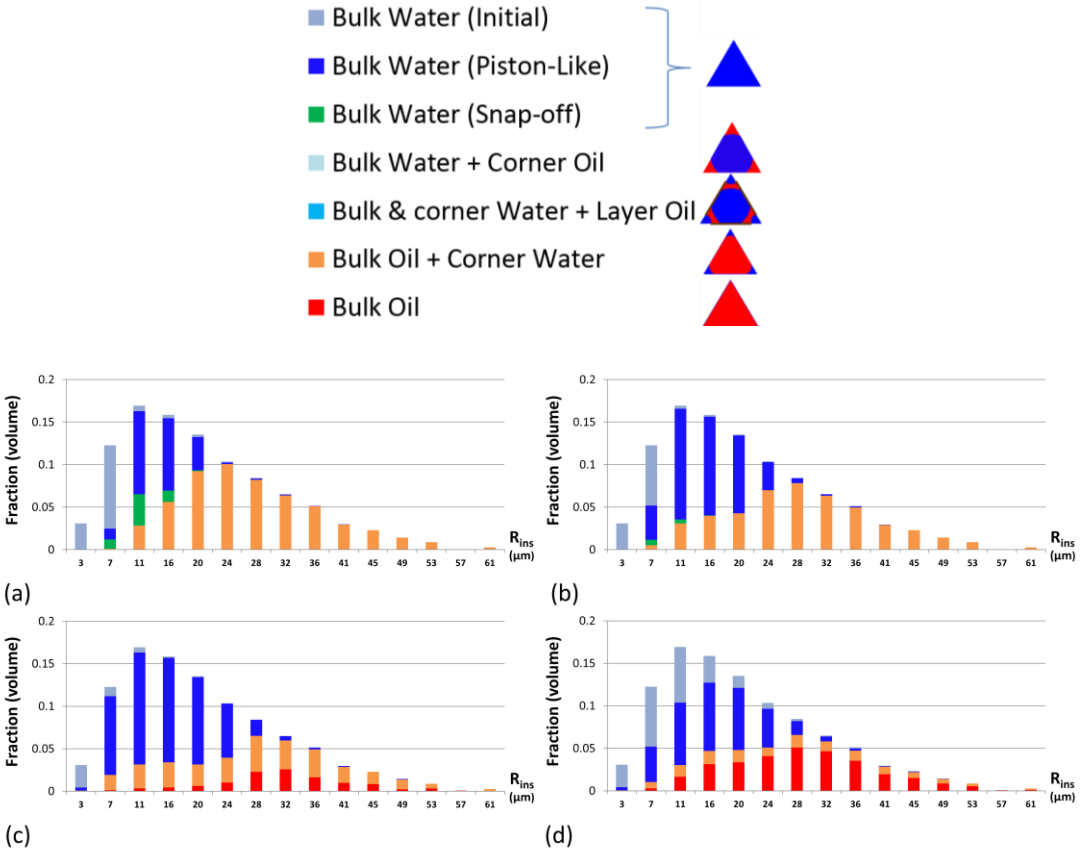

Figure 5.24: Pore occupancies at the end of the waterflood after PD/WE for the base case parameters – with (a) $\theta_{max} = 0°$($S_{oi} = 0.8; S_{or} = 0.48$), (b) $\theta_{max} = 30°$ ($S_{oi} = 0.86; S_{or} = 0.4$), (c) $\theta_{max} = 60°$ ($S_{oi} = 0.95; S_{or} = 0.4$) and (b) $\theta_{max} = 80°$ ($S_{oi} = 0.78; S_{or} = 0.44$) , shown on the pore size distribution for the Berea network (no ageing). Note the colour key (top) for the various pore-level displacements.

More generally, each S_{oi} obtained following PD/WE for each chosen θ_{max} and height h at constant Γ_{max} (corresponding to a single data point in Figure 5.20) leads to S_{or} subsequent to waterflood, as illustrated in Figure 5.25(a). The latter shows that the change from perfectly (0°) to slightly less water-wet conditions (30°) significantly reduces S_{or}, especially at high S_{oi} , mainly due to fewer snap-off events. Indeed, snap-

off usually tends to considerably decrease the oil phase connectivity as the swelling of water wetting films creates disconnected oil clusters. Although the water saturation remaining in the corner is lower for the $30°$ contact angle due to the shrinking of the wetting films that occurred during PD/WE, this was compensated by the strong effect of the reduction of snap-off. Both $\theta_{max} = 0°$ and $30°$ S_{or} curves reach a plateau at high S_{oi}. In contrast, for higher θ_{max} ($60°$ and $80°$), snap-off is inhibited and water in the corners collapsed during PD/WE. Hence, S_{or} monotonically decreases with increasing S_{oi} (at high S_{oi}). Actually, a surprising correlation exists for close-to-intermediate-wet conditions between S_{or} and the water phase connectivity reached following PD/WE (Figure 5.25(b)). In fact, higher S_{oi} following PD/WE (corresponding to higher h) results in a more disconnected water phase due to the "trapping" effect discussed above. As a consequence, less "bypassing" (introduced in 3.2.3(a)) occurs during imbibition in favour of a more efficient microscopic sweep from the inlet. This results in a decrease of S_{or} since the bypassing phenomenon has, to some extent, the same effect as snap-off in reducing the oil phase connectivity.

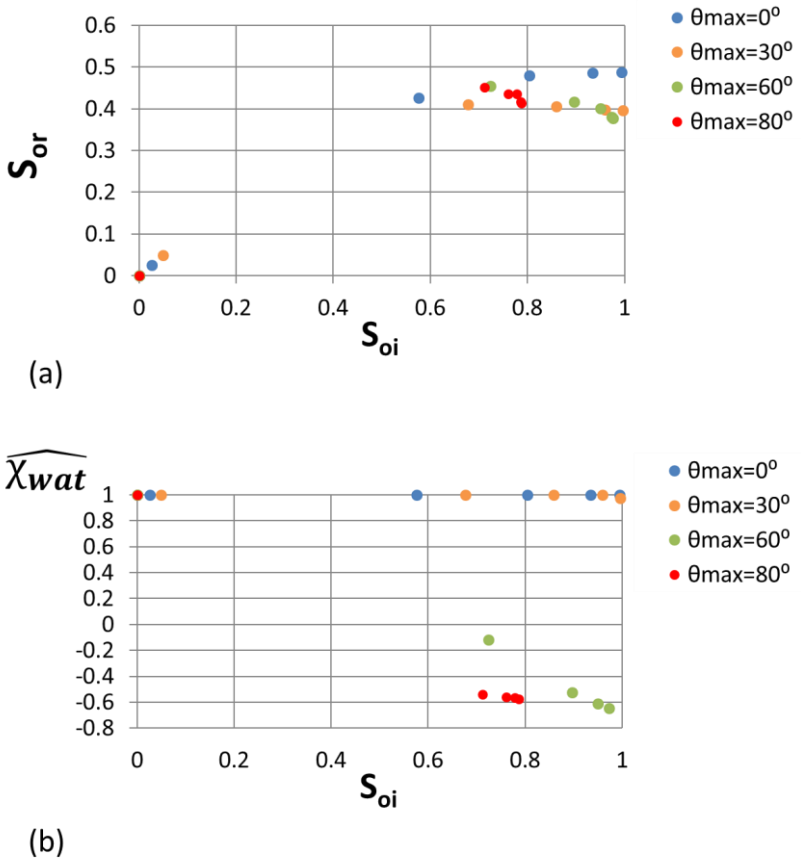

Figure 5.25: Waterflood (a) residual oil saturations and (b) water phase connectivity (normalised Euler number) as a function of S_{oi}, in the Berea network, following the application of the PD/WE model for the base case parameters – with varying height h for the different θ_{max} values – and no subsequent ageing ($f_{ow} = 0$).

With ageing

We assume in this part that a predefined fraction of the pores, f_{ow}, becomes oil-wet following ageing due to the adsorption of heavier hydrocarbon species (e.g. asphaltenes) on the rock surfaces after thin water film collapse by the mechanisms discussed above. To achieve this, we use the physically-based Altered-Wet (AW) distribution introduced in Chapter 3. While we uniformly distribute the oil-wet advancing contact angles, $\theta_{a,ow} \in [120°, 180°]$, we assume that the water-wet advancing contact angles, $\theta_{a,ww}$, do not undergo any further changes after primary drainage.

The resulting wettability distributions and pore occupancies at the end of the waterflood at fixed $h = 3.3m$ for different θ_{max} values are shown in Figure 5.26 and Figure 5.27,

respectively, corresponding to the PD/WE simulations shown in Figure 5.13. Notice that the slight difference in the wettability distributions for the θ_{max} values is mainly due to the difference in the corresponding S_{oi}. While the invasion pattern for $\theta_{max} = 30°$ is similar to the conventional PD case (0°), governed by an equal extent of snap-off and piston-like mechanisms, the pore occupancies at the end of the waterflood at higher θ_{max} are clearly distinct, especially for cases with the switch from 30 to $60°$. Indeed, if the condition in Equation (5.17) is satisfied within a pore, the corner water is expelled if it has an outlet connection, otherwise it remains as trapped cluster. If this pore becomes strongly oil-wet after ageing ($\theta_{a,ow} > \frac{\pi}{2} + \gamma$), oil films are created in the corners following water invasion as shown in Figure 5.27(c) and (d). These are easier to form, i.e. more abundant, than the oil layers that are sandwiched between water in the corner and bulk (Section 3.2.4(c)). The latter are only conditionally stable according to a strict thermodynamic criterion (refer to Section 3.2.3(d)). Additionally, same as for the oil layers, these oil films in the corners significantly contribute in maintaining the oil phase connectivity, hence in reducing S_{or}. In fact, as shown in Figure 5.28, S_{or} is monotonically decreasing with higher θ_{max} due to the increasing occurrence of corner oil films.

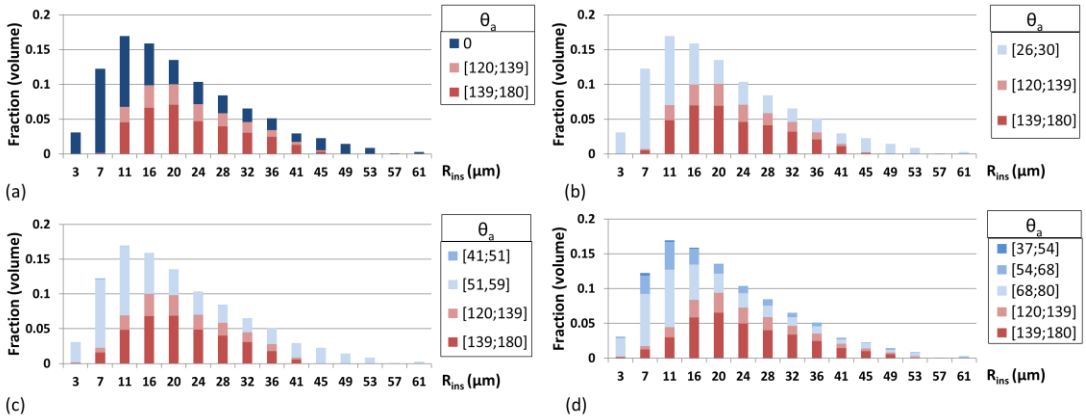

Figure 5.26: Wettability distribution (AW at $f_{ow} = 0.5$) after PD/WE for the base case parameters – with (a) $\theta_{max} = 0°$, (b) $\theta_{max} = 30°$, (c) $\theta_{max} = 60°$ and (b) $\theta_{max} = 80°$, shown on the pore size distribution for the Berea network.

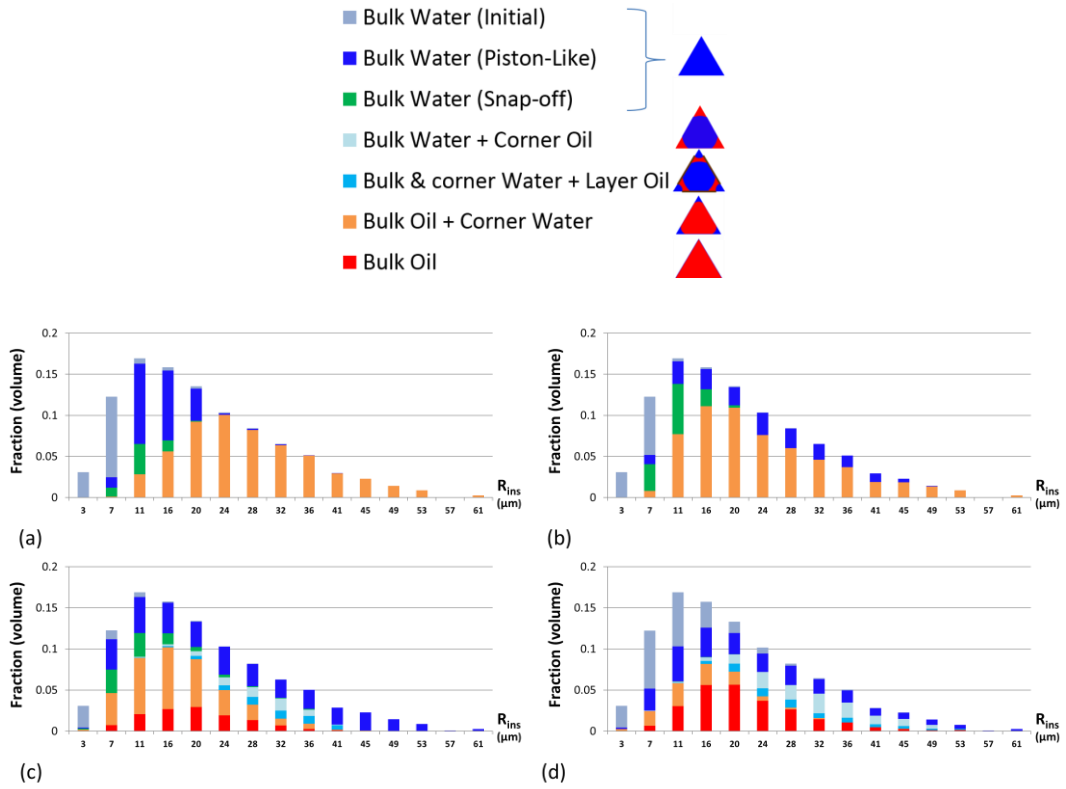

Figure 5.27: Pore occupancies at the end of the waterflood after PD/WE for the base case parameters – with (a) $\theta_{max} = 0°$*(*$S_{oi} = 0.8; S_{or} = 0.54$*), (b)* $\theta_{max} = 30°$ *(*$S_{oi} = 0.86; S_{or} = 0.55$*), (c)* $\theta_{max} = 60°$ *(*$S_{oi} = 0.95; S_{or} = 0.44$*) and (b)* $\theta_{max} = 80°$ *(*$S_{oi} = 0.78; S_{or} = 0.36$*), shown on the pore size distribution for the Berea network (AW distribution at* $f_{ow} = 0.5$*). Note the colour key (top) for the various pore-level displacements.*

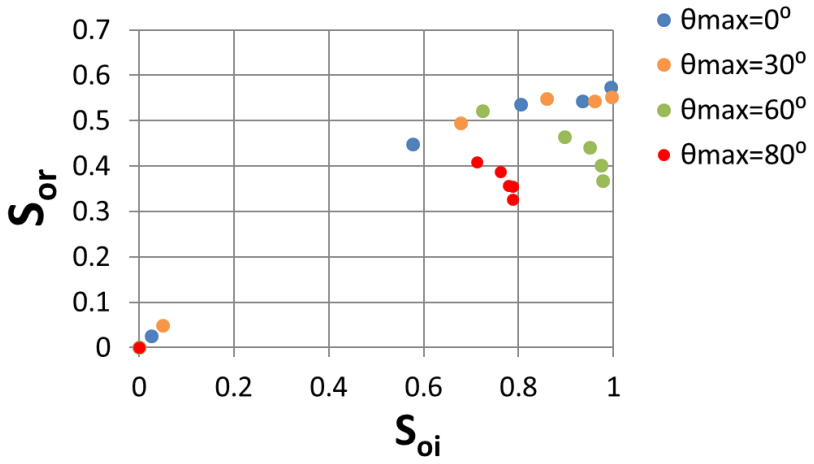

Figure 5.28: Waterflood residual oil saturations in the Berea network as a function of S_{oi} *following the PD/WE model for the base case parameters – with varying height* h *for the different* θ_{max} *values – and subsequent ageing (AW distribution at* $f_{ow} = 0.5$*).*

c) Summary

PD/WE

Upon application of the developed PD/WE model on the Berea network, we reproduced experimental patterns where an early wettability alteration occurs *during* primary drainage, starting from the inlet, due to the adsorption of small polar compounds from the oil phase. Additionally, we obtained clear differences in the PD behaviour, both at the pore-level and in the oil column. The model particularly controlled the initial water saturation, S_{wi}, through two main parameters: (i) the level of wettability alteration (i.e. the pre-defined maximum contact angle, $\theta_{\max}$) and (ii) the balance between the oil invasion and wettability alteration processes (i.e. the system adsorptive capacity, Γ_{max}), as follows:

- Intermediate-wet conditions ($\theta_{max} = 80°$): S_{wi} monotonically decreased with faster oil invasion relative to wettability alteration i.e. higher Γ_{max}.
- Weakly water-wet conditions ($\theta_{max} = 60°$): while the overall pattern was like the $80°$ case, S_{wi} was significantly lower all along the oil column.
- Water-wet conditions ($\theta_{max} = 30°$): S_{wi} was not sensitive to Γ_{max} and was lower all along the oil column compared to the conventional PD curve ($\theta_{max} = 0°$).

Subsequent waterflood

We assessed the oil recovery behaviour by carrying out a waterflood subsequent to the PD/WE model. The residual oil saturation, S_{or}, value strongly depended whether a further wettability alteration from water-wet/intermediate-wet to oil-wet conditions was carried out during ageing. It was also dependent on the final fluid saturations and configuration and the maximum contact angle (θ_{max}), all of which reached following PD/WE, as explained below:

- No ageing:
    - Water-wet conditions ($\theta_{max} = 30°$): S_{or} decreased significantly compared to the conventional PD, especially at high S_{oi}, due to considerably fewer snap-off displacements.

- Closer to intermediate-wet conditions ($\theta_{max} = 60°$ and $80°$): S_{or} monotonically decreased with increasing S_{oi} at high S_{oi}, due to a decreasing water phase connectivity attained following PD/WE.

- With ageing:
  - Water-wet conditions ($\theta_{max} = 30°$): S_{or} was similar to that for the standard PD, where snap-off and piston-like displacements were equally important.
  - Closer to intermediate-wet conditions ($\theta_{max} = 60°$ and $80°$): S_{or} monotonically decreased with higher θ_{max}, due to the increasing occurrence of corner oil films.

Generally, the PD/WE model led to lower oil saturations in the subsequent waterflood. The decrease in S_{or} was particularly significant when the wettability was altered from close to intermediate-wet conditions ($\theta_{max} = 60°$ and $80°$) to oil-wet conditions during ageing.

5.3.2 Carbonate network

In this section, we consider calculations of the type presented above, but now on the more complex multi-scale carbonate network presented in Section 3.3.2. The base case parameters are summarised in Table 5.2. Again, the chosen β, K, P and C_0 correspond to $\theta_{max} = 80°$ (Equation (5.16)). Note that we chose the P_c^{max} base case value for the carbonate network to be significantly higher than that for the Berea network. Indeed, the carbonate network has far smaller pores, thus requires higher capillary pressures to achieve water saturations comparable to those presented for the Berea network. The Γ_{max} base case value was slightly adjusted accordingly.

$Q\ [^{m^3}/_{s}]$	5e-13
$C_0\ [^{mg}/_{L}]$	500
$\Delta_t^{TR}[s]$	0.007
P	0.01
$D\ [^{cm^2}/_{s}]$	1e-5
$K\ [^{L}/_{mg}]$	1
$\Gamma_{max}[^{mg}/_{m^2}]$	0.47
β	0.0083
$P_c^{max}\ [kPa]$	11713

Table 5.2: Base case parameters for Scenario 2 simulations in the carbonate network. Only the last three parameters are varied during the sensitivity study.

a) Primary Drainage

Effect of θ_{max} on S_{wi}

The pore occupancies shown on the pore-size distribution after the application of PD/WE at different θ_{max} are shown in Figure 5.29. The PD/WE model at higher θ_{max} enables the oil to reach higher saturations and to invade smaller pores. In particular, it allows oil migration into micropores (first bin of the PSD) for high enough θ_{max} (60 and $80°$). Indeed, these micropores were not accessible otherwise ($\theta_{max} < 60°$) at the same fixed P_c^{max}. As shown in Figure 5.30(a), the filling of micropores at $\theta_{max} = 80°$ occurred early in the process at S_w lower than 0.5, which coincides with S_{wi} for the conventional PD (Figure 5.29(a)). Indeed, at the same water saturation, the filling pattern when applying PD/WE at intermediate-wet conditions compared to the conventional PD is different as the oil invasion is more spread over the PSD. This is due to the dramatic decrease in entry pressures following the increase in contact angles from $0°$ to $\theta_{max} = 80°$ (Figure 5.30(b)), which changes the filling sequence to become less dependent on pore size and more linked to the adsorption level of polar compounds and the resulting wettability alteration.

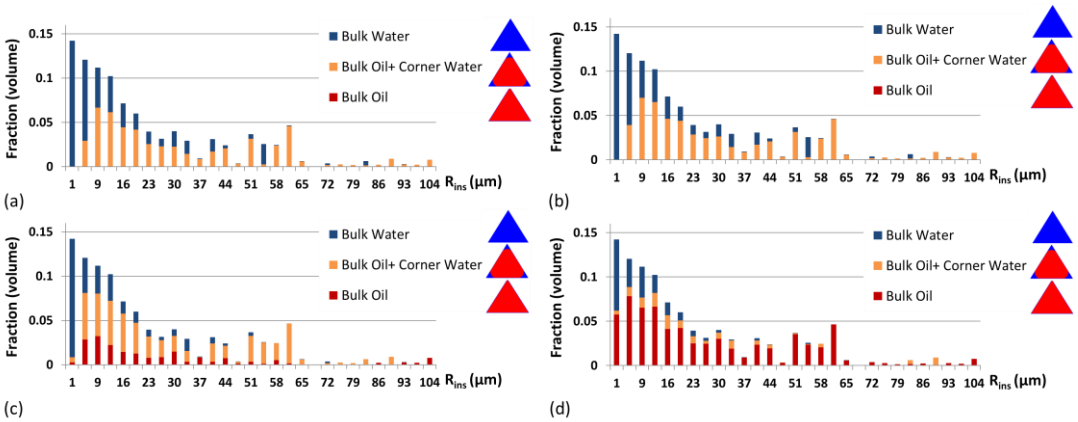

Figure 5.29: Pore occupancies for the carbonate network shown on the pore-size distribution following PD/WE for the base case parameters – with (a) $\theta_{max} = 0°$ ($S_{wi} = 0.5$); (b) $\theta_{max} = 30°$ ($S_{wi} = 0.46$); (c) $\theta_{max} = 60°$ ($S_{wi} = 0.32$) and (d) $\theta_{max} = 80°$ ($S_{wi} = 0.22$).

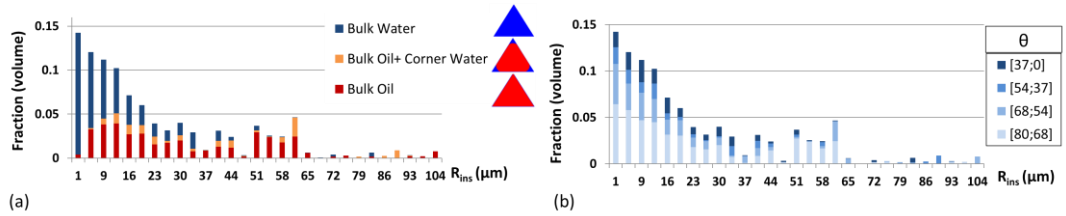

Figure 5.30: (a) Pore occupancies and (b) wettability alteration for the carbonate network shown on the pore-size distribution following PD/WE for the base case parameters stopped at a predefined $S_w = 0.5$.

Effect of Γ_{max} on S_{wi}

In this part, we keep θ_{max} as the base case value (80°) and alter the balance between the processes of wetting change and oil invasion by changing Γ_{max}. The pore occupancies shown on the pore-size distribution in Figure 5.31, added to the information from Figure 5.29(d) ($\Gamma_{max} = 0.47$), confirm the earlier findings that a slower wetting change relative to oil invasion at intermediate-wet conditions results in monotonically decreasing S_{wi} at the same predefined P_c^{max}. Besides, according to Figure 5.32(b), although the wettability alteration was delayed for a higher Γ_{max} (compared to Figure 5.30(b)), the invasion of micropores still occurred at $S_w < 0.5$. Indeed, those invaded micropores experienced enough wettability alteration for their P_E to sufficiently decrease at a relatively early stage. Eventually, oil migrates further into micropores for higher Γ_{max}.

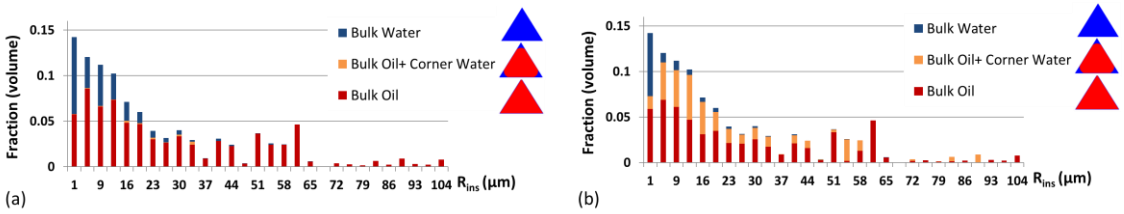

Figure 5.31: Pore occupancies for the carbonate network shown on the pore-size distribution following PD/WE for the base case parameters – with (a) $\Gamma_{max} = 0.1$ *(*$S_{wi} = 0.26$*) and (b)* $\Gamma_{max} = 1.4\ \frac{mg}{m^2}$ *(*$S_{wi} = 0.13$*).*

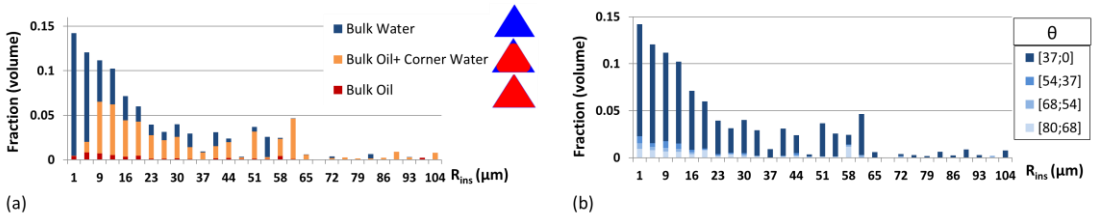

Figure 5.32: (a) Pore occupancies and (b) wettability alteration for the carbonate network shown on the pore-size distribution following PD/WE at $\Gamma_{max} = 1.4\ \frac{mg}{m^2}$ *and* $\theta_{max} = 80°$*, stopped at a predefined* $S_w = 0.5$*.*

Combined effect of θ_{max} and Γ_{max} on S_{wi}

We summarise the combined effects of θ_{max} and Γ_{max} on S_{wi} at fixed P_c^{max} in Figure 5.33. The results are qualitatively similar to those for the Berea network (Figure 5.19). However, the dependency of S_{wi} on the balance between the oil invasion and wettability alteration processes at fixed θ_{max} is weaker for the carbonate network because the "trapping" effect is less significant. In fact, as demonstrated in Figure 5.34, the decrease in the water phase connectivity, $\widehat{\chi_{wat}}$, is slower for the carbonate network at the same conditions. This pattern is attributed to the particular topology of the multiscale carbonate network where the microporosity joins up the otherwise disconnected larger pores. Indeed, the largest pores are generally invaded first during PD, and many lose their corner water generating a loss in the water phase connectivity. However, because their contribution to the overall network connectivity is low, water remains largely connected early on, leading eventually to lower S_{wi}.

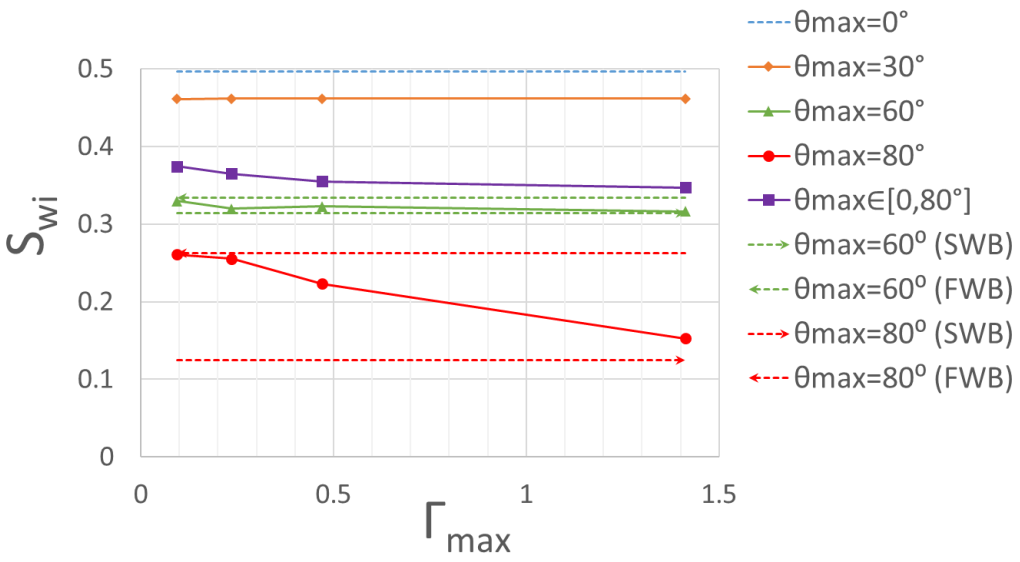

Figure 5.33: The resulting S_{wi} as a function of Γ_{max} $[\frac{mg}{m^2}]$ following the PD/WE model in the carbonate network for the base case parameters – with different θ_{max} values. FWB and SWB are the limiting fast wetting and slow wetting boundaries, respectively.

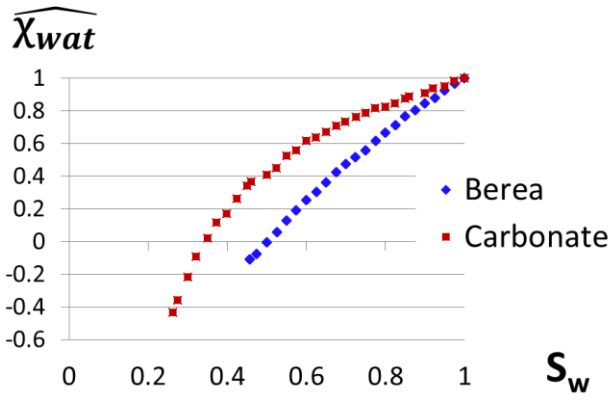

Figure 5.34: Comparison between the Berea and carbonate networks' evolution of the water phase connectivity (normalised Euler number) during PD/WE at $\theta_{max} = 80°$ at the highest point in the oil column for the fast wetting boundary (FWB) limiting case.

Similar to the analysis provided in Figure 5.33, we now quantitatively assess the invasion of micropores in the carbonate network following the PD/WE model, as shown in Figure 5.35. The results clearly show that the invasion of micropores at the (base case) moderate P_c^{max} occurs at intermediate-wet conditions ($\theta_{max} = 60°$ and $\theta_{max} = 80°$). Additionally, for $\theta_{max} = 80°$, the oil is driven further into micropores for higher Γ_{max}, as expected.

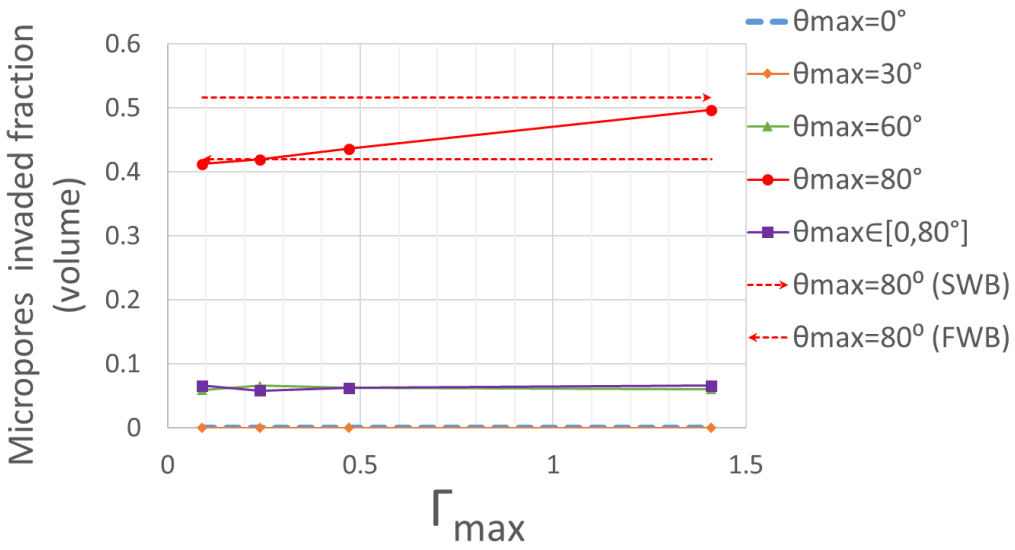

Figure 5.35: The resulting (volumetric) fraction of micropores invaded by oil as a function of Γ_{max} $[\frac{mg}{m^2}]$ following the PD/WE model in the carbonate network for the base case parameters – with different θ_{max} values. FWB and SWB are the limiting fast wetting and slow wetting boundaries, respectively.

More generally, by varying P_c^{max}, we obtain the oil column distributions for the different pairs of parameters $(\theta_{max}, \Gamma_{max})$ in Figure 5.36. Note that $h = 6$ m corresponds to the base case P_c^{max} $(11712\ Pa)$ utilized for all previous simulations. Again, the results of the PD/WE model follow the same qualitative trends exhibited by the Berea network in Figure 5.20, but the gap between the curves at fixed θ_{max} $(60 \text{ or } 80°)$ is narrower since the fast wetting boundary, FWB, is shifted to the left. This is again due to the weaker "trapping" effect.

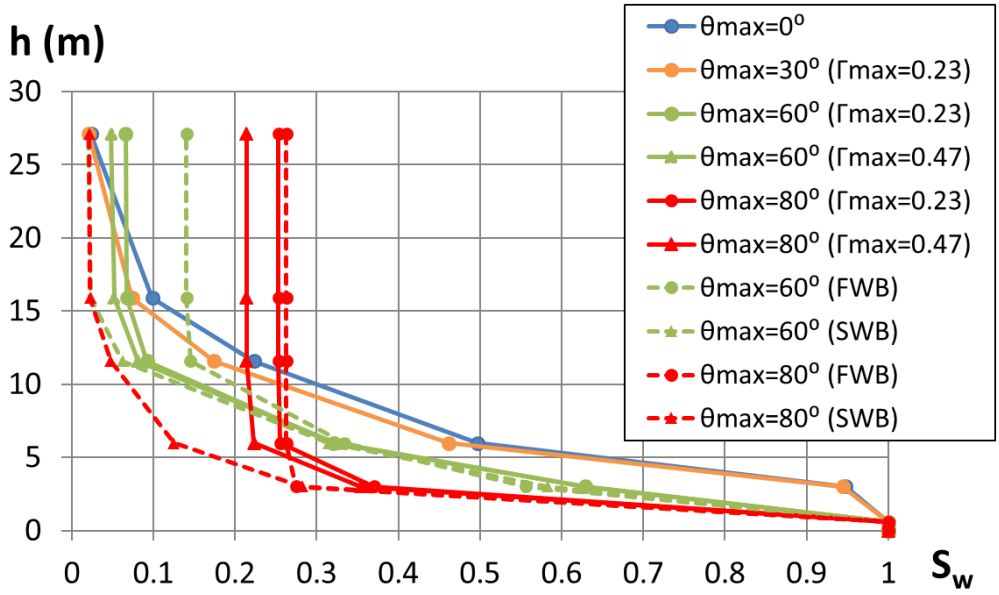

Figure 5.36: Distribution in the oil column in the carbonate network following the PD/WE model for the base case parameters – with different combinations of θ_{max} and $\Gamma_{max}[\frac{mg}{m^2}]$ values. FWB and SWB are the limiting fast wetting and slow wetting boundaries, respectively.

b) Waterflood

<u>No ageing</u>

We simulate waterflood in the carbonate network assuming the only change in wettability happened during PD/WE (θ_{max}). The pore occupancies at the end of the waterflood are shown in Figure 5.37. The water invasion pattern is similar for any chosen θ_{max}. This may be explained by the very limited snap-off for the carbonate network, even at $\theta_{max} = 0°$. It is mainly due to a well-connected fine-scale sub-network where the first water invasions happen, favouring piston-like displacements over snap-off. This results in a dependency of S_{or} on S_{oi} that is highly insensitive to θ_{max} (Figure 5.38(a)), in contrast to the Berea network case. Nonetheless, we still observe the same correlation between S_{or} and $\hat{\chi}_{Wat}$ (reached following PD/WE) for close-to-intermediate-wet conditions at high S_{oi} (Figure 5.38 (a) and (b)).

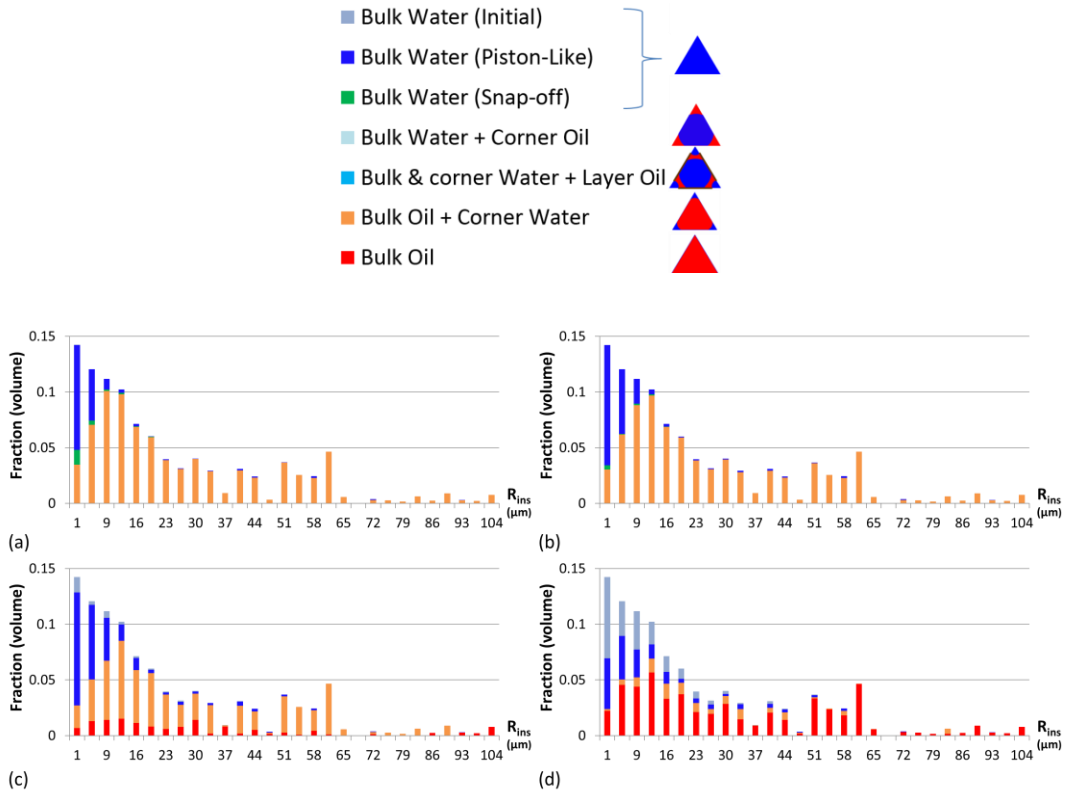

Figure 5.37: Pore occupancies at the end of the waterflood after PD/WE for the base case parameters – at $h = 27m$ and (a) $\theta_{max} = 0°(S_{oi} = 0.98; S_{or} = 0.76)$, (b) $\theta_{max} = 30°$ $(S_{oi} = 0.98; S_{or} = 0.74)$, (c) $\theta_{max} = 60°$ $(S_{oi} = 0.95; S_{or} = 0.7)$ and (b) $\theta_{max} = 80°$ $(S_{oi} = 0.79; S_{or} = 0.63)$, shown on the pore size distribution for the carbonate network (no ageing). Note the colour key (top) for the various pore-level displacements.

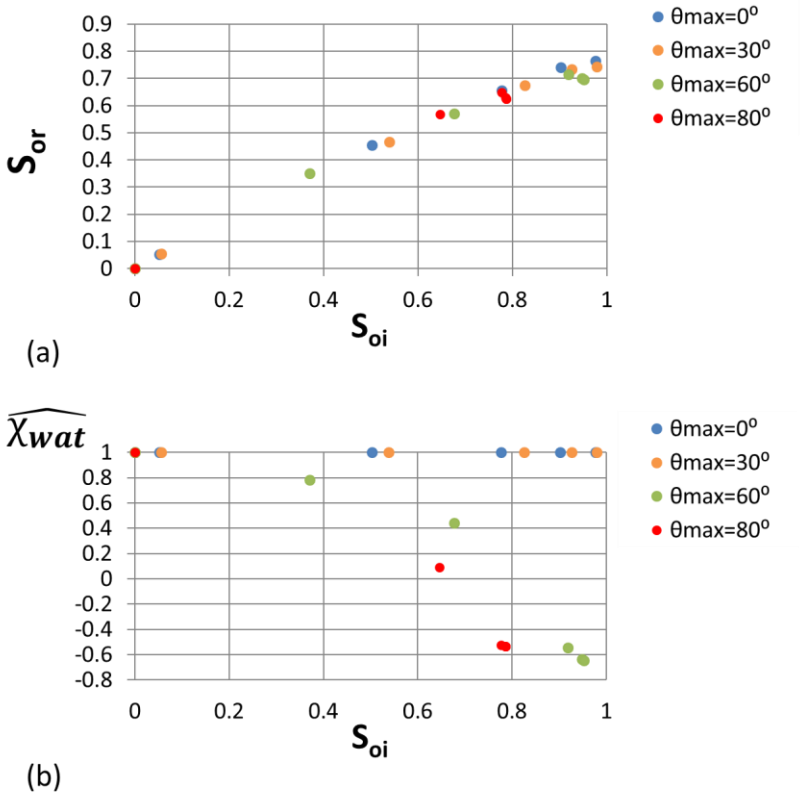

Figure 5.38: Waterflood (a) residual oil saturations and (b) water phase connectivity (normalised Euler number) as a function of S_{oi}, in the carbonate network, following the application of the PD/WE model for the base case parameters – with varying height h for the different θ_{max} values – and no subsequent ageing ($f_{ow} = 0$).

With ageing

In this part, we assume that ageing takes place following the PD/WE model. This process again results in half of the pores becoming oil-wet ($f_{ow} = 0.5$), distributed according to the AW distribution. The wettability distributions in Figure 5.39 show that the oil-filled micropores (defined as the first bin in the pore size distribution) are mostly oil-wet for all cases. This is due to their tiny size that provides enough curvature for the thin films to break (Section 4.3.2(b)). As for the Berea network, the corresponding pore occupancies in Figure 5.40 show a significant amount of corner oil films, as well as some oil layers, created during the waterflood subsequent to PD/WE at high θ_{max}.

The dependency of S_{or} on S_{oi} in Figure 5.41 shows a pattern with a maximum at around $S_{oi} = 0.7$, regardless of θ_{max}. This is ascribed to the particular connectivity structure of the carbonate network being mainly provided by its microporous sub-network, with the

larger macroporous sub-network being disconnected. Indeed, higher S_{oi} means more micropores filled by oil following PD/WE. And because they mostly become oil-wet after ageing according to the AW distribution, they remain filled by water at the end of the waterflood process. This reduces S_{or} as the oil maintains a much better connectivity than the case where water-wet micropores are invaded early on, blocking the escape of oil from the larger pores. Besides, as for the Berea network, S_{or} monotonically decreases with higher θ_{max} due to the increasing amount of the created corner oil films that maintain the oil phase connectivity. Nonetheless, this decrease in S_{or} is stronger in the carbonate network, especially at high S_{oi}.

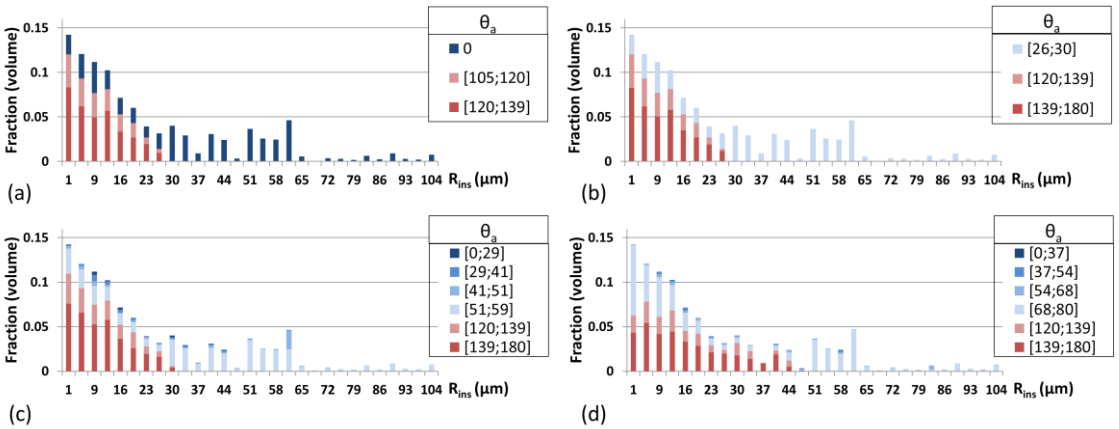

Figure 5.39: Wettability distribution (AW at $f_{ow} = 0.5$) after PD/WE for the base case parameters – at $h = 27m$ and (a) $\theta_{max} = 0°$, (b) $\theta_{max} = 30°$, (c) $\theta_{max} = 60°$ and (b) $\theta_{max} = 80°$, shown on the pore size distribution for the carbonate network.

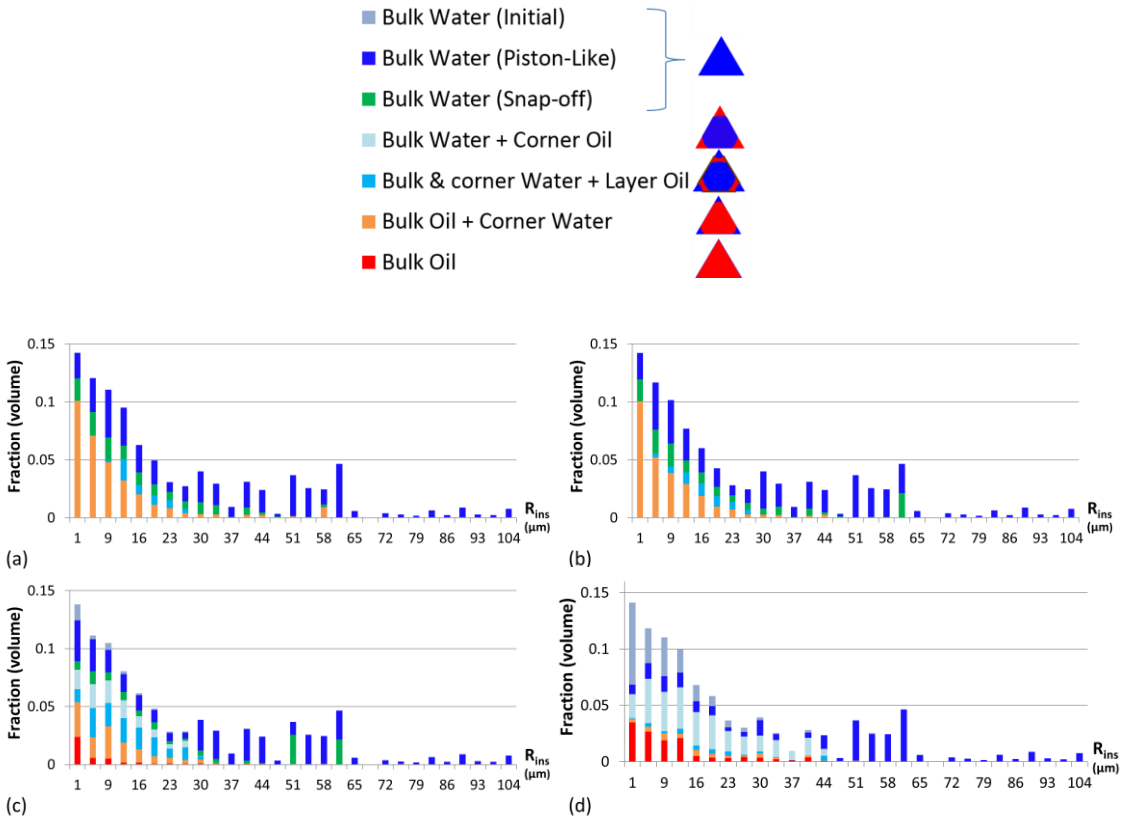

Figure 5.40: Pore occupancies at the end of the waterflood after PD/WE for the base case parameters – at $h = 27m$ and (a) $\theta_{max} = 0°$($S_{oi} = 0.98; S_{or} = 0.3$), (b) $\theta_{max} = 30°$ ($S_{oi} = 0.98; S_{or} = 0.26$), (c) $\theta_{max} = 60°$ ($S_{oi} = 0.95; S_{or} = 0.17$) and (b) $\theta_{max} = 80°$ ($S_{oi} = 0.79; S_{or} = 0.17$) , shown on the pore size distribution for the carbonate network (AW distribution at $f_{ow} = 0.5$). Note the colour key (top) for the various pore-level displacements.

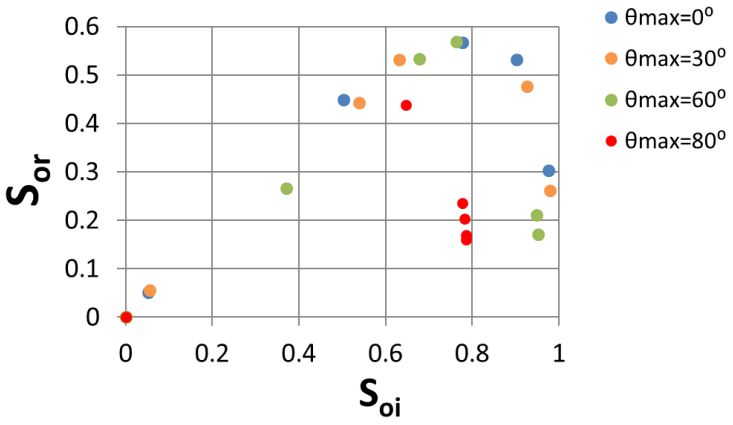

Figure 5.41: Waterflood residual oil saturations in the carbonate network as a function of S_{oi} following the PD/WE model for the base case parameters – with varying height h for the different θ_{max} values – and subsequent ageing (AW distribution at $f_{ow} = 0.5$).

However, note that by maintaining $f_{ow} = 0.5$ constant for each pair of parameters (θ_{max}, h) which result in a single S_{oi} value in Figure 5.41, Π_{crit} is changing (refer to 5.2.3(a)). Similar to the discussion in Section 4.3.2(c), this may not be true since Π_{crit} is supposed to be an intrinsic property of the rock mineral and the water film. This suggests that Π_{crit} should be fixed as a constant, for instance equal to $33kPa$ (that corresponds to $f_{ow} = 0.5$ at $\theta_{max} = 40°$). Figure 5.42 explains the dependency of f_{ow} on both θ_{max} and h for the chosen Π_{crit}. It clearly shows, as expected, that f_{ow} increases with higher θ_{max} since water films get more destabilised i.e. P_c^* decreases in accordance with Equation (5.18). Additionally, f_{ow} increases higher in the oil column (higher h) since at higher P_c^{max} (i) more films are prone to collapse and (ii) higher oil saturations are reached.

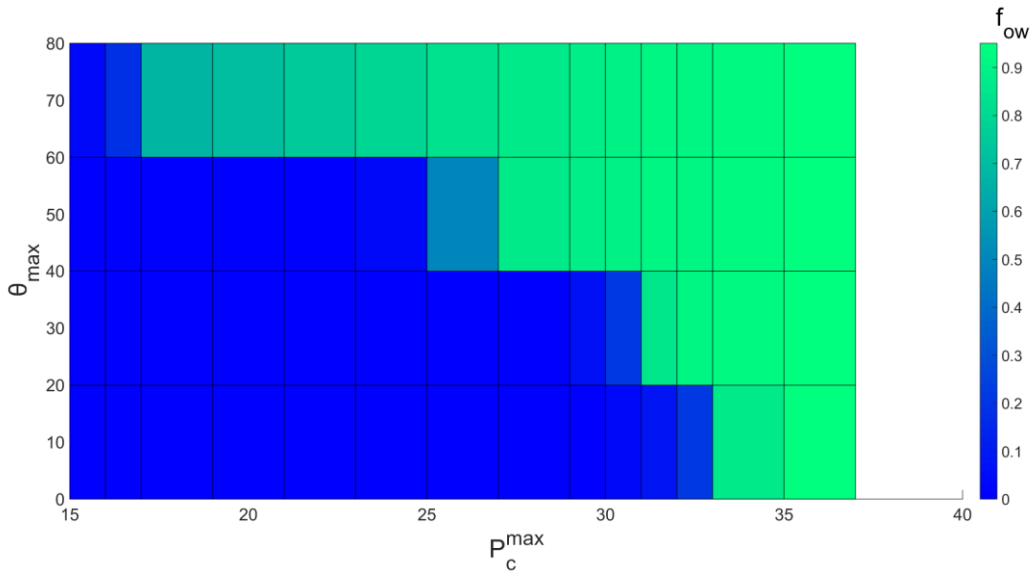

Figure 5.42: Contour chart describing the relationship between θ_{max}, h and f_{ow} at a chosen $\Pi_{crit} = 33kPa$ (for which $f_{ow} = 0.5$ at $\theta_{max} = 40°$).

c) Summary

PD/WE

Upon application of the PD/WE model, the carbonate network exhibited overall trends qualitatively similar to the Berea network, both at the pore-scale and the reservoir-scale (oil column). Nonetheless, the "trapping" i.e. loss in water phase connectivity due to the collapse of corner water, was less effective due to the carbonate network connectivity governed by its microporosity. This resulted in the dependency of the initial water saturation, S_{wi}, on the balance between the oil invasion and wettability alteration

processes being weaker for the carbonate network, with lower S_{wi} all along the oil column. Additionally, we clearly demonstrated how initially strongly water-wet micropores, inaccessible with regards to their high initial capillary entry level, can be invaded early in the primary drainage process as a result of a wetting change to intermediate-wet conditions.

Subsequent waterflood

As for the Berea network, the residual oil saturation, S_{or}, upon waterflooding the carbonate network strongly depended on whether a subsequent wettability alteration from water-wet/intermediate-wet to oil-wet conditions was applied (ageing) following PD/WE. Nonetheless, a few differences arose, mainly attributed to the difference in topology:

- No ageing:

  S_{or} was weakly sensitive to the contact angle change. The main cause is the absence of snap-off displacements in favour of more regular piston-like displacements, probably due to a well-connected microporosity.

- With ageing:

  The carbonate network S_{or} decreased more dramatically compared to the Berea network, especially at high S_{oi} when micropores are filled by oil and are mainly oil-wet in accordance with the Altered-Wet distribution. This is ascribed to the particular connectivity of the network controlled by its microporosity.

5.4 Conclusions

In this chapter, we have developed a novel pore-scale model where the wetting state evolves *during* primary drainage, referred to as the Primary Drainage/Wettability Evolution (PD/WE) model. The model involves small polar species from the oleic phase with high solubility in water and important surface activity (e.g. alkylphenols, carbazoles, etc.). The PD/WE model qualitatively reproduced experimental observations reported by Bennett et al. (2004) where an early rapid wettability alteration occurred during primary drainage, starting from the inlet, due to the adsorption of these polar species.

The PD/WE model is proposed as a physically well-founded *plausible* model using all the pore-scale physics of fluid displacements and wetting alteration that we currently

understand. We are applying this to generate understanding and explanations of how the complex range of parameters interact in the primary drainage and wetting change process that occur when crude oil invades a porous rock. The possible fluid configurations and wetting states that can occur and how these give rise to the post-drainage oil column are considered and explained. Furthermore, we also intended to show that it is straightforward for oil to invade small water-filled, initially water-wet pores with both reasonable and minimal physics-based assumptions. This final stage of altered wettability and fluid configurations following PD/WE models forms the initial state for the ageing and subsequent water displacement (imbibition) to determine the oil recovery characteristics of pore networks. A flowchart describing the interactions between the different processes modelled as part of this chapter is shown in Figure 5.43.

PD/WE

Upon the application of the wettability alteration model, we highlighted that two effects were competing to determine the water saturation following primary drainage, S_{wi}, at fixed maximum capillary pressure, P_c^{max}:

- "Trapping": loss in water phase connectivity due to corner water removal following the wettability alteration in oil-filled pores, which tends to increase S_{wi}. Compared to the Berea network, this effect was generally weaker in the carbonate network due to its singular connectivity dominated by its microporosity.
- "Enterability": decrease in pore entry pressure P_{entry} following the wetting change of water-filled pores, which tends to decrease S_{wi}.

Interestingly, we invoked clear differences in the PD behaviour by varying both the level of wettability alteration (through the imposed maximum contact angle reached, $\theta_{\max}$) and the balance between the oil invasion and wetting change processes (through the system adsorptive capacity, Γ_{max}). These two parameters proved to dictate S_{wi} following PD/WE as they vary the competition between "trapping and "enterability" as follows:

- For intermediate-wet conditions ($\theta_{max} = 80°$), where both the "trapping" and "enterability" effects are significantly strong, S_{wi} monotonically decreased with faster oil invasion relative to wetting change (higher Γ_{max}) due to the resulting

delay in "trapping". In fact, depending on Γ_{max}, the model may end up with either lower or significantly higher S_{wi} throughout the oil column compared to the conventional PD simulation. This change in S_{wi} was less dramatic for the carbonate network than for the Berea network because of the "trapping" being weaker in the former.

- For weakly water-wet conditions ($\theta_{max} = 60°$), although the behaviour was similar to the $80°$ case, S_{wi} was generally lower. In fact, while both the "enterability" and "trapping" effects get weaker with lower contact angle, the loss in "enterability" is compensated by a stronger decrease in "trapping", meaning that the former generally dominates.
- For water-wet conditions ($\theta_{max} = 30°$) where "enterability" dominates in the absence of "trapping", S_{wi} was independent of Γ_{max} and was lower all along the oil column compared to the conventional PD.

Note that neither the change in the way the balance between the oil invasion and wettability alteration processes is varied nor the change in the time-dependent oil invasion model has an effect on the PD/WE model qualitative behaviour.

The PD/WE model provides a physically-plausible scenario to explain the phenomenon of oil invasion into micropores. Indeed, we demonstrated that oil did invade the micropores at moderate capillary pressure values following their wetting alteration. In fact, these micropores were not accessible otherwise following the conventional PD at the same fixed P_c^{max}. This process is further illustrated in Figure 5.44.

Subsequent waterflood

In this chapter, we also carried out waterflood simulations following the application of the PD/WE model. The resulting S_{or} patterns changed significantly, depending whether a further wettability alteration from water-wet/intermediate-wet to oil-wet conditions during ageing applied. S_{or} proved as well to be sensitive to the initial fluid saturations and configuration, the extent of wettability alteration during PD/WE (θ_{max}) and the network topology, as follows:

- No ageing:
    - For water-wet conditions ($\theta_{max} = 30°$), S_{or} was significantly lower than the conventional PD in the Berea network, especially at high S_{oi} where

a plateau was reached. This is mainly due to the occurrence of far fewer snap-off events. However, the carbonate network lack of snap-off in favour of more regular piston-like displacements due to a well-connected microporosity resulted in S_{or} being weakly sensitive to the contact angle change.

- For closer to intermediate-wet conditions ($\theta_{max} = 60°$ and $80°$), in the absence of snap-off and at which some corner-water collapsed during PD/WE, S_{or} monotonically decreased with increasing S_{oi} at high S_{oi}. This pattern is due to the surprising correlation between S_{or} and the water phase connectivity reached following PD/WE. Indeed, higher S_{oi} generates a less connected water phase due to "trapping". This, in turn results in less frequent "bypassing" in favour of a more efficient sweep from the inlet, which better maintains the oil phase connectivity thus reduces S_{or}.

- With ageing:
  - For water-wet conditions ($\theta_{max} = 30°$), the waterflood behaviour was like the conventional PD case, controlled to an equal extent by both snap-off and piston-like displacements.
  - For closer to intermediate-wet conditions ($\theta_{max} = 60°$ and $80°$), S_{or} monotonically decreased with higher θ_{max}, due to the creation of oil layers and the more abundant corner films. In fact, the latter, created during waterflood in pores whose corner water was expelled during PD/WE and that became strongly oil-wet after ageing, are easier to form than the oil layers that are only conditionally stable according to a strict thermodynamic criterion. Both equally contribute in maintaining the oil phase connectivity, hence in significantly reducing S_{or}. This decrease in S_{or} was significantly higher for the carbonate network compared to the Berea network, especially at high S_{oi} when micropores are oil-filled and largely oil-wet according to the Altered-Wet distribution.

In general terms, the PD/WE model resulted in substantially lower S_{or} subsequent to waterflood, especially when the wetting state was changed from close to intermediate-wet conditions ($\theta_{max} = 60°$ and $80°$) to oil-wet conditions during ageing. This was particularly significant for the carbonate network, especially at high S_{oi} when

micropores are invaded by oil and mostly oil-wet in accordance with the physically-based Altered-Wet distribution. This is attributed to the connectivity characteristics of the carbonate network where the microporosity joins up an otherwise disconnected network.

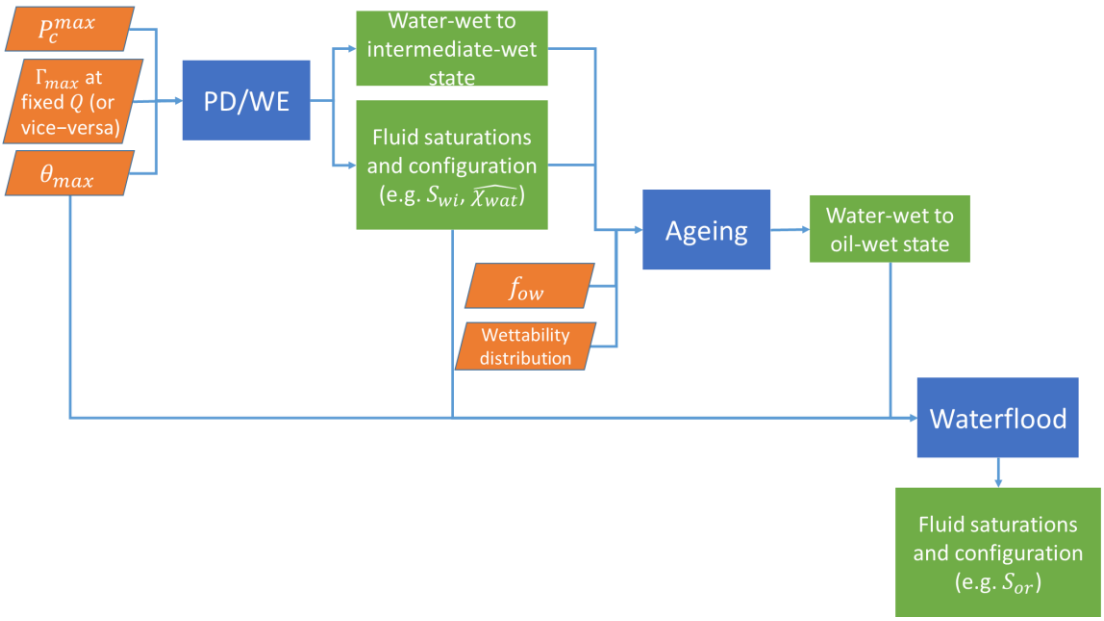

Figure 5.43: Flowchart describing the complex interaction between the input parameters (in orange), the modelled processes (PD/WE, Ageing and Waterflood, in blue) and their output results (in green).

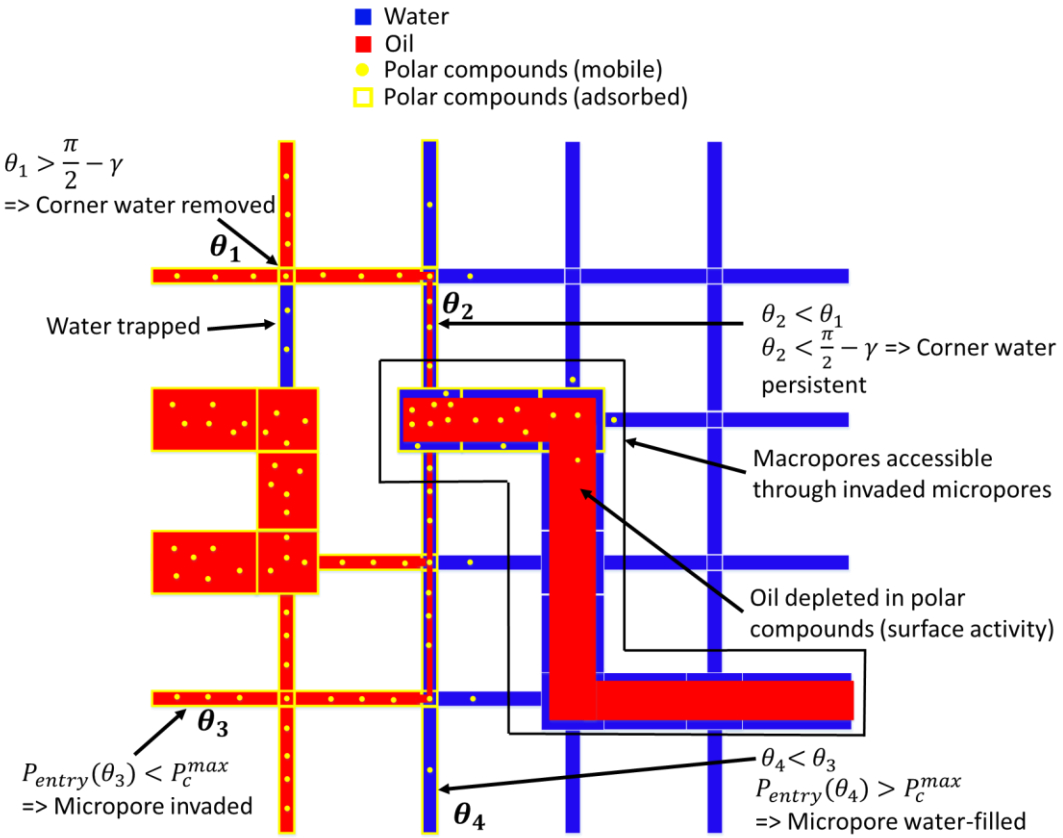

Figure 5.44: Representation of the PD/WE model and its effects on oil invasion by a snap-shot of a simplified 2D 4x4 carbonate network of pores with square cross-sections (half-angle γ) and two distinct pore sizes: small micropores joining up disconnected larger macropores. Note that periodic boundary conditions apply between the bottom and top. The network is initially water-filled and perfectly water-wet (initial contact angle $\theta = 0°$), then oil displaces water from the inlet (left) to the outlet (right). For simplicity, we assume that only the macropores can be invaded at the initial wetting conditions and at the chosen (low) predefined maximum capillary pressure, P_c^{max}. Note that $P_{entry}(\theta)$ of a water-filled pore corresponds to its entry pressure at θ.

Chapter 6 : Conclusions and future work

6.1 Summary and main conclusions

In this work, we aimed at modelling the wettability alteration in microporous carbonate rocks at the pore-scale. To do so, we investigated the responses of different petrophysical properties to two distinct scenarios for wettability change:

- Scenario 1: the wettability change occurs *following* primary drainage as a result of ageing in crude oil. This corresponds to the traditional approach that mimics the 3-stage process experienced by an initially water-wet reservoir: primary drainage, ageing and waterflood.
- Scenario 2: an alternative framework where the wettability alteration from initially water-wet to more intermediate-wet conditions occurs *during* primary drainage. A subsequent wettability alteration to oil-wet conditions may then take place during ageing.

6.1.1 Scenario 1- Wettability alteration following ageing

What has been done

Within Scenario 1, we have developed a physically-based wettability distribution, referred to as Altered-Wet (AW), which takes into account the shapes of the pores as well as their size. We implemented it in a two-phase flow pore network model and used a simple model that assigns equivalent curvatures to the flat pore walls based on the overall pore shapes (for wettability alteration purposes only). The AW scenario represents an alternative to the standard wettability distributions, either exclusively correlated to pore size: Mixed-Wet Large (MWL) and Mixed-Wet Small (MWS); or distributed independently of pore size: Fractionally-Wet (FW).

Novelty

This model is based on Kovscek et al. (1993)'s work, which has already been implemented in 3D pore network models by many authors (Blunt, 1997, Blunt, 1998, Oren et al., 1998, Jackson et al., 2003). However, these studies used angular pore cross sections, and a simple parametric model for the water film collapse, assigned randomly, which may end up in the Fractionally-Wet (FW) distribution. Moreover, to our knowledge, neither the derived wettability distribution nor the resulting residual oil

saturation following waterflood have been previously compared to those corresponding to the standard wettability distributions.

Main conclusions

- The AW model qualitatively reproduced a pattern of wettability alteration in carbonates shown experimentally by high-resolution imaging, where the most curved pore walls are the most likely to be oil-wet.
- The AW distribution was different from any of the standard wettability distributions (MWL, MWS, FW). Particularly in the carbonate network, although it led to mostly oil-wet micropores due to their very small sizes (which provide enough curvature for the water films to collapse), the wetting distribution was still clearly distinct from the MWS model.
- The sandstone network showed little sensitivity to different wettability scenarios with regard to the residual oil saturation.
- The microporous carbonate network exhibited a significant effect of the wettability distributions on the residual oil saturation.
- We demonstrated the importance of the micropores' wettability on flow in carbonates, which proved to control the oil recovery.

6.1.2 Scenario 2- Wettability alteration starting during primary drainage

What has been done

Within Scenario 2, based on experimental observations by Bennett et al. (2004), we developed a physically plausible wettability alteration model that occurs during primary drainage. The model, implemented in a two-phase flow pore network model, involves the relatively rapid adsorption of surface-active water-soluble polar compounds (such as phenols, carbazoles, etc.) present in the oleic phase. This then leads to a destabilisation of the water films (by reducing the disjoining pressure) leading to wetting alteration by the subsequent adsorption of higher molecular weight hydrocarbon species (e.g. asphaltenes).

Novelty

This model proposes a novel scenario that tackles the issue of oil migration into micropores by associating it to a wettability change that evolves during primary drainage (PD). Moreover, the approach itself is original since we overcame the time-

independency inherited from “quasi-static” pore network models by adding a notional time-dependency to the conventional oil invasion in order to incorporate a dynamic transport model for polar compounds. However, although the model is based on experimental evidence, we believe that it is not yet at a predictive stage, but rather an explanative model based on reasonable assumptions.

Main conclusions

- The model qualitatively reproduced experimental observations where an early rapid wettability alteration occurred during primary drainage, starting from the inlet, due to the polar compounds surface interaction that decreased in the direction of flow.
- We invoked clear differences in the primary drainage patterns by varying the level of wettability alteration and the balance between the oil invasion and wetting change processes. In fact, these two parameters proved to dictate S_{wi}.
- For the particular conditions of relatively fast oil invasion or small wetting changes, the model leads to lower S_{wi} at fixed P_c^{max} compared to the conventional primary drainage model. Particularly in the microporous carbonate network, this results in the invasion of micropores at reasonable (low) capillary pressures.
- The model resulted in significant decrease in the residual oil saturations, S_{or}, following subsequent waterflood, compared to the conventional PD. This improvement in oil recovery was especially significant when an additional wettability alteration from intermediate-wet to oil-wet conditions applies during ageing.

6.2 Discussion

- Although the two scenarios developed in the course of this study particularly served our purpose in reproducing experimental wettability alteration trends observed in microporous carbonates and in providing a possible explanation of micropores invasion, they apply regardless of the rock type. The only parameter that needs to be modified when changing from a rock to another would be the critical disjoining pressure, which is for instance lower for carbonates than for sandstones.

- The transport model incorporated in Scenario 2 added a significant complexity to the conventional quasi-static pore network modelling tool. Hence, the computation times (shown in Table 6.1) have considerably increased. Nonetheless, they are still within a reasonable time-scale of a few hours in our case, which can be improved by a more powerful computer. This computational complexity is mainly attributed to the discretised diffusion model that requires small diffusion time-steps in order to conserve mass properly (see Equation (5.9)). Since this constraint is imposed by the smallest pores, the wider is the pore-size distribution, the slower is the simulation. This explains the higher computational time for the carbonate network whose pore sizes span multiple length-scales, as compared to the Berea network with comparable number of pores. Consequently, we expect that complex multi-scale rocks will require larger networks to produce reliable quantitative predictions.

	Scenario 1	Scenario 2
Berea network	$t = 36s$	$t = 53s$
Carbonate network	$t = 17994s$	$t = 32986s$

Table 6.1: Typical computational times for the two developed scenarios run on the Berea and carbonate networks using the base case parameters (shown in Table 4.1, Table 5.1 and Table 5.2). Note that the computer has an Intel core i7 processor, and that multiple simulations can be run simultaneously without altering the computational efficiency

- We attempted to run our simulations on a different multiscale carbonate network with significant microporosity and where the macropores are (just) intra-connected. However, we were not able to identify a suitable network. Most of the multiscale networks that we generated lacked the overall connectivity to allow the waterflood to reach reasonable residual oil saturations (lower than 1). The reason possibly resides in the shortcomings of multiscale network extraction techniques that fail to properly join the networks at two distinct length-scales.

6.3 Future work

We acknowledge that the models that we developed in the scope of this thesis have shortcomings and issues that need to be addressed and require further improvements, such as:

- Within the framework of Scenario 1:
    - Implement Grain Boundary Pore (GBP) cross-sectional shapes (Man and Jing, 2000) within the pore network model instead of assigning equivalent curvatures to flat pore shapes.
    - Better characterise the micropores shapes, for instance capture the distinctive straight and platy morphology of micropores (Cantrell and Hagerty, 1999).
    - Consider a wider dataset of carbonate networks as inputs to the model to support the findings.

- Within the framework of Scenario 2:
    - We implemented a simple transport model that sufficiently captured some interesting primary drainage patterns. However, we suggest the implementation of more sophisticated chemical and physical details into the diffusion, adsorption and subsequent wettability change sub-models. For instance, does the Langmuir isotherm for equilibrium adsorption capture the actual adsorption mechanism or should we rather use a kinetic adsorption model instead? Additionally, one can suggest a more complex model for wettability change as a function of adsorption levels instead of the rather simple linear dependency that we proposed.
    - We stretched the capabilities of "quasi-static" network models by adding a notional time-dependency in order to incorporate the transport model. Hence, we suggest to assess the benefit of using a truly "dynamic" pore network model instead. However, this should capture accurately films in the corners as these proved to be central in controlling the resulting residual phase saturations (S_{wi} and S_{or}) in our model. Moreover, dynamic models are computationally very demanding, therefore

benefits of using a dynamic model should be looked at critically, particularly if the considered flow regimes are still capillary dominated.

- In order to run the model on bigger networks, more representative of real pore spaces, there is a need to address the computational issues related to the discretised diffusion model. This is especially relevant for multiscale networks that possess a wide range of pore sizes.
- We would also propose additional core-flood experiments be carried out to confirm our findings. The essence of such experiments could be similar to the experiments conducted by Bennett et al. (2004), but using two different crude oils: one which is rich and the other which is poor in small polar compounds such as alkylphenols, carbazoles, etc.. The two resulting oil/water saturations would then be compared, and our prediction that these should be significantly different could be tested. We further suggest a more dynamic assessment of the wettability change, using for example in-situ contact angle measurements directly from micro-CT images (Andrew et al., 2014), to confirm the evolution of the wettability change during primary drainage. Additionally, in order to test our prediction of the removal of water films in the pore corners/crevices due to the evolving wettability change, we propose the evaluation of the remaining water at the pore-scale using micro-CT imaging as described by Pak et al. (2015).

List of references

ABDALLAH, W., BUCKLEY, J. S., CARNEGIE, A. & ZIAUDDIN, M. 2007. Fundamentals of Wettability. *Oilfield Review,* 19.

AL-YOUSEF, H. Y., LICHAA, P. M., AL-KAABI, A. U. & ALPUSTUN, H. 1995. Wettability Evaluation of a Carbonate Reservoir Rock from Core to Pore Level. *Society of Petroleum Engineers.* Middle East Oil Show, Bahrain: Society of Petroleum Engineers.

AMOTT, E. 1959. Observations Relating to the Wettability of Porous Rock. Petroleum Transactions, AIME.

ANDERSON, W. 1986. Wettability literature survey-part 2: Wettability measurement. *Journal of Petroleum Technology,* 38**,** 1,246-1,262.

ANDREW, M., BIJELJIC, B. & BLUNT, M. J. 2014. Pore-scale contact angle measurements at reservoir conditions using X-ray microtomography. *Advances in Water Resources,* 68**,** 24-31.

BENNETT, B., BUCKMAN, J. O., BOWLER, B. F. J. & LARTER, S. R. 2004. Wettability alteration in petroleum systems: the role of polar non-hydrocarbons. *Petroleum Geoscience,* 10**,** 271-277.

BENNETT, B., LAGER, A., POTTER, D. K., BUCKMAN, J. O. & LARTER, S. R. 2007. Petroleum geochemical proxies for reservoir engineering parameters. *Journal of Petroleum Science and Engineering,* 58**,** 355-366.

BLUNT, M. J. 1997. Pore Level Modeling of the Effects of Wettability. *SPE Journal,* 2**,** 494 - 510.

BLUNT, M. J. 1998. Physically-based network modeling of multiphase flow in intermediate-wet porous media. *Journal of Petroleum Science and Engineering,* 20**,** 117-125.

BLUNT, M. J. & SCHER, H. 1995. Pore-level modeling of wetting. *Physical Review E,* 52**,** 6387.

BUCKLEY, J. S. & LIU, Y. 1998. Some mechanisms of crude oil/brine/solid interactions. *Journal of Petroleum Science and Engineering,* 20**,** 155-160.

BULTREYS, T., VAN HOOREBEKE, L. & CNUDDE, V. 2015. Multi-scale, micro-computed tomography-based pore network models to simulate drainage in heterogeneous rocks. *Advances in Water Resources,* 78**,** 36-49.

CANTRELL, D. L. & HAGERTY, R. M. 1999. Microporosity in Arab Formation Carbonates, Saudi Arabia. *GeoArabia,* 4**,** 129 - 154.

CHOQUETTE, P. W. & PRAY, L. C. 1970. Geologic nomenclature and classification of porosity in sedimentary carbonates. *AAPG bulletin,* 54**,** 207-250.

CLERKE, E. A. 2009. Permeability, Relative Permeability, Microscopic Displacement Efficiency and Pore Geometry of M_1 Bimodal Pore Systems in Arab-D Limestone. *SPE Journal,* 14**,** 524 - 531.

CLERKE, E. A., ALLEN, D. F., CRARY, S. C., SRIVASTAVA, A., RAMAMOORTHY, R., SALDUNGARAY, P., SAVUNDARARAJ, P., HELIOT, D., GOSWAMI, J. & BORDAKOV, G. 2014. Wireline Spectral Porosity Analysis of the Arab Limestone—From Rosetta Stone to Cipher. *SPWLA 55th Annual Logging Symposium.* Abu Dhabi, United Arab Emirates: Society of Petrophysicists and Well-Log Analysts.

COX, P., WOOD, R., DICKSON, J., AL ROUGHA, H., SHEBL, H. & CORBETT, P. 2010. Dynamics of cementation in response to oil charge: Evidence from a Cretaceous carbonate field, UAE. *Sedimentary Geology,* 228**,** 246-254.

CUIEC, L. & YAHYA, F. A. 1991. Wettability of Asab Reservoir Rock: Comparison of Various Evaluation Methods, Role of Lithology. *SCA Paper No*.

CURTIS, A. & WOOD, R. 2005. Optimal elicitation of probabilistic information from experts. *In:* WOOD, R. (ed.) *Geological Prior Information.* Geological Society London.

DAKE, L. P. 1983. *Fundamentals of reservoir engineering*, Elsevier.

DIXIT, A. B., BUCKLEY, J. S., MCDOUGALL, S. R. & SORBIE, K. S. 2000. Empirical Measures of Wettability in Porous Media and the Relationship between Them Derived From Pore-Scale Modelling. *Transport in Porous Media,* 40**,** 27-54.

DIXIT, A. B., MCDOUGALL, S. R., SORBIE, K. S. & BUCKLEY, J. S. 1999. Pore-Scale Modeling of Wettability Effects and Their Influence on Oil Recovery. *SPE Reservoir Evaluation & Engineering,* 2**,** 25 - 36.

DODD, N., MARATHE, R., MIDDLETON, J., FOGDEN, A., CARNERUP, A., KNACKSTEDT, M., MOGENSEN, K., MARQUEZ, X., FRANK, S., BOUNOUA, N. & NOMAN, R. 2014. Pore-Scale Imaging of Oil and Wettability in Native-State, Mixed-Wet Reservoir Carbonates. *International Petroleum Technology Conference.* Doha, Qatar: International Petroleum Technology Conference.

DONALDSON, E. C., THOMAS, R. D. & LORENZ, P. B. 1969. Wettability Determination and Its Effect on Recovery Efficiency. *Society of Petroleum Engineers Journal,* 9**,** 13 - 20.

FASSI-FIHRI, O., ROBIN, M. & ROSENBERG, E. 1995. Wettability Studies at the Pore Level: A New Approach by the Use of Cryo-Scanning Electron Microscopy. *SPE Formation Evaluation,* 10**,** 11 - 19.

FRETTE, O. I., VIRNOVSKY, G. & HILDEBRAND-HABEL, T. 2009. Modelling the stability of thin water films using SEM images. *EUROPEC/EAGE Conference and Exhibition.* Amsterdam, The Netherlands: Society of Petroleum Engineers.

FUNG, L. S. K., MIDDYA, U. & DOGRU, A. H. 2011. Numerical Simulation of Fractured Carbonate Reservoirs with the M_1 Bimodal Pore System. *SPE Reservoir Simulation Symposium.* The Woodlands, Texas: Society of Petroleum Engineers.

GRAUE, A., ASPENES, E., BOGNØ, T., MOE, R. & RAMSDAL, J. 2002. Alteration of wettability and wettability heterogeneity. *Journal of Petroleum Science and Engineering,* 33**,** 3-17.

HAMON, G. 2000. Field-Wide Variations of Wettability. *Society of Petroleum Engineers.* Society of Petroleum Engineers.

HARLAND, S. R., WOOD, R. A., CURTIS, A., VAN DIJKE, M. I. J., STRATFORD, K., JIANG, Z., KALLEL, W. & SORBIE, K. 2015. Quantifying flow in variably wet microporous carbonates using object-based geological modelling and both lattice-Boltzmann and pore network fluid flow simulations. *AAPG Bulletin*.

HEASLEY, E. C., WORDEN, R. H. & HENDRY, J. P. 2000. Cement distribution in a carbonate reservoir: recognition of a palaeo oil–water contact and its relationship to reservoir quality in the Humbly Grove field, onshore, UK. *Marine and Petroleum Geology,* 17**,** 639-654.

HELLAND, J. O., RYAZANOV, A. & VAN DIJKE, M. I. J. 2008. Characterization of pore shapes for pore network models. *ECMOR XI: 11th European Conference on the Mathematics of Oil recovery.* Bergen, Norway.

HERRING, A. L., HARPER, E. J., ANDERSSON, L., SHEPPARD, A., BAY, B. K. & WILDENSCHILD, D. 2013. Effect of fluid topology on residual nonwetting phase trapping: Implications for geologic CO2 sequestration. *Advances in Water Resources,* 62**,** 47-58.

HIRASAKI, G. J. 1991. Wettability: Fundamentals and Surface Forces. *SPE Formation Evaluation,* 6**,** 217 - 226.

HUANG, Y., RINGROSE, P. S., SORBIE, K. S. & LARTER, S. R. 1996. The Effects of Heterogeneity and Wettability on Oil Recovery from Laminated Sedimentary Structures. *SPE Journal,* 1**,** 451 - 462.

IDOWU, N., LONG, H., ØREN, P.-E., CARNERUP, A. M., FOGDEN, A., BONDINO, I. & SUNDAL, L. 2015. Wettability analysis using Micro-CT, FESEM and QEMSCAN, and its applications to digital rock physics. International Symposium of the Society of Core Analysts 16-21 August, 2015. St. John's Newfoundland and Labrador, Canada

JACKSON, M. D., VALVATNE, P. H. & BLUNT, M. J. 2003. Prediction of wettability variation and its impact on flow using pore- to reservoir-scale simulations. *Journal of Petroleum Science and Engineering,* 39**,** 231-246.

JADHUNANDAN, P. P. & MORROW, N. R. 1995. Effect of Wettability on Waterflood Recovery for Crude-Oil/Brine/Rock Systems. *SPE Reservoir Engineering,* 10**,** 40 - 46.

JIANG, Z., VAN DIJKE, M. I. J., SORBIE, K. S. & COUPLES, G. D. 2013. Representation of multiscale heterogeneity via multiscale pore networks. *Water Resources Research,* 49**,** 5437-5449.

JIANG, Z., WU, K., COUPLES, G., VAN DIJKE, M. I. J., SORBIE, K. S. & MA, J. 2007. Efficient extraction of networks from three-dimensional porous media. *Water Resources Research,* 43**,** n/a-n/a.

JOEKAR-NIASAR, V., PRODANOVIĆ, M., WILDENSCHILD, D. & HASSANIZADEH, S. M. 2010. Network model investigation of interfacial area, capillary pressure and saturation relationships in granular porous media. *Water Resources Research,* 46**,** n/a-n/a.

JURI, J., VAN DIJKE, M. & SORBIE, K. 2016. Inversion of the lattice network wettability subjected to the capillary pressure of the entire flooding cycle: Hamiltonian Monte Carlo posterior sampling and prediction of the relative permeability. *Journal of Petroleum Science and Engineering*.

KNACKSTEDT, M. A., PINCZEWSKI, W. V., FOGDEN, A. & SENDEN, T. 2011. Improved characterization of EOR processes in 3D. Characterizing mineralogy, wettability and residual fluid phases at the pore scale. *SPE Enhanced Oil Recovery Conference.* Kuala Lumpur, Malaysia: Society of Petroleum Engineers.

KOVSCEK, A. R., WONG, H. & RADKE, C. J. 1993. A pore-level scenario for the development of mixed wettability in oil reservoirs. *AIChE Journal,* 39**,** 1072-1085.

KOWALEWSKI, E., BOASSEN, T. & TORSAETER, O. 2003. Wettability alterations due to aging in crude oil; wettability and Cryo-ESEM analyses. *Journal of Petroleum Science and Engineering,* 39**,** 377-388.

LENORMAND, R., ZARCONE, C. & SARR, A. 1983. Mechanisms of the displacement of one fluid by another in a network of capillary ducts. *Journal of Fluid Mechanics,* 135**,** 337-353.

LICHAA, P. M., ALPUSTUN, H., ABDUL, J. H., NOFAL, W. A. & FUSENI, A. B. 1993. Wettability Evaluation of a Carbonate Reservoir Rock. *Advances in Core Evaluation III, Reservoir Management,* 327.

LØNØY, A. 2006. Making sense of carbonate pore systems. *AAPG bulletin,* 90**,** 1381-1405.

LORD, D. L. & BUCKLEY, J. S. 2002. An AFM study of the morphological features that affect wetting at crude oil–water–mica interfaces. *Colloids and Surfaces A: Physicochemical and Engineering Aspects,* 206**,** 531-546.

LUCACH, S. O., BOWLER, B. F. J., FREWIN, N. & LARTER, S. R. 2002. Variation in alkylphenol distributions in a homogenous oil suite from the Dhahaban petroleum system of Oman. *Organic Geochemistry,* 33**,** 581-594.

LUCIA, F. 1983. Petrophysical parameters estimated from visual descriptions of carbonate rocks: a field classification of carbonate pore space. *Journal of Petroleum Technology,* 35**,** 629-637.

MAHANI, H., BERG, S., ILIC, D., BARTELS, W.-B. & JOEKAR-NIASAR, V. 2015. Kinetics of low-salinity-flooding effect. *SPE Journal,* 20**,** 8-20.

MAN, H. & JING, X. 2000. Pore network modelling of electrical resistivity and capillary pressure characteristics. *Transport in Porous Media,* 41**,** 263-285.

MARATHE, R., TURNER, M. L. & FOGDEN, A. 2012. Pore-Scale Distribution of Crude Oil Wettability in Carbonate Rocks. *Energy & Fuels,* 26**,** 6268-6281.

MARZOUK, I. Wettability and saturation in Abu Dhabi carbonate reservoirs. SPE Middle East Oil Show & Conference, 1999. 497-503.

MASALMEH, S. K. The effect of wettability on saturation functions and impact on carbonate reservoirs in the middle east. Abu Dhabi International Petroleum Exhibition and Conference, 2002. Society of Petroleum Engineers.

MCDOUGALL, S. R., DIXIT, A. B. & SORBIE, K. S. 1997. Network analogues of wettability at the pore scale. *Geological Society, London, Special Publications,* 122**,** 19-35.

MCDOUGALL, S. R. & SORBIE, K. S. 1995. The Impact of Wettability on Waterflooding: Pore-Scale Simulation. *SPE Reservoir Engineering,* 10**,** 208 - 213.

MORROW, N. R. 1975. The effects of surface roughness on contact: angle with special reference to petroleum recovery. *Journal of Canadian Petroleum Technology,* 14.

MORROW, N. R. 1990. Wettability and Its Effect on Oil Recovery. *Journal of Petroleum Technology,* 42.

MORROW, N. R. & BUCKLEY, J. 2006. Wettability and Oil Recovery by Imbibition and Viscous Displacement from Fractured and Heterogeneous Carbonates. *Chemical & Petroleum Engineering*.

OKASHA, T. M., FUNK, J. J. & RASHIDI, H. N. 2007. Fifty Years of Wettability Measurements in the Arab-D Carbonate Reservoir. *SPE Middle East Oil and Gas Show and Conference.* Kingdom of Bahrain: Society of Petroleum Engineers.

OREN, P. E., BAKKE, S. & ARNTZEN, O. J. 1998. Extending Predictive Capabilities to Network Models. *SPE Journal,* 3**,** 324 - 336.

PAK, T., BUTLER, I.B., GEIGER, S., VAN DIJKE, M.I. AND SORBIE, K.S., 2015. Droplet fragmentation: 3D imaging of a previously unidentified pore-scale process during multiphase flow in porous media. Proceedings of the National Academy of Sciences, 112(7), pp.1947-1952.

PATZEK, T. W. 2001. Verification of a Complete Pore Network Simulator of Drainage and Imbibition. *SPE Journal,* 6**,** 144 - 156.

POURMOHAMMADI, S., HETLAND, S., SPILDO, K. & SKAUGE, A. 2015. Does the Pore Class Concept for Carbonates Make Sense for Multi Phase Flow? Paper SCA2008-29 presented at the International Symposium of the Society of Core Analysts, Abu Dhabi, UAE, Oct, 2008.

PRODANOVIĆ, M., MEHMANI, A. & SHEPPARD, A. P. 2015. Imaged-based multiscale network modelling of microporosity in carbonates. *Geological Society, London, Special Publications,* 406**,** 95-113.

ROEHL, P.O. and CHOQUETTE, P.W. 2012. Carbonate petroleum reservoirs. Springer Science & Business Media.

ROTH, S., BISWAL, B., AFSHAR, G., HELD, R. J., OREN, P.-E., BERGE, L. I. & HILFER, R. 2011. Continuum-based rock model of a reservoir dolostone with four orders of magnitude in pore sizes. *AAPG bulletin,* 95**,** 925-940.

RUESLÅTTEN, H., ØREN, P., ROSENBERG, E. & CUIEC, L. 1994. A Combined Use of CRYO-SEM and NMR for Studying the Distribution of Oil and Brine in Sandstones. *paper SPE/DOE,* 27804.

RYAZANOV, A. 2012. *Pore scale network modelling of residual oil saturation in mixed-wet systems.* PhD thesis, Heriot-Watt University.

RYAZANOV, A. V., DIJKE, M. I. J. & SORBIE, K. S. 2009. Two-Phase Pore-Network Modelling: Existence of Oil Layers During Water Invasion. *Transport in Porous Media,* 80**,** 79-99.

RYAZANOV, A. V., SORBIE, K. S. & VAN DIJKE, M. I. J. 2014. Structure of residual oil as a function of wettability using pore-network modelling. *Advances in Water Resources,* 63**,** 11-21.

SALATHIEL, R. A. 1973. Oil Recovery by Surface Film Drainage In Mixed-Wettability Rocks. *Journal of Petroleum Technology,* 23.

SCHMATZ, J., URAI, J. L., BERG, S. & OTT, H. 2015. Nanoscale imaging of pore-scale fluid-fluid-solid contacts in sandstone. *Geophysical Research Letters,* 42**,** 2189-2195.

SHARMA, M. M. & WUNDERLICH, R. W. 1987. The alteration of rock properties due to interactions with drilling-fluid components. *Journal of Petroleum Science and Engineering,* 1**,** 127-143.

SKAUGE, A. & OTTESEN, B. 2002. A summary of experimentally derived relative permeability and residual saturation on North Sea reservoir cores. International Symposium of the SCA, Monterey, CA, 2002.

SKAUGE, A., SØRVIK, A., VIK, B. & SPILDO, K. 2006. Effect of wettability on oil recovery from carbonate material representing different pore classes. *International Symposium of the Society of Core Analysts.* Trondheim, Norway.

SKAUGE, A., SPILDO, K., HØILAND, L. & VIK, B. 2007. Theoretical and experimental evidence of different wettability classes. *Journal of Petroleum Science and Engineering,* 57**,** 321-333.

TAYLOR, P., LARTER, S., JONES, M., DALE, J. & HORSTAD, I. 1997. The effect of oil-water-rock partitioning on the occurrence of alkylphenols in petroleum systems. *Geochimica et Cosmochimica Acta,* 61**,** 1899-1910.

TIE, H. & MORROW, N. R. 2005. Oil recovery by spontaneous imbibition before and after wettability alteration of three carbonate rocks by a moderately asphaltic crude oil. International Symposium of Society of Core Analysis, Toronto, Canada, Aug, 2005. 21-25.

VALVATNE, P. H. & BLUNT, M. J. 2004. Predictive pore-scale modeling of two-phase flow in mixed wet media. *Water Resources Research,* 40**,** n/a-n/a.

VAN DIJKE, M. I. & SORBIE, K. S. 2006. Existence of fluid layers in the corners of a capillary with non-uniform wettability. *Journal of colloid and interface science,* 293**,** 455-63.

VAN DUIN, A. C. T. & LARTER, S. R. 2001. A computational chemical study of penetration and displacement of water films near mineral surfaces. *Geochemical Transactions,* 2**,** 35.

VOGEL, H.-J. 2002. Topological Characterization of Porous Media. *In:* MECKE, K. & STOYAN, D. (eds.) *Morphology of Condensed Matter.* Springer Berlin Heidelberg.

YUAN, Y. & LEE, T. R. 2013. Contact angle and wetting properties. *Surface science techniques.* Springer.

ZHAO, X., BLUNT, M. J. & YAO, J. 2010. Pore-scale modeling: Effects of wettability on waterflood oil recovery. *Journal of Petroleum Science and Engineering,* 71**,** 169-178.